UNIVERSIDADE
BEIRA INTERIOR

Hot-Wire Measurements in a Low Pressure Turbine Linear Cascade

(Versão Corrigida Após Defesa)

Mariana Caetano Lousada

Dissertação para obtenção do Grau de Mestre em
Engenharia Aeronáutica
(Mestrado Integrado)

Orientadores:
Prof. Doutor Kouamana Bousson
Prof. Doutor Francisco Brójo
Prof. Doutor Sergio Lavagnoli

Março de 2022

Dedicated to my family

Acknowledgement

First of all, I would like to thank my supervisors, Dr. Kouamana Bousson, Dr. Francisco Brojo and Dr. Sergio Lavagnoli, for all their time and patience in following this thesis. I am very grateful for all the knowledge transmitted by Dr. Francisco Brójo about turbomachinery which allowed me to easily understand my project. To Dr. Kouamana Bousson I thank for always encouraging me to improve my skills and knowledge throughout my journey at the University of Beira Interior and for all the support he gave me when I decided to do my thesis at VKI. To Dr. Sergio Lavagnoli I would like to thank him for providing this amazing opportunity to develop this thesis at VKI and for supporting the work with all his knowledge.

I would also like to thank the SPLEEN team for the good reception in the project, especially Gustavo and Loris for all the time we spent together in the wind tunnel, for always being available to discuss new approaches with me and for all the beers they paid during the beer meetings. Also to my first teacher on hot wires Filippo for always being available at any time of the day to explain to me how hot-wires work and to Elissavet for all the meetings and discussions on the project.

I would like to express my gratitude to all the friends I made in Covilhã, they gave me the best experience I could ask for with many fun and crazy moments. A special thanks to Tiago and Miguel for all the support in the hardest times, for always being there when I needed it and for all the good memories.

If doing a thesis is hard, I think it is even harder when you are not in your own country, luckily I met some incredible people on this journey that I cannot be thankful enough for all the good moments. To Giacomo, Lorenzo, Gonçalo, Jorge, Gian, Nicola, Denis, Maria, and Andrea, thank you for all the help and for making Brussels so much more fun.

Finally, I would like to conclude by thanking my family for their daily support and sacrifices, without them I would not have gotten to this point and I would not be the person I am today. A very special thanks to my grandmother for all the support and encouragement, for all the phone calls and for being my biggest support.

Resumo

As simulações numéricas são uma ferramenta importante de análise e design na indústria aeronáutica. A ambição de melhorar o desempenho e a sustentabilidade dos motores aeronáuticos modernos, combinada com o uso intensivo de simulações numéricas, criou novos desafios no desenvolvimento de ferramentas de CFD. A modelação da turbulência e a dificuldade em definir corretamente as condições de fronteira são duas das limitações mais significativas na aplicação de CFD em escoamentos característicos de turbomáquinas, sendo as características de entrada do escoamento turbulento geralmente a maior incógnita.

O presente estudo aborda a aplicação de anemometria de fio quente num escoamento de baixa densidade e alta velocidade, na entrada de uma cascata linear representativa de uma turbina transónica de baixa pressão. O objetivo principal desta pesquisa é a caracterização do escoamento na secção de entrada da cascata, em termos de turbulência e escalas de comprimento integral. A anemometria de fio quente é uma técnica amplamente conhecida para medir flutuações de velocidade. Contudo, as condições de medição neste estudo apresentam um elevado grau de complexidade, devido à compressibilidade do escoamento e ao efeito da rarefação. Além disso, poucas investigações foram realizadas nas condições indicadas, evidenciando a falta de uma metodologia sólida para este tipo de aplicação.

No âmbito de um projeto financiado pela UE, a campanha de testes ocorreu no túnel de vento de alta velocidade e baixa densidade $S - 1/C$, localizado no von Karman Institute for Fluid Dynamics. Foi utilizado um fio quente simples e implementada uma calibração não dimensional desenvolvida recentemente. As medições foram realizadas acima da cascata com a presença de dois geradores de turbulência, um passivo e um ativo. Para as medições de média temporal, a camada limite foi caracterizada em termos de velocidade média, parâmetros integrais e parâmetros da parede. Na primeira fase da campanha referente apenas ao gerador passivo de turbulência, três metodologias foram comparadas para as medições de série temporal. Após selecionada a metodologia, a turbulência, as escalas de comprimento integral e os espectros de energia foram calculados. Na segunda fase da campanha com ambos os geradores de turbulência, a *phase locked averaging* foi aplicada para remover os componentes periódicos do sinal. Eventualmente, o conjunto de dados obtido poderá ser usado para para a validar ferramentas numéricas para aplicações em turbomáquinas.

Palavras-chave

Anemometria de fio quente, CFD, Camada Limite, Escalas de comprimento, PSD, Turbulência, Turbomáquinas, Tunel de vento, Turbina de baixa pressão, PLA

Abstract

Numerical simulations are an important analysis and design tool in the turbomachinery industry. The ambition to improve the performance and sustainability of modern aero-engines, combined with the extensive use of numerical simulation, has created new challenges in the development of accurate CFD tools. The turbulence modelling and the lack of well defined boundary conditions are two of the most significant limitations in the application of CFD in turbomachinery flows, with the characteristics of the inlet turbulent flow being usually the biggest unknown.

The presented study addresses the application of Hot-Wire Anemometry in a low-density and high-speed flow, at the inlet of a linear cascade representative of a transonic low pressure turbine. In this context, the main objective of this research is the turbulence characterization of the inlet section of the cascade, in terms of turbulence intensity and integral length scales. The Hot-Wire Anemometry is a well known technique for measuring velocity fluctuations. However, measurements in the present conditions feature an increased degree of complexity, due to the compressibility of the flow and the effect of the gas rarefaction. Moreover, few investigations were conducted in such conditions, highlighting a lack of a solid methodology for this kind of application.

In the frame of a large EU-funded project, the test campaign took place in the high-speed and low-density wind tunnel S-1/C, located at the von Karman Institute for Fluid Dynamics. A single hot-wire was employed and a recently developed non-dimensional calibration was implemented. The measurements were performed upstream of the cascade with the presence of a passive and an active turbulence generator. For time-average measurements the inlet endwall boundary layer was characterized in terms of mean velocity, integral parameters and wall units. In the first case of the campaign regarding only the passive turbulence generator, three methodologies were compared for the time-resolved measurements. Once the methodology was selected the inlet turbulence intensity, integral length scales and energy spectra were computed. In the second phase of the campaign with both active and passive turbulence generators, a phase locked averaging had to be applied to remove the periodic components of the signal. Eventually, the obtained dataset can be used to define high-order boundary conditions for the validation of high-fidelity numerical tools for turbomachinery applications.

Keywords

Hot-Wire Anemometry, CFD, Boundary Layer, Length Scales, PSD, Turbulence, Turbomachinery, Wind Tunnel, Low Pressure Turbine, PLA

Contents

List of Figures

List of Tables

List of Acronyms

A/D	Analog to Digital
ACF	Autocorrelation function
FSTI	e free-stream turbulence intensity
RMS	root mean square
St	Strouhal number
5HPP	5-Hole Pressure Probe
ACF	autocorrelation function
BPF	Bar Passing Frequency
CCA	constant current anemometry
CFD	computational fluid dynamics
CTA	constant temperature anemometry
CTHWA	Constant Temperature Hot-Wire Anemometry
CVA	constant voltage anemometry
DC	Direct Current
DNS	Direct Numerical Simulation
EU	European Union
FRPP	Fast Response Pressure Probe
HW	Hot-Wire
HWA	Hot-Wire Anemometry
ILS	Integral Length Scales
LE	Leading edge
LES	Large Eddy Simulations
LPT	Low Pressure Turbine
NASA	National Aeronautics and Space Administration
PIV	Particle Image Velocimetry
PLA	Phase Locked Averaging
PSD	Power Spectral Density
RANS	Reynolds Averaged Navier-Stokes
RDF	Rotor Disk Frequency
RPM	Rotation per minut
SAE	SAFRAN Aircraft Engines
SPLEEN	Secondary and Leakage Flow Effects in High-SPeed Low PrEssurE TurbiNes
TA	Time Average
TE	Trailing Edge
TG	Turbulence Grid
TR	Time Resolve
VKI	von Karman Institute for Fluid Dynamics

List of Symbols

A_w	External surface of the wire	[m^2]
A, B and n	Constants for the King's law	[-]
B	Slope of the log layer	[-]
C	Kolmogorov constant	[-]
c_f	Skin friction coefficient	[-]
c_w	Specific heat	[J/(kg°C)]
d_w	Wire diameter	[μ m]
$E(k)$ or $E(f)$	Energy Spectrum function	[dB/Hz]
E	Anemometer output voltage	[V]
E_b	Anemometer bridge output voltage	[V]
E_{out}	Output voltage	[V]
E_w	Wire voltage	[V]
f_c	Cut-off frequency	[Hz]
f_p	Periodic signal	[Hz]
f_s	Sampling frequency	[Hz]
Gr	Grasshof number	[-]
H	Shape factor	[-]
h	Heat transfer coefficient	[W/(m^{2}K)]
I	Current	[A]
I	Roach constant (I=0.2)	[-]
k	Thermal conductivity	[W/(m K)]
k_{20}	Thermal conductivity at $20°C$	[W/(m K)]
Kn_w	Knudsen number of the wire	[-]
Kn	Knudsen number	[-]
ℓ	Length scale	[m]
$\mathcal{L}$	Characteristic length scale of the flow	[m]
ℓ_0	length scale of the largest eddies	[m]
ℓ_{DI}	demarcation lengthscale between the dissipation range ($\ell < \ell_{DI}$)and the inertial subrange ($\ell > \ell_{DI}$)	[m]
ℓ_{EI}	demarcation between the anisotropic large eddies ($\ell > \ell_{EI}$) and the isotropic small eddies($\ell < \ell_{EI}$)	[m]
l_w	Wire length	[mm]
M	Mach number	[-]
$M_{in,is}$	Inlet Mach number	[-]
$M_{out,is}$	Outlet Mach number	[-]
N	number of samples	[-]
Nu	Nusselt number	[-]
Nu_{corr}	Nusselt number corrected	[-]
p	Static pressure	[Pa]
P	Electrical Power	[W] P_0
	Total pressure	[Pa]

Pr	Prandtl number	[-]
Q	Thermal power	[W]
R	Universal gas constant	[J/kg·K]
R^2	R-squared	[-]
R_{ref}	Sensor resistance at a reference temperature	[ohm]
R_s	Support resistance	[ohm]
R_t	Total resistance	[ohm]
R_w	Sensor resistance	[ohm]
$R_{w,cold}$	Cold resistance of the wire	[ohm]
Re	Reynolds number	[-]
$Re_{in,is}$	Inlet Reynolds number	[-]
$Re_{out,is}$	Outlet Reynolds number	[-]
Re_w	Reynolds number based on the wire diameter	[-]
S_α	Yaw angle sensitivity	[-]
S_β	Pitch angle sensitivity	[-]
S_ρ	Sensitivity to density	[-]
S_{T_0}	Sensitivity to total temperature	[-]
S_u	Sensitivity to velocity	[-]
T	Static temperature	[K]
T_0	Total temperature	[K]
t	Time instant	[s]
$\mathcal{T}(\ell)$	Rate at which energy is transferred from eddies larger than ℓ_{EI} to those smaller than ℓ_{DI}.	[m^2/s^2]
$\mathcal{T}_{DI}$	Rate of transfer of energy into the dissipation range from larger scales	[m^2/s^2]
$\mathcal{T}_{EI}$	Rate of transfer of energy from large eddies to small eddies	[m^2/s^2]
T_{int}	Integral time scale	[s]
T_{ref}	Reference temperature	[K]
T_{heat}	Recovery temperature	[K]
Tu	Turbulence intensity	[%]
T_w	Temperature of the wire	[K]
$T_{w,eff}$	Effective wire temperature	[K]
u	Characteristic velocity scale of the flow	[m/s]
$\overline{u'}$	Root mean square (RMS) of the velocity fluctuations	[m/s]
u^+	mean velocity normalized by the friction velocity	[-]
u'	Fluctuating Velocity	[m/s]
$u(l)$	Characteristic velocity of an eddy of size ℓ	[m/s]
u_η	Kolmogorov velocity	[m/s]
u_τ	Friction velocity	[m/s]
u_0	Velocity scale of the largest eddies	[m/s]
U	Velocity	[m/s]
$U(x,t)$	Eulerian velocity	[m/s]
U_{FS}	Free-stream velocity	[m/s]

U_N	Velocity component normal to the wire	[m/s]
U_T	Velocity component tangential to the wire	[m/s]
U_∞	Free-stream velocity	[m/s]
X	Instantaneous signal	[-]
X'	Purely stochastic fluctuations	[-]
$\widetilde{X}$	Periodic fluctuations	[-]
Y_{tot}	Total pressure drop coefficient	[-]
Y_{TG}	Pressure drop coefficient across the turbulence grid	[-]
Y_{WG}	Pressure drop coefficient across the turbulence generator	[-]
y^+	distance from the wall normalized by the viscous length scale	[-]
k	von Karman constant	[-]
$\wp$	Rate of production of turbulent kinetic energy	[m^2/s^2]

Greek letters

α	Yaw angle	[rad]
α'	Yaw angle fluctuations	[rad]
α_w	Wire specific temperature coefficient of resistance	[ppm/$^\circ$ C]
β	Pitch angle	[rad]
β'	Pitch angle fluctuations	[rad]
γ	Ratio of specific heats	[-]
$\delta(x)$	Boundary-layer thickness	[mm]
δ_{99}	Boundary-layer thickness at 99%	[mm]
δ_1 or δ^*	Displacement thickness	[mm]
δ_2 or θ	Momentum thickness	[mm]
δ_ν	Viscous length scale	[mm]
Δt	Time interval	[s]
ε	Rate of dissipation of turbulent kinetic energy	[m^2/s^3]
η	Kolmogorov length scale	[mm]
η	Recovery factor	[-]
Λ	Integral length scales	[mm]
ν	Kinematic viscosity	[m^2/s]
μ	Dynamic viscosity	[Pa $\cdot$ s]
ρ	Density	[kg/m^3]
ρ_∞	Free-stream density	[kg/m^3]
ρ'	Density fluctuations	[kg/m^3]
τ	Time interval	[s]
τ_η	Kolmogorov time scale	[s]
τ_w	Wall shear stress	[Pa]
τ_w	Overheat ratio	[-]
ϕ	Dewey correction term	[-]

Chapter 1

Introduction

1.1 Motivation

Over the years, technical advances in aircraft engines and operating systems have been driven by the development of more efficient and cleaner solutions. The future targets include the maximization of the performance, safeguard of components integrity, minimization of fuel consumption and production of fewer emissions. The low pressure turbine (LPT) is one of the heaviest aero-engine components, accounting for about 30% of the engine weight. The continuous quest for lighter engines leads to the reduction of the number of stages, resulting in highly-loaded blades. The higher rotational speed of the LPT, therefore higher loads and higher stage pressure ratios, results in new aero-mechanical challenges for high-speed LPT manufacturers. The LPT operates at high-subsonic/transonic conditions in term of exit Mach number ($M \sim 0.8 - 0.9$) and, at the same time, operate at the lowest Reynolds number of the engine, which may vary from 5×10^5 at take off and landing to 5×10^4 at cruise conditions [1]. The low Reynolds number environment, combined with the strong adverse pressure gradient occurring after the high velocity peak on the suction side of the blade, lead to severe risk of boundary layer separation [1]. Since this behaviour has a direct impact on the engine efficiency, the aerodynamic of low pressure turbine blades has been extensively studied over the years.

To better understand the loss mechanisms and heat transfer phenomena in complex turbomachinery flows, a rigorous characterization of flow turbulence (i.e. turbulence intensity, length scales, and even spectrum) is required. In low pressure turbines, the free-stream turbulence intensity and length scales are critical for the boundary layer transition and/or separation along the blade surfaces, and therefore for the component's losses [2]. A thorough investigation was conducted by Mayle et al. [3], describing in detail the role of the laminar to turbulent transition of the boundary layer of a highly loaded LPT blade.

With the advances in computer performance, computational fluid dynamics (CFD) has become a primary design tool for turbomachinery components. Given the high specific cost of experimental facilities, it is also becoming a frequent investigation tool, replacing an increasing number of experimental investigations. Nevertheless, as discussed by Denton [4], there are still significant limitations on the use of CFD, especially for complex turbomachinery flows, which underline the importance of experimental validation. Turbulence modeling and unknown or incomplete boundary conditions are among those limitations. The calibration of turbulence models is frequently based on simple laboratory cases that do not represent

real flow conditions, imposing tuning and adjustment of model constants for specific applications. Though the use of high-fidelity CFD, such as Direct Numerical Simulation (DNS) and Large Eddy Simulations (LES), modeling errors can be reduced, but the quality and validity of simulations are still dependent on the accuracy of the imposed boundary conditions. From the point of view of turbulence, these normally include the turbulent kinetic energy and length scales at the inlet of the computational domain, information which is rarely completely known [5].

The aim of the present study is to provide reliable and accurate measurements of turbulence intensity and integral length scales in conditions representative of a LPT by means of Constant Temperature Hot-Wire Anemometry (CTHWA). Despite its fragility, CTHWA is one of the most commonly used tools in turbulence research and often the reference technique against which other methods are validated. Nevertheless, as a consequence of its mainstream usage, the peculiarities of its application are often overlooked. This can lead to poorly mastered experimental data and post-processing, for example when fluctuations on the flow properties other than the velocity are not considered, resulting in a general lack of fidelity on the final results.

1.2 State of the Art

Hot-Wire Anemometry is the main measurement technique for turbulence research since the beginning of the 20th century (King [6] and Bousinnesq [7]) and it is still one of the reference techniques for turbulence measurements and validation of other experimental approaches, thanks to its high frequency response, high spatial resolution and good signal to noise ratio [8].

One of the first relevant studies of turbulence in tubomachinery was realized by Camp & Shin [9]. Using hot-wire anemometry, they measured the turbulence intensity and integral length scale in a low-speed multistage compressor rig. Oro et al. [10] analyzed the structure of turbulence at a single stage, low speed axial fan by performing hot-wire measurements. They measured the turbulence intensity and length scales at three axial stations (inlet to the stage, rotor exit, stator exit).

Maunus et al. [11] computed the turbulence evolution in terms of turbulent kinetic energy, dissipation rate and length scales. They analysed an extensive dataset provided by NASA, acquired downstream of a fan stage in a scaled geared turbofan by means of multiple hot-wire probes.

More recently, Odier et al. [12] acquired the evolution of the turbulence intensity and integral length scale through the fan stage of a small geared turbofan. They compared Hot-Wire Anemometry measurements with two CFD codes in order to validate the latter's prediction of turbulence intensity, spectra and integral length scales.

Other relevant studies in turbines are limited to turbulence intensity values. Porreca et al. [13] measured turbulence in a two-stage turbine test rig using fast response pressure probes. Chasoglou et al. [14] performed turbulence measurements in the same test rig with a multi-hole fast response pressure probe, evaluating also the anisotropy level of the flow field. Lengani et al. [15] retrieved the turbulence intensity downstream of an LPT rotor using a single-sensor fast response pressure probe. Bauinger et al. [16] used hot-wires and fast response pressure probes to measure turbulence downstream of the LPT rotor in a two-stage two-spool turbine test rig. They compared the turbulence intensity computed by the two techniques.

Furthermore, for Low Pressure Turbines, Schwarzbach et al. [17] investigated the effect of different turbulence scales on the separation-induced boundary layer transition on the suction side of the blade, both experimentally and numerically. Chemnitz [18] recently compared 3D hot-wire and Particle Image Velocimetry (PIV) measurements downstream of a linear LPT cascade at high-speed engine representative conditions. According to Chemnitz, the combination of a high velocity and a low density environment presents a challenging complexity for all measurement techniques, particularly Hot-Wire Anemometry.

It is clear from the literature review that even information about the integral length scale is rare in experimental turbomachinery test cases. Such data in engine representative conditions (in terms of Mach and Reynolds number) are even rarer, as most studies have been conducted at low-speed facilities (e.g. [19][20]). This lack of data can be attributed to the difficulties in applying appropriate measurement techniques in such environments, as well as the complexity of the required post-processing methods when deterministic fluctuations are also present in the signal [5].

Despite being widely used for many years, the application of CTHWA to certain flow regimes, such as high subsonic and low density flows, is still limited. Researchers such as Cukurel et al. [21], Boyle et al. [22] and Boufidi [5] have proposed extensions to the applicability of CTHWA in such conditions, but more research is needed before a general measurement methodology can be established. For these reasons, few studies have been conducted in high subsonic/transonic and subsonic slip flows where many turbomachinery flows lie.

1.3 Objectives

The current study was carried out in the world-class S-1/C high-speed wind tunnel of the von Karman Institute of Fluid Dynamics (VKI). This study is part of a large EU-funded project called SPLEEN (Secondary and Leakage Flow Effects in High-SPeed Low PrEssurE TurbiNes), investigating the aerodynamics of High-Speed Low Pressure Turbines at engine-representative conditions. The program was born from a collaboration with SAFRAN Aircraft Engines (SAE) in 2018, which aims to provide a large experimental open database of time-resolved 3D unsteady flow data in engine-realistic conditions. This database intends to

fill the gap of experimental data and provide knowledge on loss mechanisms in high-speed low pressure turbines. Furthermore, the SPLEEN project's accomplishments will provide an extensive and detailed database for the development and validation of innovative technologies and tools for the design of modern high-speed LPT.

Hot-Wire Anemometry has an additional level of complexity in high-speed flow environments due to the compressibility effect of the flow. Furthermore, if the flow is characterized by low density, the interaction between the flow and the wire is further complicated by the influence of gas-rarefaction. Due to the complexity of applying Hot-Wire Anemometry in such flows, there is no consolidated and highly validated methodology that allows for the treatment of hot-wire measurements in high-speed flow with a high level of confidence.

Recently, a modern and practical calibration approach has been developed by Cukurel [21] and applied by Boufidi [5] in several conditions. In the present research work, the aforementioned methodology is employed. To the author knowledge, besides of the previous investigation of Biondi [23] in the same facility no others studies were conducted addressing the same flow conditions.

Finally, the primary objective of the present study is the application of Hot-Wire Anemometry in a challenging environment such as the one featured by a modern Transonic Low Pressure Turbine. The main purpose of the hot-wire measurements are the characterization of the turbulence field (i.e. turbulence intensity and integral length scales) at the inlet of a linear cascade and the investigation of the endwall inlet boundary layer.

1.4 Thesis Outline

The present study is divided in the following chapters:

Chapter 1 expresses the author's motivation behind the development of this thesis. Provides a general overview about the state-of-art on High-Speed turbines research, highlighting the role of Hot-Wire Anemometry. And finally, the objectives proposed for this thesis are also presented.

Chapter 2 establishes the theoretical foundation required to analyze the campaign's results. The principles of turbulence and its statistical description are presented, as well as turbulent boundary layer fundamentals.

Chapter 3 describes the wind tunnel facility and gives information about the test section and its experimental features. A description of the related instrumentation is also provided.

Chapter 4 describes the hot-wire operating principles and the calibration methodology. The procedures and equipment used in calibration are explained in detail in this chapter. Finally, a description of the post-processing methodologies is provided.

Chapter 5 presents the results for time-average and time-resolved measurements of the experimental test campaign. The former refers to the results whose objective is characterize the the inlet boundary layer and the mean velocity field of the flow. The latter retrieves the information from the instantaneous data, such as turbulence intensity and integral length scales. Furthermore, some considerations about sensitivities are made and the turbulent power density spectrum for different cases is analyzed.

Chapter 6 collects the outcomes of the presented research work and outlines the main conclusions.

Chapter 2

Theoretical background

2.1 Turbulence

This section provides a brief overview of turbulent flows for the purposes of the current study. The literature contains a comprehensive treatment of turbulent flows and although the concept of turbulence is almost intuitive, a precise definition of it is extremely difficult to formulate, and even if we were to achieve this definition, it would most likely be difficult to characterize all of the properties inherent in such a complex process. One of the good definitions of turbulence is presented by Peter Bradshaw [24]:

" Turbulence is a three-dimensional time-dependent motion in which vortex stretching causes velocity fluctuations to spread to all wavelengths between a minimum determined by viscous forces and a maximum determined by the boundary conditions of the flow. It is the usual state of fluid motion except at low Reynolds numbers."

2.1.1 Principles

The first evidence of turbulent flows are attributed to O. Reynolds (1883) who performed experiments in a pipe using coloured filaments. Figure 2.1 shows a conceptualization of the experiments conducted by Reynolds. At low Reynolds numbers, the relative intensity of dissipative effects induced by viscous stresses is sufficient to dampen any small disturbances naturally existing in the environment and imposed on the boundary layer, be they mechanical vibrations of the structure, body surface irregularities, waves of pressure associated with acoustic noise, among others. At higher Reynolds numbers, some of these small perturbations are already able to tune into the flow and, similarly to a resonance phenomenon, be amplified by it, leading, after a highly non-linear process, to a degeneration in a chaotic flow. It is said then that a transition from laminar to turbulent regime occurred.

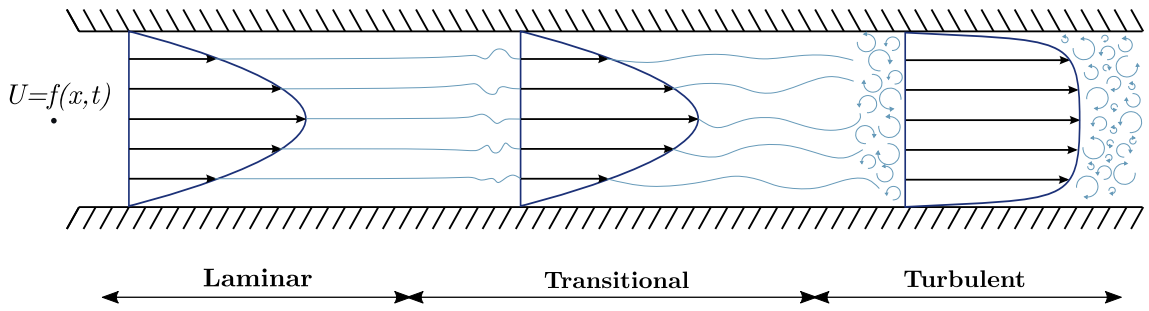

Figure 2.1: Reynolds experiment: Laminar to turbulent transition in a channel flow [23]

A turbulent regime is fundamentally characterized by its irregularity and three-dimensionality, in which velocity fluctuations of different intensities and different wavelengths, around an average value, promote the transport of fluid bodies from one to other regions of space , which results in a great mixing or uniformity capacity, several orders of magnitude greater than the molecular level diffusion, which is the only one present in a laminar regime. These bodies of fluid in disorderly motion are called eddies, corresponding to wind gusts, in atmospheric flows.

Nevertheless, a statistical approach may be adopted, if the flow is treated with proper averaging techniques. Reynolds averaging (ensemble-average) is a well-known technique in which a phenomenon is tested several times and the results are averaged together. A time series of a generic quantity can be decomposed into a mean value and a fluctuating part using this technique:

$$u(x,t) = \overline{U}(x,t) + u'(x,t) \tag{2.1}$$

This is called Reynolds decomposition. If the Navier-Stokes equation are rewritten by decomposing the velocity in its mean and fluctuating parts and then averaged, the Reynolds Averaged Navier-Stokes (RANS) equation are obtained.

$$\vec{\nabla} \cdot \vec{U} = 0 \tag{2.2}$$

$$\frac{\partial \vec{U}}{\partial t} + \vec{\nabla}(\vec{U}\vec{U}) = -\frac{1}{\rho}\nabla p + \nabla \cdot (2\nu \vec{\vec{E}}) - \underbrace{\vec{\nabla} \cdot \left\langle \vec{u'}\vec{u'} \right\rangle}_{\text{Reynolds stresses}} \tag{2.3}$$

The underlined element is known as the Reynolds stresses tensor, and it is responsible for the generation of turbulence. The Reynolds stresses, in particular, trigger a process in which the kinetic energy of the flow is transported into the turbulent field through a inviscid processes and dissipated through the viscosity.

2.1.2 Energy Cascade

The concept of the energy cascade (introduced by Richardson in 1922 [25]) states that through a production mechanism, the kinetic energy enters the turbulence at the largest scales of motion as a result of the high velocity gradients in a three-dimensional field. This energy is then transferred (by inviscid process of stretching vortex tubes) to smaller and smaller scales until, at the smallest scales, the energy is dissipated by viscous action.

In brief, Richardson's first conclusion was that turbulence is made up of eddies of varying sizes ℓ . The largest ones are characterized by a length scale ℓ_0 which is comparable to the flow scale $\mathcal{L}$ and their characteristic velocity $u_0 \equiv u(\ell_0)$. According to Richardson, such eddies are unstable and undergo a break-up process, transferring energy to smaller eddies until the motion is stable and the Reynolds number is low enough for viscosity to take over[26].

Kolmogorov (1941) [27] quantified this theory based his notions over three fundamental hypothesis. In particular he identified the smallest scales of turbulence to be those that now bear his name.

Kolmogorov's hypothesis of local isotropy *At sufficiently high Reynolds number, the small-scale turbulent motions ($\ell \ll \ell_0$) are statistically isotropic.*

Based on this, a boundary length scale ℓ_{EI} can be defined as the demarcation between the anisotropic large eddies ($\ell > \ell_{EI}$) and the isotropic small eddies ($\ell < \ell_{EI}$). In light of this, Kolmogorov argued that, just as the directional information of large scales is lost as energy passes down the cascade, all information about the geometry of large eddies (determined by the mean flow field and boundary conditions) is also lost. As a consequence, the statistics of the small-scale motions are universal, similar in every high-Reynolds number turbulent flow. This leads to next Kolmogorov's hypothesis.

Kolmogorov's first similarity hypothesis *In every turbulent flow at sufficiently high Reynolds number, the statistics of the small-scale motions ($\ell < \ell_{EI}$) have a universal form that is uniquely determined by ν and ε*

The size range $\ell < \ell_{EI}$ is called *universal equilibrium range*. In this range, the time scales $\ell/u(\ell)$ are small compared with ℓ_0/u_0, allowing the small eddies to quickly adapt to maintain a dynamic equilibrium with the energy-transfer rate $\mathcal{T}_{EI}$ imposed by the large eddies.

By performing a dimensional analysis using the two parameters ν and ε, the characteristic length, time and velocity scales can be formed. These are the Kolmogorov scales:

$$\eta \equiv (\nu^3/\varepsilon)^{1/4} \tag{2.4}$$

$$u_\eta \equiv (\varepsilon\nu)^{1/4} \tag{2.5}$$

$$\tau_\eta \equiv (\nu/\varepsilon)^{1/2} \tag{2.6}$$

The ratios of the smallest to largest scales can be easily determined using the Kolmogorov scales above and from the scaling $\varepsilon \sim u_0^3/\ell_0$.

$$\eta/\ell_0 \sim \mathrm{Re}^{-3/4} \tag{2.7}$$

$$u_\eta/u_0 \sim \mathrm{Re}^{-1/4} \tag{2.8}$$

$$\tau_\eta/\tau_0 \sim \mathrm{Re}^{-1/2} \tag{2.9}$$

Evidently, at high Reynolds number, the velocity scales and time scales of the smallest eddies are small compared with those of the largest eddies.

From Equation 2.7 it can be see that, the ratio η/ℓ_0 decreases with increasing of Re. As a consequence, at sufficiently high Reynolds number, there is a range of scales ℓ that are very small compared with ℓ_0, and yet very large compared with ν. Since eddies in this range are much bigger than the dissipative eddies, it may be supposed that their Reynolds number is large, and consequently insensible to viscous effects.

Hence, following from this and from the first similarity hypothesis, Kolmogorov stated his last hypothesis:

Kolmogorov's second similarity hypothesis - *In every turbulent flow at sufficiently high Reynolds number, the statistics of the motions of scale ℓ in the range $\ell_0 \gg \ell \gg \nu$ have a universal form that is uniquely determined by ε.*

The length scale ℓ_{DI} divide the universal equilibrium range ($\ell < \ell_{EI}$) into two subranges: the *inertial subrange* ($\ell_{EI} > \ell > \ell_{DI}$) and the *dissipation range* ($\ell < \ell_{DI}$). As the name suggests, according to the second similarity hypothesis, in the inertial subrange the motion is determined by inertial effects.

In the conception of the energy cascade, a quantity of central importance – denoted by $\mathcal{T}(\ell)$ – is the rate at which energy is transferred from eddies larger than ℓ_{EI} to those smaller than ℓ_{DI}. It is shown that for both ℓ_{EI} and ℓ_{DI} , the energy transfer rate throughout the inertial subrange is equal to the dissipation range. This means that the inertial subrange has a constant rate of energy flux. From Kolmogorov's second hypothesis:

$$\mathcal{T}_{\mathrm{EI}} \equiv \mathcal{T}\left(\ell_{\mathrm{EI}}\right) = \mathcal{T}(\ell) = \mathcal{T}_{\mathrm{DI}} \equiv \mathcal{T}\left(\ell_{\mathrm{DI}}\right) = \varepsilon \tag{2.10}$$

In summary, the energy cascade process is depicted in figure 2.2 The largest eddies in a high-Reynolds number flow are unstable and go through a break-up process. The kinetic energy is fed into the energy-containing range by mean of a production mechanism ($\wp$) and then "injected" into the inertial subrange, which exhibits constant energy transfer within the largest scales ℓ_{EI} and dissipation scales ℓ_{DI}. Following that, the eddies enter the dissipation range, where the associated Reynolds number is low enough to consider viscosity effects. Finally, once the Kolmogorov scale η is reached, the kinetic energy is dissipated by viscous actions through the Dissipation ε [23].

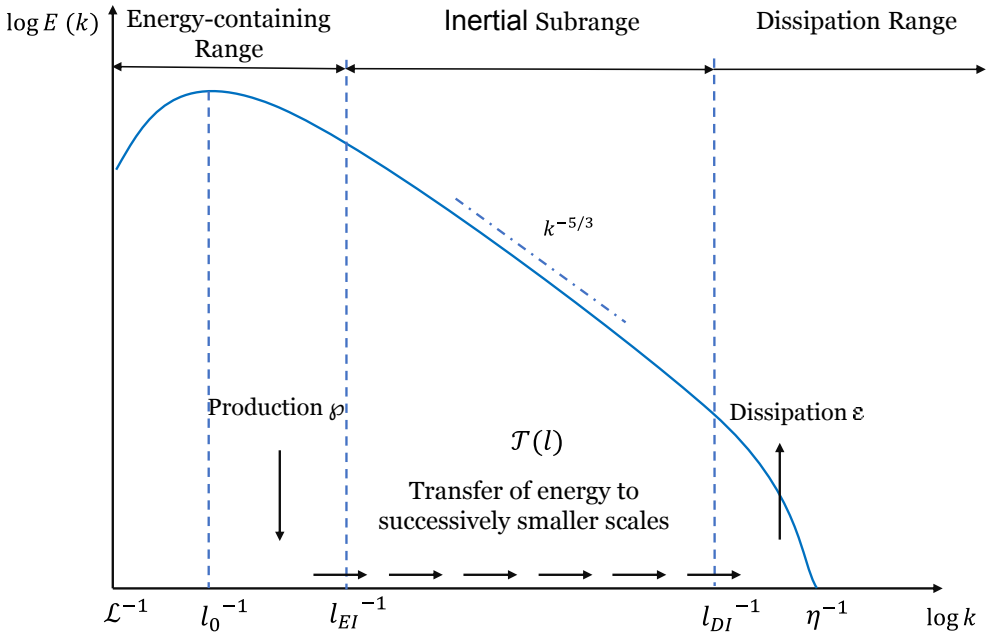

Figure 2.2: Energy cascade process

To determined how the turbulent kinetic energy is distributed among the eddies of different sizes, the most easily way, for homogeneous turbulence, is considering the energy spectrum function $E(\kappa)$. From the second hypothesis it follows that, in the inertial range, the spectrum is:

$$E(\kappa) = C\varepsilon^{2/3}\kappa^{-5/3} \tag{2.11}$$

where C denotes a universal constant. According to equation 2.11, the energy distribution over the wavelength spectrum of a turbulent flow in the inertial subrange has a $-5/3$ slope decay.

Although the Kolmogorov -$5/3$ spectrum applies only to the inertial range, the observations are consistent with the notion that the bulk of the energy is in the large scales ($\ell > \ell_{EI}$), and that the bulk of the dissipation is in the small scales ($\ell < \ell_{DI}$).

2.1.3 Statistical description of turbulent flows

A common mistake is to attribute incorrectly additional significance to the designation 'random'. An event A is defined as random if it is neither certain nor impossible. That a time-series velocity signal $U(x,t)$ is a random variable means only that it does not have the same value at each time instant that the experiment is repeated under the same set of conditions, C. Despite the deterministic nature of classical mechanics equations, turbulent flows, which must obey the Navier-Stokes equations, have a random and unpredictable nature. This can be seen in two observations:

1. In any turbulent flow there are, unavoidably, perturbations in initial conditions, bound-

ary conditions, and material properties;

2. Turbulent flow fields are extremely sensitive to such perturbations.

Despite its chaotic nature, turbulence can be described using a statistical approach. Any deterministic model used for turbulence modeling is, in fact, based on statistical data. As a result, only statistical measurements can accurately characterize a turbulent flow. A statistical description of turbulence includes correlation functions, probability density function and spectra characterization. This way a turbulent flow can be fully appreciated [23] .

The statistical moments of turbulence are computed considered a discrete instantaneous turbulent signal of velocity sampled with a frequency f_s, resulting in N samples. Since only the longitudinal velocity u is measured, all the following equations refer to this component. The first central moment is the mean velocity, which is computed as:

$$\overline{U} = \frac{1}{N}\sum_{i=0}^{N} u_i \tag{2.12}$$

The second central moment is the variance. In turbulence research the root mean square (RMS) of the velocity fluctuations is most often used, which is the positive square root of the variance of a signal:

$$\overline{u'} = \sqrt{\frac{1}{N}\sum_{i=0}^{N}\left(u_i(t) - \overline{U}\right)^2} \tag{2.13}$$

Through equations 2.12 and 2.13, is possible to define the turbulence intensity of the flow according to:

$$Tu = \frac{\overline{u'}}{\overline{U}} \tag{2.14}$$

High-order statistical moment may be defined by introducing the *Probability Density Function*, which quantifies the probability with which the samples of a velocity signal $u(t)$ are included within a certain band around the mean value U. A signal that is completely random has a Normal (or Gaussian) distribution around the mean. Similarly, a steady turbulent flow exhibit the same distribution with the centre corresponding to the peak and a standard deviation equal to the RMS. In order to assess and describe the shape and the deviation of the actual distribution with respect to the Gaussian one, the third and fourth statisical moments are introduced. The third central moment, the skewness, is computed as follow:

$$\text{Skewness } = \frac{1}{N}\sum_{i=0}^{N}\frac{(u_i(t) - \bar{U})^3}{\overline{u'}^3} \tag{2.15}$$

The Skewness is a measure of the lack of symmetry of the signal distribution with respect to the Gaussian distribution. Value different from zero means distribution more skewed to

the left (positive skewness) or right (negative skewness). The fourth central moment, is the Kurtosis (equation 2.16) and it gives an indication of the flatness of the distribution. High values of Kurtosis imply that the fluctuations are sparse around the mean.

$$\text{Kurtosis } = \frac{1}{N}\sum_{i=0}^{N}\frac{(u_i(t)-\bar{U})^4}{\overline{u'}^4} \tag{2.16}$$

A turbulent signal is not truly random, it possesses a certain degree of correlation. This means that, if only a one-component velocity signal is considered, the instantaneous velocity value at that specific time instant $u(t)$ is not completely independent of the velocity at preceding instants. This feature is called autocorrelation and represents the degree of correlation between the fluctuating velocity components u at two different instants separated by a time interval τ. The autocorrelation degree is expressed by the Autocorrelation function (ACF), computed as follow:

$$ACF = \frac{\overline{u(t)u(t+\tau)}}{\overline{u(t)^2}} \tag{2.17}$$

The integral time scale gives an estimate of the time interval for which the velocity signal is correlated. This parameter is calculated as:

$$T_{\text{int}} = \int_0^\infty ACF(\tau)\mathrm{d}\tau \tag{2.18}$$

The autocorrelation properties lead to the determination of Integral Length Scales (ILS). The ILS are defined as the length scales of the energy-containing eddies of the energy spectrum (figure 2.2). Once the signal is no longer autocorrelated, the macroscopic information are lost. Therefore the integral length scale are defined as the smallest scales to which the signal at one instant can correlate with a point at another instant, hence the smallest scale before the turbulent kinetic energy is fed into the inertial subrange.

Using Taylor's frozen rotor hypothesis [28] the integral length scale can be calculated by multiplying the integral time scale by a convective velocity, which is usually assumed to be the local mean velocity.

$$\Lambda_x = T_{\text{int}}\,\overline{U} \tag{2.19}$$

where Λ_x represent the integral length scales based on a one-component velocity signal.

As the experimentally obtained autocorrelation coefficients often exhibit wide oscillations around zero, integrating for the entire signal duration can produce incorrect results. As a result, different options for the upper integration limit of equation 2.18 have been proposed: the time lag for which the amplitude of the function decreases to e^{-1}; or the time lag corresponding to the first root [29]. Oscillations cause an unreliable computation of the integral

time scale, particularly for short time intervals. Assuming the Taylor frozen vortex hypothesis, Roach [30] proposed an alternative method for calculating the integral scale from the power spectrum:

$$\Lambda_x = \left[\frac{E(f)\overline{U}}{4\overline{u'^2}}\right]_{f\to 0} \tag{2.20}$$

The micro length scale η, also known as Kolmogorov length scale, is considered representative of eddies that dissipate turbulent energy. It can also be computed according to Roach [30] as:

$$\eta = \left[\frac{\overline{U}^2\overline{u'^2}}{2\pi^2 \int_0^\infty f^2 E(f)\mathrm{d}f}\right] \tag{2.21}$$

2.2 Principles of Boundary Layer theory

L. Prandtl (1904) introduced the boundary layer or frictional layer as a transition that takes place in a thin layer close to the wall, at large Reynolds number. Close to the wall, viscosity plays an important role in the flow dynamics, and it must be accounted for in order to satisfy the no-slip condition, and thus zero velocity at the wall. As will be shown, the boundary layer is thinner the higher the Reynolds number, i.e. the smaller the viscosity. As a result, the concept of the boundary layer implies that flows with high Reynolds numbers can be divided into two main regions regions: the outer flow (bulk), in which the viscosity may be neglected and the boundary layer, in which the viscosity takes over and must be taken into account.

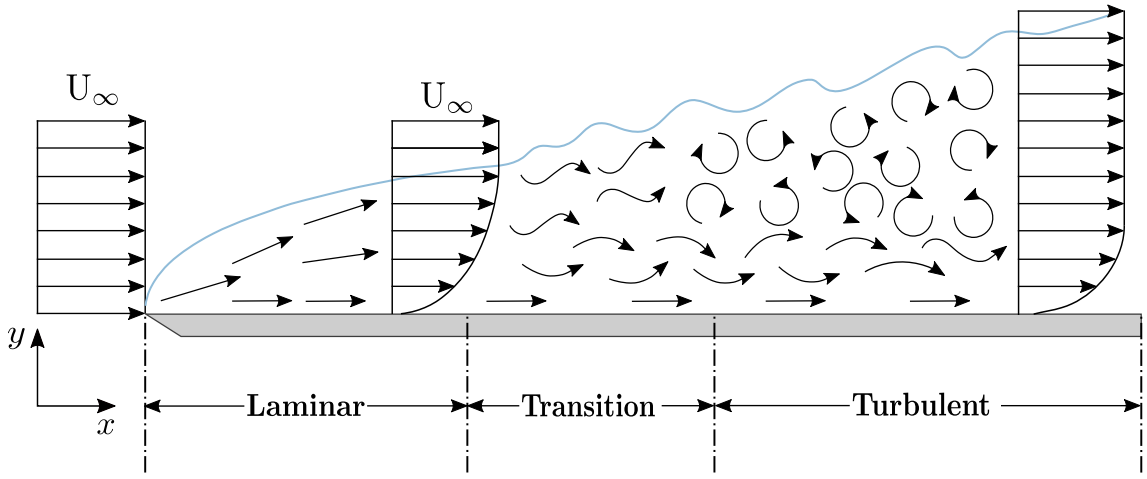

Figure 2.3: Laminar-to-turbulent transition of the boundary layer in thin flat plate [23]

Figure 2.3 shows the development of the boundary layer on a flat plate. It can be seen that goes through three different states. Initially, the velocity streamlines follow the main inlet flow, and the boundary layer exhibits laminar behavior. As the distance increases, some vertical disturbances occur, and the boundary layer becomes transitional. Then the boundary

layer becomes turbulent as a result of these vertical disturbances taking over and resulting in a vortex-structured flow.

Different methods are used in order to define the thickness of the boundary layer. A first approach is to define the boundary layer extension as the height at which the velocity reaches 99% of the inviscid solution U. This method is referred to as boundary layer thickness δ_{99}. Despite the simplicity and the intuitive nature of δ_{99}, this is a poorly conditioned quantity, since it depends on the measurement of a small velocity difference. More reliable are integral measures such as the displacement thickness (δ_1 or δ^*). It represents how much the wall should be displaced in an hypothetical inviscid solution that has the same mass flow-rate of the real one [31]. For a compressible flow, it is defined as follow:

$$\delta_1 = \int_0^\infty \left(1 - \frac{\rho(y)U(y)}{\rho_\infty U_\infty}\right) dy \tag{2.22}$$

where y is the wall-normal coordinates. In a wall bounded flow, the upper limit of the integral is replaced with the height of the channel/pipe. A similar parameter is the momentum thickness (δ_2 or θ), important in the von Karman integral solution (1921). It is derived analogously as the displacement thickness, but instead of an inviscid solution with the same mass-flow rate as the real one, an hypothetical inviscid velocity profile with the same momentum mass-flow rate is taken. For a compressible flow, it is expressed as follow:

$$\delta_2 = \int_0^\infty \frac{\rho(y)U(y)}{\rho_\infty U_\infty}\left(1 - \frac{U(y)}{U_\infty}\right) dy \tag{2.23}$$

The ration between the displacement thick and the momentum thickness defines the shape factor H:

$$H = \frac{\delta_1}{\delta_2}$$

It indicates the status of the boundary layer. For a flat plate, $H = 2.59$ denotes a laminar boundary layer and $H \simeq 1.6 - 1.7$ stands for turbulent boundary layer [31].

As with the boundary–layer thickness, the wall shear stress τ_w of the plate can also be estimated. According to Newton's law of friction we have:

$$\tau_\mathrm{w}(x) = \mu \left(\frac{\partial u}{\partial y}\right)_\mathrm{w} \tag{2.24}$$

where μ is the dynamic viscosity of the fluid and w denotes the value at the wall.

Therefore the normalized wall shear stress by a reference dynamic pressure, $\frac{1}{2}\rho U_\infty^2$, is called skin friction coefficient c_f and is defined as:

$$c_f = \frac{\tau_\mathrm{w}}{\frac{1}{2}\rho U_\infty^2} \tag{2.25}$$

Two distinct momentum transport mechanisms operate in the boundary layer and the bulk

flow. To study them while keeping the distinction, a two-dimensional analysis based on lengths and velocities is required to define the quantities that can characterize the two regions. The frictional velocity is one of the first results of this analysis, and it is defined as follows:

$$u_\tau = \sqrt{\frac{\tau_w}{\rho}} \tag{2.26}$$

The viscous length scale is defined by the ratio of the flow's dynamic viscosity ν to its frictional velocity:

$$\delta_\nu = \frac{\nu}{u_\tau} \tag{2.27}$$

The mean velocity profile can be expressed in wall units by scaling the velocity $\overline{U}$ and the wall normal coordinate y by the frictional velocity and viscous length scales, respectively.

$$u^+ = \frac{\overline{U}}{u_\tau} \tag{2.28}$$

$$y^+ = \frac{y}{\delta_\nu} \tag{2.29}$$

Following the Prandtl hypothesis (1925), these quantities can be used to calculate the law of the wall and define equations that describe the mean velocity profile in the boundary layer (figure 2.4).

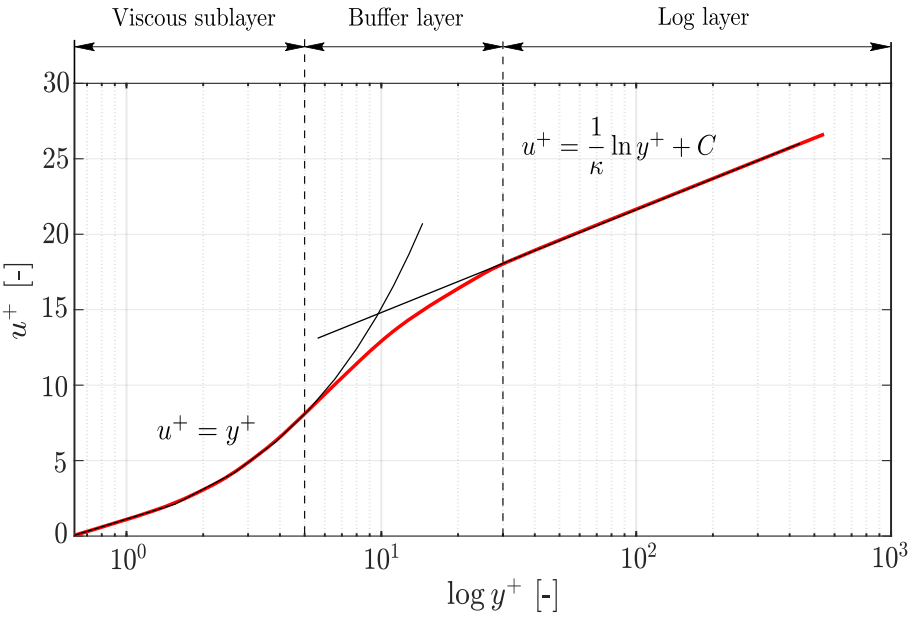

Figure 2.4: Turbulent boundary layer in terms of wall units y^+–u^+

According to Pope [26] the following rough delimiting of the boundary layer can be made:

- *Inner layer* ($y/\delta < 0.1$): in this zone the greatest part of viscous stress are focused. Its thickness is usually 10% to 20% of the total thickness.

- *Outer Layer* ($y^+ > 50$): this region accounts for the remaining 80% to 90% of the total thickeness. It contains big vortex structures and a reduced turbulence production, being the velocity gradients very reduced in magnitude.

- *Overlap region* ($y^+ > 50$, $y/\delta < 0.1$): at sufficiently high Reynolds number exist a region of overlap between inner and outer layers. In the overlap region the mean velocity profile must be logarithmic. In fact the log law is a good approximation beyond the overlap region.

Therefore, the following regions can be considered:

- Viscous sub-layer, $0 < y^+ < 5$, region characterized by a linear trend with a slope of $45°$, where:

$$u^+ = y^+ \tag{2.30}$$

- Buffer Layer, $5 < y^+ < 30$, it is the transition region between the viscosity-dominated and the turbulence-dominated parts of the flow. The nondimensional velocity profile u^+ within the buffer layer mostly relies on curve fitting, because an analytical formula is not readily available for describing the relationship between u^+ and y^+.

- Log-law region, $y^+ > 30$, $y/\delta < 0.3$, formulated by Theodore von Karman (1930), on the assumption that, for large y^+ the viscosity has little effect. It can be shown that the following trend holds:

$$u^+ = \frac{1}{k} ln(y^+) + C \tag{2.31}$$

  where k is the von Karman constant, usually taken as 0.41 and C is a constant ($C \simeq 5.2$)

Explaining the concept and procedure by which these laws are retrieved is beyond the scope of this study. More information is available in Schlichting's [31] and Pope's [26] books. The boundary layer's region and their properties are summarized in table 2.1

Table 2.1: Wall regions and their defining properties

Region	Location	Equation	Description
Inner layer	$y/\delta < 0.1$	-	U determined by u_τ and y^+, independent of U_0 and δ
Viscous sub-layer	$0 < y^+ < 5$	$u^+ = y^+$	Shear stress essentially driven by viscosity.
Buffer layer	$5 < y^+ < 30$	-	Transition between the viscous sublayer and the log-law region. Viscous and turbulent contribution to the overall shear stress are comparable.
Log-law region	$y^+ > 30$,$y/\delta < 0.3$	$u^+ = \frac{1}{k} ln(y^+) + C$	Shear stress essentially driven by turbulence (Reynolds stress).
Outer layer	$y^+ > 50$	-	Direct effects of viscosity on U are negligible

Chapter 3

Experimental campaign

3.1 The VKI S-1/C wind tunnel

The experimental campaign was carried out in the von Karman Institute for Fluid Dynamics in S-1/C high-speed wind tunnel, which is schematically represented in figure 3.1.The facility consists of a closed-loop circuit driven by a 615 kW axial compressor, which controls the total amount of mass-flow by adjusting its rotational speed, while the mass flow passing through the test section can be adjusted by a 500 mm by-pass valve. The flow downstream of the compressor passes through a cooler in order to keep the total temperature close to ambient one. As a result, no heat transfer occurs between the inside and outside of the facility. The operating pressure inside the facility is regulated by means of a vacuum pump, which can reduce the rig's absolute pressure until 8000 Pa. The combined action of compressor and vacuum pump allows the Reynolds and Mach number to be varied independently within the facility.

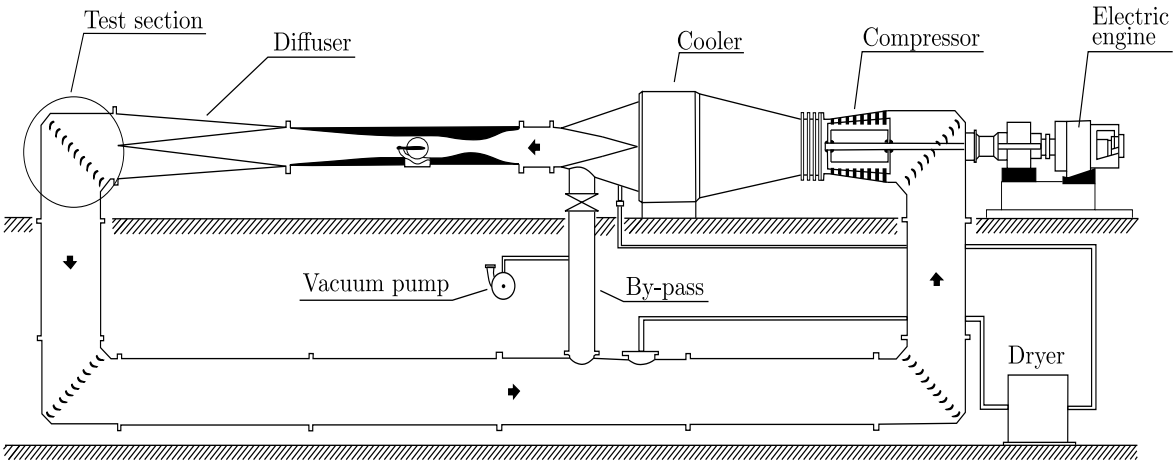

Figure 3.1: The von Karman Institute's S1-C wind tunnel

Previously, the wind tunnel was used to conduct external aerodynamic studies, and it was later modified to accommodate a linear cascade. As a result, an LPT cascade test section (figure 3.2) was installed following the diffuser, replacing the left elbow of the facility. The cylindrical part upstream of the diffuser serves as a settling chamber for the cascade test section in this new configuration, providing a homogeneous inlet flow conditions by means of wire meshes and honeycombs.

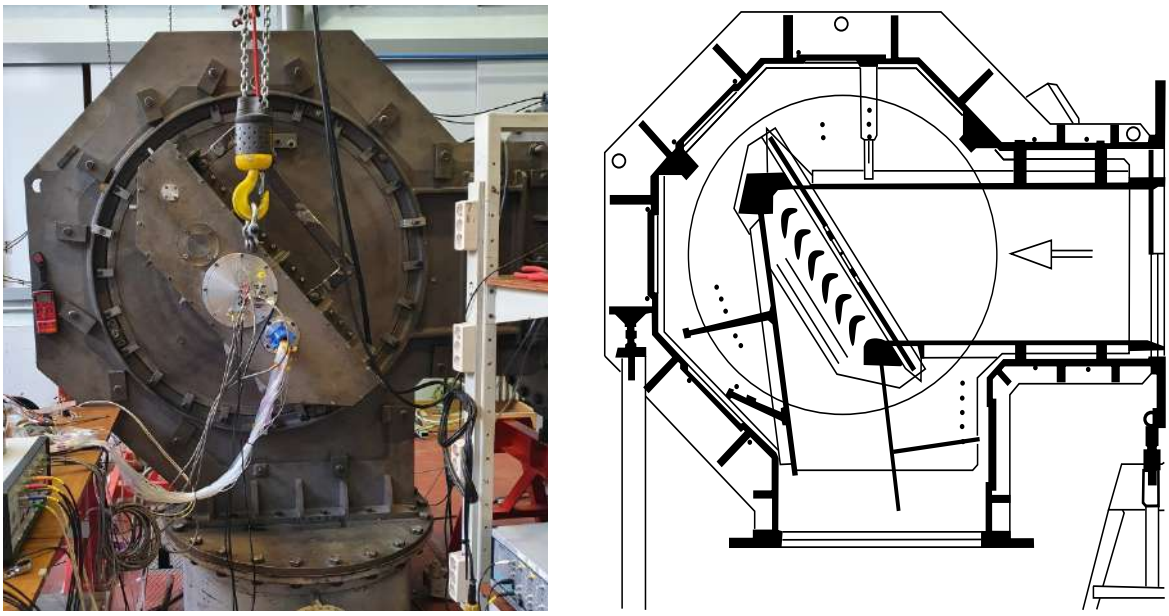

Figure 3.2: Detailed illustration of the test section. Linear cascade housing (left). Technical illustration of the test section (right)

3.2 Cascade test section

The test section's is equipped with vertical and lateral contractions, allowing the transition between the original circular parts of the wind tunnel and the cascade. The height is adjustable within 375 and 650 mm, while the maximum width is 225 mm, which corresponds to the span of the blade. This way, the span is sufficiently high to ensure a proper aspect ratio of the blade in order to have a two-dimensional flow at midspan.

Figure 3.3: Hot-wire placed in traverse the support system

The test section is equipped with a motor-driven traversing system which allows to obtain

pitchwise measurements upstream and downstream of the blades. The support system is placed outside of the cascade and the probes are inserted in the test section through slots on the cascade side wall. Two slots are available, one upstream and one downstream of the blades, so that both the inlet and outlet flow to the cascade can be investigated. Nevertheless, the present work took place during the first and second part of the project were just upstream measurements were preform.

In figure 3.3 the support system is shown, with the hot-wire probe inserted into the test section through the upstream slot. For the upstream measurements, the head of the probe was set at blade midspan and aligned with the axial inlet flow.

3.2.1 Cascade instrumentation and measuring planes

For a better representation of the measurements location, a coordinate system (figure 3.4) has been defined. The origin of the axis is located at the intersection between leading edge of the central blade and the endwall. The endwall containing the coordinate system's origin will now be referred to as the cavity endwall, while the opposite endwall will be referred to as the upper endwall.

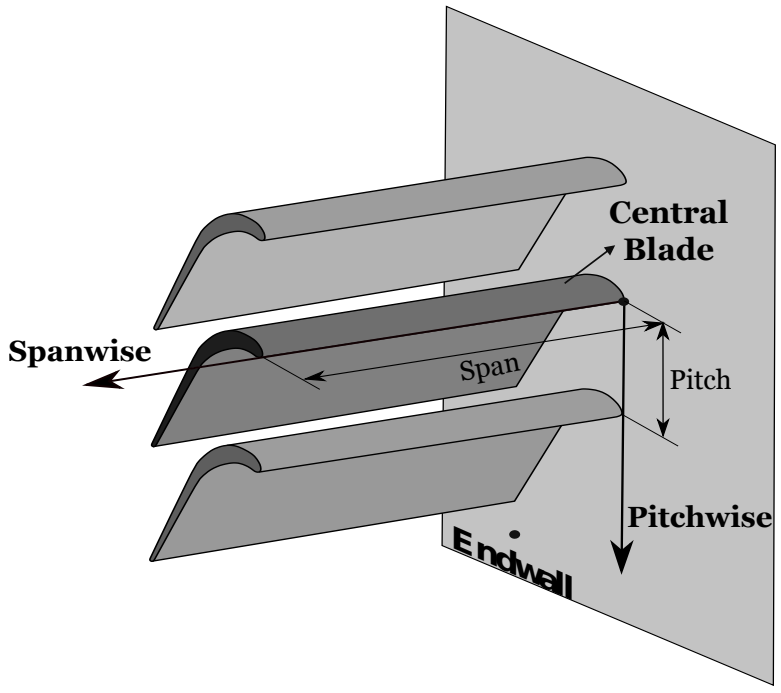

Figure 3.4: Coordinate system

Therefore, two axes have been introduced:

- Spanwise direction, from the cavity endwall to the upper endwall;
- Pitchwise direction, running from blade to blade and positive towards the blades below the central one.

The cascade is permanently instrumented to provide the basic flow quantities required to set the operational conditions. The measurement points are arranged in planes upstream and downstream of the cascade, as shown in figure 3.5.

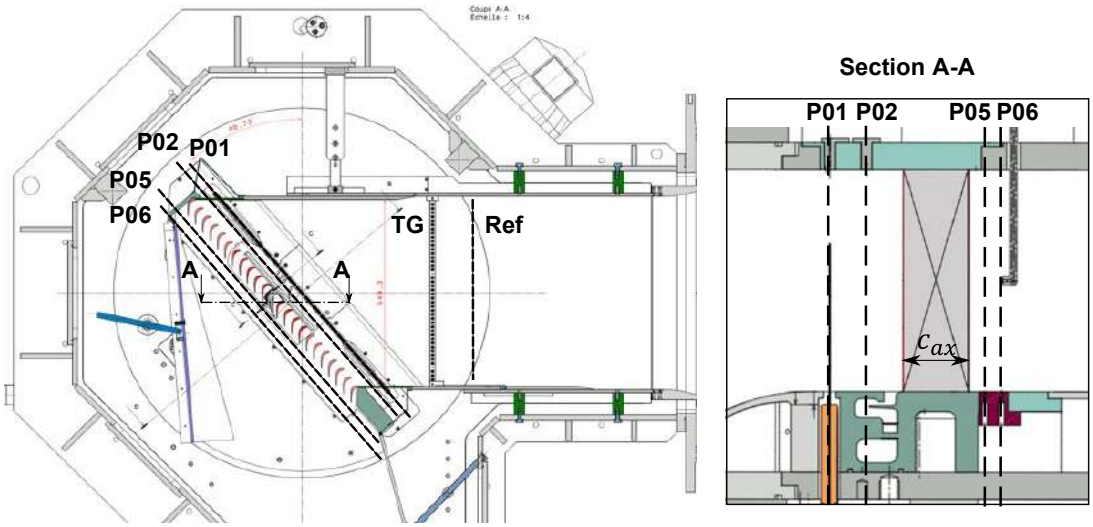

Figure 3.5: Measurement Plane front view (left) and top view (right)

Table 3.1: Measurements plane arrangement

Plane	Location	Position	Reference
01	Upstream	$1.125c_{ax}$	LE
02	Upstream	$0.5c_{ax}$	LE
05	Downstream	$0.25c_{ax}$	TE
06	Downstream	$0.5c_{ax}$	TE

Reference Plane

This plane provides the reference information of the total pressure and total temperature needed to determine the flow conditions in the other planes. It is permanently instrumented with:

- a type-K thermocouple that measures the total temperature of the flow $T_{0,ref}$, and which is assumed to be uniform throughout the test section's flow field since the facility works in adiabatic conditions;

- two Pitot tubes providing the total pressure of the flow, $P_{0,ref}$. To ensure redundancy in total pressure measurements, the two probes are linked to separate pressure transducers via different pressure lines. A WIKA P-30, absolute pressure sensor, is used for the primary measurement. The redundancy measurement provided by the second Pitot tube is provided by two separate pressure transducers: a Validyne DP15-42 differential pressure sensor and an MPS4264 Scanivalve pressure scanner, with the primary measurement of the WIKA P-30 serving as the reference pressure.

Upstream and Downstream planes

Throughout the project SPLEEN, six planes (excluding the reference plane) are object of investigation. Nevertheless, for the sake of simplicity, only plane 01, 02, 05 and 06 will be considered in this section. Their arrangement is reported in table 3.1 and can be visualize in Figure 3.5. They are the effective measurement planes, where the different probes are positioned during the experimental campaign. Each one of this planes, except for plane 02, is instrumented with an array of 31 static pressure taps, providing the static pressure at different pitch positions. While the pressure taps on planes 05 and 06 are placed on the cavity endwall, in plane 01 and 03 the pressure taps are featured with removable slots placed on the upper endwall. The static pressure is fed via pneumatic tubes to two MPS4264 Scanivalves pressure scanners. They are an array of 64 differential pressure traducers that allow to measure a pressure difference in a range of 1 psi and 2.5 psi, for upstream and downstream planes respectively. The management of the different channels changes from test to test, depending on the probes, their location and the planes involved during the test. All the information, pneumatic and electric, are fed to the Analog-to-Digital (A/D) acquisition board for the digitalization of the analogical signal.

In the present work, the hot-wire probe is positioned at plane 02 for the mapping of the turbulence field at the inlet of the cascade. The choice of placing the hot-wire probe at plane 02 lies on the fact that plane 01 will be hosting the wake generator during the unsteady phase of the campaign.

3.2.2 Passive Turbulence Grid

A passive turbulence generator grid (TG) is adopted in order to increase the free-stream turbulence intensity (FSTI) at the cascade inlet. Previous investigations conducted in S-1/C by Michàlek et al [32], state that the inlet natural levels of FSTI achieved by the facility is around 0.9%. They used a double crossed hot-wire located at an axial distance of $0.95x/c_{ax}$ upstream of the LE of the central blade.

The turbulence grid (figure 3.6) consists in 41 cylindrical rods of 3 mm in diameter, with a spacing between their centre-lines of 12 mm (mesh size), resulting in a geometric solidity of 0.25. The grid can be positioned at different stream-wise positions upstream of the cascade, specifically between the reference plane and plane 01, in order to regulate the turbulence intensity at a prescribed plane downstream. It is placed perpendicular to the test section's intake, which means that the axial distance between the grid and the blades varies from blade to blade. This yields to a turbulence intensity decay trend along the pitchwise direction. Due to the decay of the FSTI, the axial distance between the TG and the central blade is crucial in order to achieve the desired FSTI.

Over the past years, the study of turbulence generation by means of passive grids by several authors allowed the derivation of different decay laws characterizing the turbulence decay

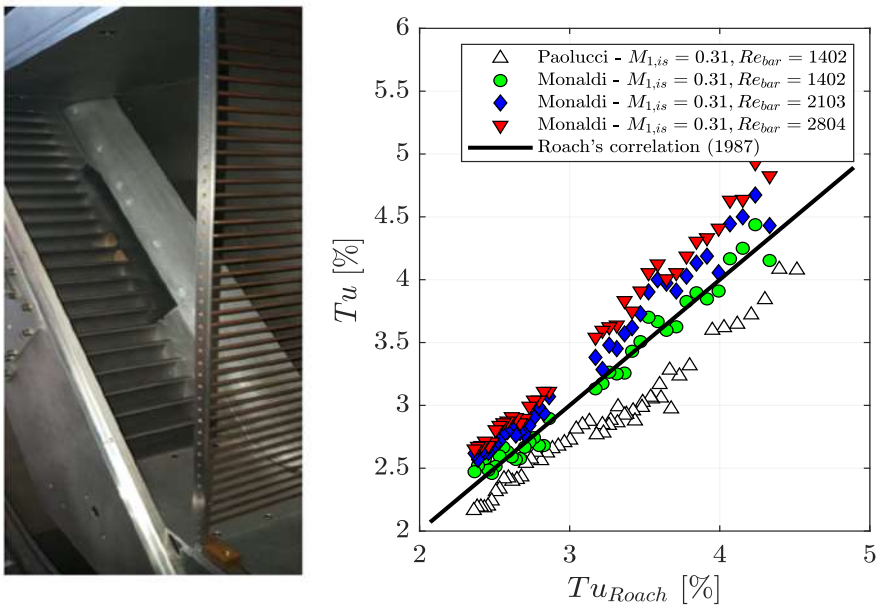

Figure 3.6: Passive TG present in the VKI S-1/C (left) and comparison between the correlation proposed by Roach [30] and previous experiments (right)

after the grid. Roach [30] addressed this problem by assessing the decay laws proposed by Batchelor [33] and Frenkiel [34] and proposed a law solely dependent on the grid geometry. This power law allows to estimate the decay of the FSTI as a function of the distance to the grid and the grid rod diameter:

$$Tu = C \left(\frac{x}{d}\right)^{-\frac{5}{7}} \tag{3.1}$$

where C is a constant dependent on the grid geometry (0.80 for a grid with parallel circular bars), x is the downstream distance from the grid location and d is the diameter of the grid rods. This correlation was previously investigated at VKI in the same facility by Monaldi [35] and Paolucci [36], who found a good agreement with the experimental data as shown in figure 3.6.

By following Roach's methodology, the TG has been experimentally set to 400 mm away from the LE of the central blade in order to achieve a desired turbulence intensity level of 2.5%.

3.2.3 Wake Generator

To fully simulate the rotating environment of an axial turbine, the test section is equipped with an upstream high-speed rotating bar system (figure 3.7), able to simulate the blade-row interference effects due to wake-blade interactions. The wake generator (WG) consists of a disc of 625 mm diameter equipped at its periphery with cylindrical bars made of molybdenum. The rotating disc can be mounted with 96, 48, 32, 24, 16 bars. The number and diameter of the bars as well as the rotational speed of the disk are adjustable to match a requested Strouhal number (St). The rotating bars are only parallel to the blade leading edge (LE) when passing in front of the central blade. In this position, the bars extend over most

of the entire blade span except for a clearance to the opposite wall. Leakage flows at the passage of the bars through the upper and lower tunnel walls are minimized by sealed cavities to avoid spurious recirculation between the upstream and downstream area of the cascade. The generator is lodged in a large semi-circular housing mounted on one of the circular cascade sidewalls. The WG is driven by a 30 kW electric motor up to 3500 rpm which corresponds to a bar passing velocity at blade midspan of ~ 165 m/s, providing therefore an engine similar velocity triangle and a correct flow coefficient, as opposed to the systems using a linear bar displacement system. The latter is most often limited in displacement velocity and provides, in engine-like high-speed compressible flow conditions to be reproduced, values of the flow coefficient which are much too high.

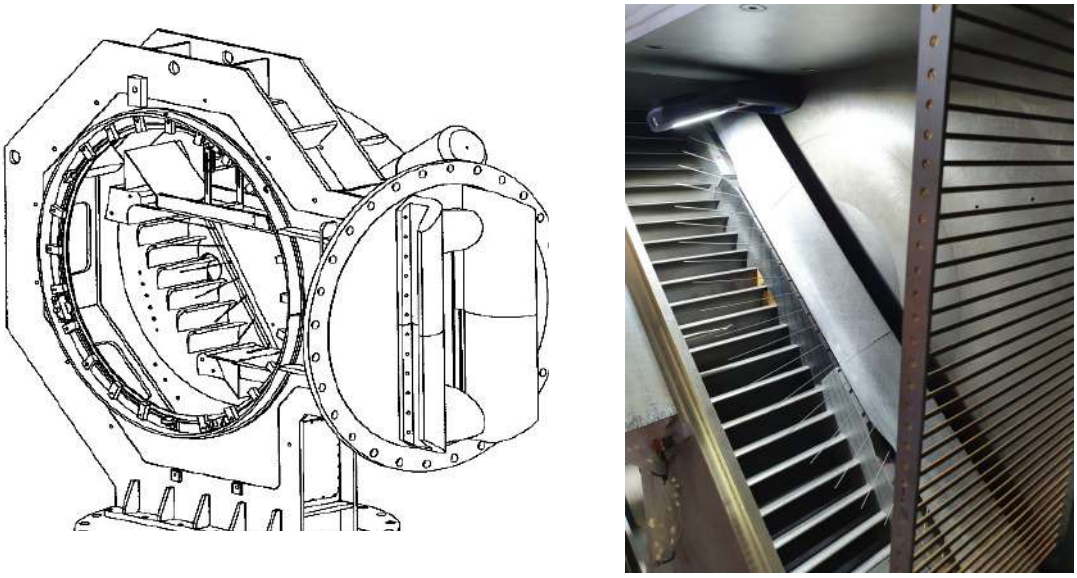

Figure 3.7: Technical illustration of the WG (left) and test section final arrangement with TG and WG (right)

The selection of the number of bars to be mounted in the WG arises from the need to match the Strouhal number range envisaged for the experimental campaign (St $\in [0.6;1.2]$). The Strouhal number is a dimensionless parameter that define the performability of an unsteady environment and can be computed as:

$$St = \frac{RPM}{60} N_{\text{bars}} \frac{c}{V_{2,is}} \tag{3.2}$$

It can be seen that, in order to maintain a specified Strouhal number, decreasing the numbers of bars will require an increase in the rotational velocity.

The Strouhal number was requested to be kept constant. Therefore, it was concluded that the Strouhal number for the SPLEEN experimental campaign is 0.95, for a bar length of 130 mm and 1.0 mm of diameter. To achieve a Strouhal number equal to 0.95, the rotational velocity of the motor is 3209 RPM. And finally the WG can only have 96 bars to fulfill the previous requirements.

3.2.4 Total pressure drop coefficient

A total pressure loss occurs across the TG and the WG, this means that the inlet total pressure at the cascade inlet, referred as $p_{0,int}$, is lower than the reference total pressure, $p_{0,ref}$. In order to account this loss, a correlation between the two planes has been developed.

The pressure drop coefficient across the turbulence grid, Y_{TG}, can be defined as:

$$Y_{TG} = \frac{P_{0,\text{ ref}} - P_{0,\text{ int}}}{P_{0,\text{ ref}}} \tag{3.3}$$

Where $P_{0,ref}$ is the total pressure upstream of the turbulence grid and $P_{0,in}$ is the total pressure downstream of the turbulence grid and upstream of the WG.

The pressure drop coefficient across the WG, Y_{WG}, can be defined as:

$$Y_{WG} = \frac{P_{0,\text{ int}} - P_{01}}{P_{0,\text{ int}}} \tag{3.4}$$

Where P_{01} is the total pressure downstream of the WG and upstream of the cascade. This quantity is not measured in real time for all the tests but can be measured during measurements involving a probe at the given location.

The determination of the total pressure drop coefficient across the turbulence grid and WG can be expressed as:

$$Y_{\text{tot}} = Y_{TG} + Y_{WG} - Y_{TG}Y_{WG} \tag{3.5}$$

Once these loss terms are known, the inlet total pressure to the blade cascade can be evaluated through the following equations, depending on whether the turbulence grid or the periodic WG or both are used:

$$\text{No TG - No WG} : P_{0,\text{ in}} = P_{0,\text{ ref}} \tag{3.6}$$

$$\text{TG - No WG} : P_{0,\text{ in}} = (1 - Y_{TG}) \cdot P_{0,\text{ ref}} \tag{3.7}$$

$$\text{TG - WG} : P_{0,\text{ in}} = (1 - Y_{\text{tot}}) \cdot P_{0,\text{ ref}} \tag{3.8}$$

3.2.5 Operating conditions

The flow conditions in the test section are characterized by the isentropic exit Mach and Reynolds numbers. The isentropic exit Mach number is computed by the inlet total pressure $P_{0,in}$ and the exit static pressure $P_{out,s}$, by the isentropic relationship:

$$M_{out,is} = \left\{ \frac{2}{\gamma - 1} \left[\left(\frac{P_{0,in}}{P_{out,s}} \right)^{\frac{\gamma-1}{\gamma}} - 1 \right] \right\}^{0.5} \tag{3.9}$$

The two quantities required to compute $M_{out,is}$ are the cascade outlet static pressure, $P_{out,s}$, and total pressure upstream of the cascade, $P_{0,in}$. The $P_{out,s}$ is determined by means of the pressure taps situated downstream of the blades TE.

The cascade outlet static temperature is computed from the previously determined $M_{out,is}$, and $T_{0,in}$ which is acquired by means of a K-type thermocouple. Knowing these two quantities, the following isentropic equation can be used to determine $T_{out,s}$:

$$T_{out,s} = \frac{T_{0,out}}{1 + \frac{\gamma-1}{2} M_{out,is}^2} \tag{3.10}$$

From $M_{out,is}$ and $T_{out,s}$, the isentropic velocity $V_{out,is}$ is computed as follows:

$$V_{out,is} = M_{out,is} \sqrt{\gamma R T_{out,s}} \tag{3.11}$$

In order to compute the Reynolds number, the density $\rho_{out,is}$ and the dynamic viscosity $\mu_{out,is}$ are needed. They can be calculated with the ideal gas relationship and the Sutherland's law respectively:

$$\rho_{out,is} = \frac{P_{out,s}}{R T_{out,s}} \tag{3.12}$$

$$\mu_{out,is} = \mu_{ref} \frac{T_{ref} + S}{T_{out,s} + S} \left(\frac{T_{s,6}}{T_{ref}} \right)^{1.5} \tag{3.13}$$

where $\mu_{ref} = 1.716 \times 10^{-5} \mathrm{kgm^{-1}\,s^{-1}}$ is the dynamic viscosity at $T_{ref} = 273.15K$ and $S = 110.4K$.

Using the previous quantities, the outlet Reynolds, $Re_{out,is}$, can be computed:

$$Re_{out,is} = \frac{\rho_{out,is} V_{out,is} c}{\mu_{out,is}} \tag{3.14}$$

where c is blade's chord length.

The experimental campaign on which this thesis focuses has the following nominal conditions:

• Nominal Outlet isentropic Mach number: $M_{out,is} = 0.9$.

• Nominal Outlet isentropic Reynolds number: $Re_{out,is} = 70000$.

Figure 3.8: Auxiliary pressure instrumentation.Cobra-shaped 5-Hole Pressure probe (left), Valydine DP15-42 (center) and Scanivalve MPS4264 (right)

3.3 Auxiliary Pressure Measurements

As previously stated in section 3.2, the facility is equipped with a pneumatic pressure system that provides support for the measurements with hot-wires (and other probes) concerning the flow conditions inside and outside of the boundary layer.

The pressure measurement system can be divided into a probe, which transmits the pressure information, through a specifically designed pressure line, and a sensor that takes this information and converts it into an electrical signal. To be more specific, the sensor is merely a component of the entire instrument whose sole purpose is to provide an output voltage signal and commonly referred to as a pressure transducer.

In this section, the auxiliary pressure sensors and probes which served as support for the hot-wire test campaign are presented hereunder.

3.3.1 Pneumatic 5-Hole Pressure Probe (5HPP)

The hot-wire measurements for the boundary layer investigations were supported and compared using a 5-Hole Pressure Probe (5HPP), depicted in figure 3.8. This type of probe is commonly used in turbomachinery applications for steady measurement: their low frequency response makes them unsuitable for detecting flow fluctuations, but their design has been refined over time and allows them to capture well mean flow values [37].

A 5HPP, as the name implies, is a probe whose head has 5 holes, one in the center of the head, oriented normally to the main flow, and the other four lie on a slanted plane, symmetrically opposed. Each one of the pressure lines are connected to a channel of the Scanivalve and by means of a static and an aerodynamic calibration, the output is converted in velocity and flow angles quantities. These measurements will serve as a reference and comparison for the results of boundary layer and measurements with the wake generator, where it is impossible to know the mean flow values in the plane between the hot-wire and the WG.

3.3.2 Differential Pressure Transducers

A transducer is a device that transforms a signal from one energy form to another energy form. In the present test campaign, a Validyne DP$15-42$ and two Scanivalve MPS4264 were used, in which a pressure difference is fed to the sensor and subsequently converted into an electric signal (voltage).

Validyne DP$15-42$

The Validyne DP$15-42$, shown in figure 3.8, is a variable-reluctance pressure transducer that is widely used in experimental fluid dynamics. A variable reluctance transducer consists of a diaphragm of magnetically permeable stainless steel clamped between two blocks of stainless steel. Embedded in each block is an inductance coil on an E-shaped core. In the undeflected position, the diaphragm is centered with equal gaps between it and the legs of each E-core to provide equal reluctances. A pressure difference applied through the pressure ports deflects the diaphragm toward the cavity with the lower pressure, decreasing one gap and increasing the other. As the magnetic reluctance varies with the gap and determines the inductance value of each coil, the diaphragm deflection increases the inductance of one coil and decreases that of the other. The difference in the inductances of the coils is demodulated into a voltage output, which is then converted into a pressure measurements through a linear calibration law.

Scanivalve MPS4264-Miniature Pressure Scanner

The *Scanivalve MPS*4264 (figure 3.8),is a unique 64 channel pressure scanner versatile enough to be used for many applications. Each one of these channels has a miniaturized piezoresistive pressure sensor that has the ability to change its electrical resistance when subjected to a mechanical strain. The scanivalve acquisition works sequentially, which means that each channel is sampled individually for a defined sampling period before starting the acquisition of the next channel, until the 64 channels have been sampled. The MPS4264 scanner is a complete data acquisition system that integrates all electronic components for the analog-to-digital signal conversion. Therefore, it only requires a low current DC power supply and an Ethernet connection to connect to the computer.

In the presented investigation, the two Scanivalve MPS4264 Miniature Pressure Scanner are used to acquire pressure information concerning:

- reference total pressure $p_{0,ref}$;
- static pressure measured from the wall taps in relation to the various measurement planes;
- pneumatic probes that can be connected.

Chapter 4

Hot- Wire Anemometry

4.1 Introduction

4.1.1 Physical operating principle

The operation of Hot-Wire Anemometry (HWA) is based on the establishment of a convective heat transfer from a heated sensor to the surrounding fluid. This heat transfer can be converted into a fluctuating output voltage and by means of a calibration, can be related to instantaneous flow velocity, density and total temperature, for a given probe/fluid.

The heat balance for an electrically heated wire, without taking into account the contributions of conduction and radiation is formulated as follow [38]:

$$\frac{dc_w}{dt}T_w = P - Q \tag{4.1}$$

In equation 4.1 the derivative term represents the heat stored in the wire by means of its thermal inertia, in which c_w and T_w are the specific heat and the temperature of the wire, respectively. P is the electrical power supplied to the wire and Q is the thermal power. This equation can expressed the convective heat transfer and can be expanded to:

$$\frac{dc_w}{dt}T_w = I^2 R_w - hA_w\left(T_w - T_{heat}\right) \tag{4.2}$$

where I is the current supplied to the wire, R_w is the resistance of the wire, h is the convective heat transfer coefficient, A_w is the external surface of the wire and T_{heat} is the recovery temperature, which is the temperature "felt" by the wire, thus the temperature that drives the heat transfer process. The recovery factor η defines the ratio between the recovery temperature and the flow total temperature T_0, according to:

$$\eta = \frac{T_{heat}}{T_0} \tag{4.3}$$

The recovery factor is essentially influenced by the Knudsen number and the Mach number [8]. The Knudsen number express the deviation from the continuum flow as the ratio between the molecular mean free path and a characteristic length of the flow (the wire diameter in the hot-wire case). It may be expressed as a function of both Mach and Reynolds

number [39]:

$$Kn = \frac{\lambda}{d_w} = \frac{M}{\mathrm{Re}}\sqrt{\frac{\pi\gamma}{2}} \tag{4.4}$$

The singularities and limitations of the HWA application in different flow conditions are well summarized in a review paper by Stainback and Nagabushana [38], where the following flow regimes are distinguished (in terms of Mach number):

- $M < 0.3$ subsonic incompressible flow
- $0.3 < M < 1.4$ subsonic compressible, transonic and low supersonic flow
- $M > 1.4$ high supersonic flow

within which, one can distinguish the following three flow sub-regimes (in terms of Knudsen number):

- $Kn < 0.01$ continuum flow
- $0.01 < Kn < 0.1$ slip flow
- $Kn > 0.1$ free molecule flow

The Knudsen number is also a function of the flow conditions [8], while in incompressible continuum flows its effect is negligible ($T_{heat} \approx T_0$), it should be taken into account in compressible and slip flows, since the Knudsen number strongly influences the heat transfer process due to the gas rarefaction.

In the present study, the Knudsen number is near to the bottom bound of the slip flow regime, due to the high speeds and low densities of the flow. Dewey [39] proposes an empirical correlation for the recovery factor (see section 4.2). A correlation of this type can be used with confidence for a wide range of Knudsen and Mach numbers [39]. Equation 4.2 may now be written as follow:

$$\frac{dc_w}{dt}T_w = I^2 R_w - \pi l_w k \left(T_w - \eta T_0\right) Nu \tag{4.5}$$

where Nu is the Nusselt number, which defines the ratio between convective and conductive heat transfer:

$$Nu = \frac{h d_w}{k} \tag{4.6}$$

where h is the heat transfer coefficient, d_w is the wire diameter and k the thermal conductivity

of the fluid. The Nusselt number depends on the following dimensionless quantities:

$$Nu = f(Re, M, Pr, Gr, \tau_w, \alpha, \beta, \frac{l_w}{d_w}) \tag{4.7}$$

where Re, M, Pr and Gr are the Reynolds, Mach, Prandtl and Grasshof numbers of the flow respectively. τ_w is the overheat ratio, α and β are the two flow angles, l_w and d_w are the length and diameter of the sensor.

4.1.2 Anemometer's modes of operation

There are three distinct modes of operation in HWA: the constant current anemometry (CCA), the constant temperature anemometry (CTA) and the constant voltage anemometry (CVA). Although CVA is under development, CCA and CTA are mature and have been widely implemented. References [8] and [40] provide more information on hot-wire anemometry.

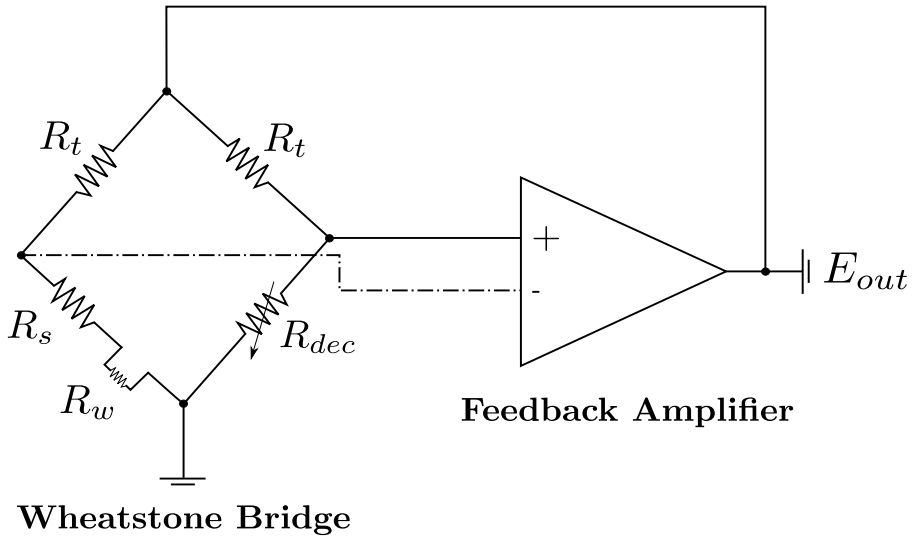

Figure 4.1: Constant Temperature Anemometer electrical scheme

Constant Current Anemometry

Constant current anemometry (CCA) is the oldest type of HWA. The control circuit is a Wheatstone bridge, in which the hot-wire represents one of the legs. In the CCA, the system is fed with a constant current and the unbalance voltage across the bridge is then related to the heat transfer from the wire which changes its resistance. In other words the fluctuating heat transfer is obtained from resistance fluctuations of the wire. The main drawbacks of this approach are due to the thermal inertia of the sensor that limits the frequency response, hence a non-uniform compensating amplifier is necessary. This makes the CCA laborious to use [8].

Constant Temperature Anemometry

The Constant Temperature Anemometer, of which the electrical scheme is shown in figure 4.1, is similar to CCA. The difference lies in the fact that CTA uses a fast response feedback amplifier which varies the feeding current of the wire's leg of the Wheatstone bridge in order to keep the wire's resistance and thereby its operational temperature, constant. The heat

transfer from the wire is related to the bridge top voltage, so feedback amplifier reads the unbalance voltage and modifies the bridge top voltage (hence the wire heating) until the balance is restored.

By keeping the mean wire temperature constant, the effect of thermal inertia seen in CCA is negligible, which is the main advantage of CTA. Therefore, Equation 4.2 can be rewritten expressing the feeding current of the wire in terms of wire voltage E_w, the final form of the heat balance over a heated thin wire in CTA application is:

$$\frac{E_w^2}{R_w} = \pi l_w k \left(T_w - \eta T_0\right) Nu \tag{4.8}$$

Constant Voltage Anemometry

One of the more recent developments in HWA is the constant voltage anemometer (CVA), patented in 1991 by Sarma [41]. It is still under development and the methodology is not as mature as CCA or CTA, so it is very expensive and less commercial. In this technique, the voltage across the wire is kept constant, and any change in wire resistance due to instantaneous heat transfer causes a current change through the wire. Kegerise [42] compared CTA and CVA measurement techniques and according to the study, CVA has a larger frequency bandwidth, as well as slightly higher velocity and temperature sensitivities than CTA, indicating a higher signal-to-noise ratio.

4.1.3 Hot-Wires Probes

A single sensor hot-wire is presented in figure 4.2. The sensor is typically a fine wire with a diameter between 5 and 10 μm, a total length of 1 to 4 mm, welded on two prongs, usually made of stainless steel or Nickel. The active length of the wire can be extended entirely to the tip of the prongs or to a restricted central region, which is smaller than the total length, by using coated wire ends that approach the prongs. The main advantage of using a coating is that it reduces heat losses to the prongs while increasing spatial resolution [8].

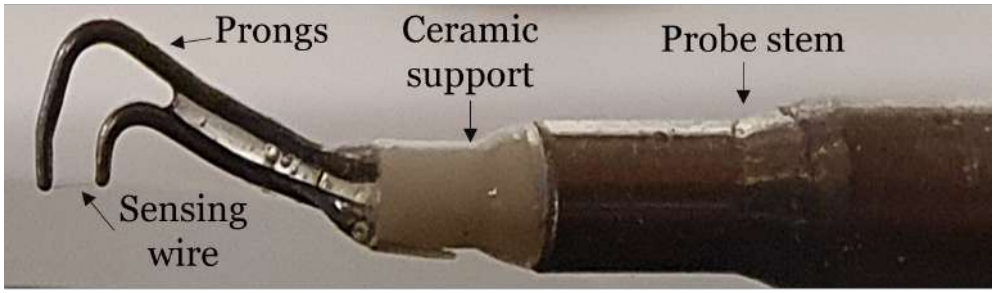

Figure 4.2: Hot-wire probe illustration

The sensor material should feature a high temperature coefficient of resistance α_w, with common materials being tungsten, platinum-based alloys and Platinum-Nickel [8].

The sensor resistance R_w at a temperature T_w is then given by the following expression:

$$R_w = R_{ref}[1 + \alpha_w(T_w - T_{ref})] \tag{4.9}$$

where R_{ref} is the sensor resistance at a reference temperature T_{ref}, high values of α_w express high sensitivity to temperature fluctuations.

The selection of the materials, the design and the main features of the probe are typically based on the type of fluid to be investigated, the characteristics of the flow and the external constrains of the experimental setup [23]. The hot-wire probe depicted in figure 4.3 was used in this investigation. It is a single straight Tungsten Gold-plated wire with a diameter of 9μm and an active length of 0.7mm on a total length of 1.16mm.

The hot-wire probe is essentially a chain of resistances. As depicted in figure 4.2, the main components are: the sensor, the prongs, the support (includes all of the components between the prongs and the cable.) and the cable. If one of the resistances changes, the calibration changes, it is therefore extremely important that the experimental configuration used during the measurements is accurately replicated in the calibration process.

Figure 4.3: Probe mounted on the external calibrator (left) and wire detail (right)

4.1.4 Dantec Dynamics Streamline Pro CTA

The anemometer shown in figure 4.4, is operated through a dedicated software provided by Dantec Dynamics called Streamware Pro. It consists in six integrated and independent modules. Each one of the modules consist in a CTA control circuit (Wheatstone bridge + feedback amplifier) followed by a signal conditioner.
A single module can operate independently from the others, allowing to use six probes at six different operating temperatures at the same time . The operating temperature of the wire is imposed by an user-input parameter, the overheat ratio τ_w, which is defined by the equation:

$$\tau_w = \frac{R_w - R_{w,cold}}{R_{w,cold}} = \alpha_w(T_w - T_{ref}) \tag{4.10}$$

where R_w is the operational resistance of the wire, $R_{w,cold}$ is the resistance of the wire measured at the reference temperature T_{ref} , T_w is the operating wire temperature and α_w is the

wire specific temperature coefficient of resistance, measured at $20°C$.

In order to obtain $R_{w,cold}$, the system performs a measurement of the total resistance of the hot-wire probe assembly and subtracts the user input information of the resistances of cables, support and prongs, which were previously measured with an high precision multimeter. The system measure T_{ref} via a dedicated thermocouple plugged into the CTA frame.

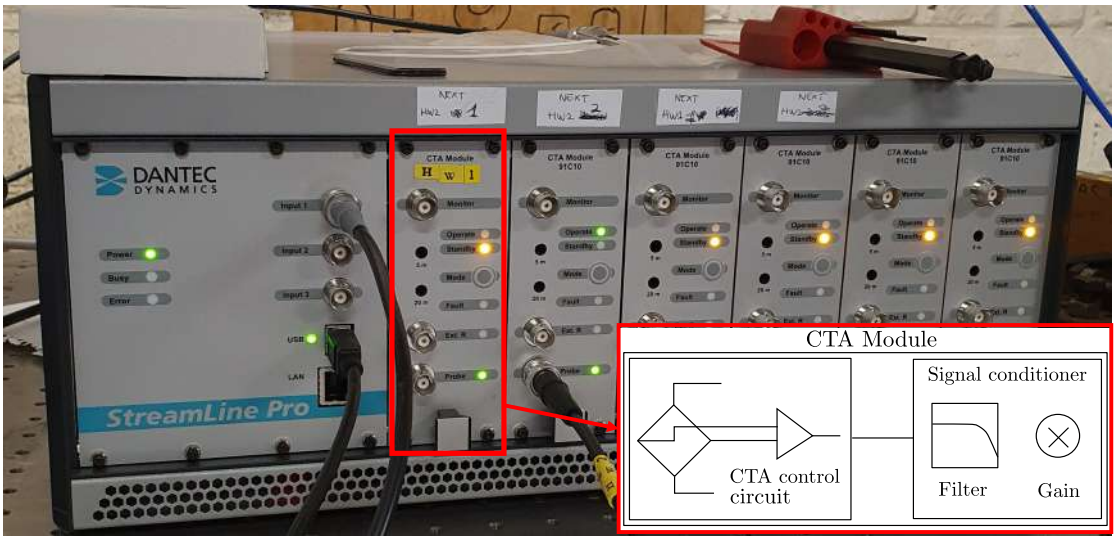

Figure 4.4: Dantec Dynamic Streamline Pro Constant Temperature Anemometer

According to the definition (equation 4.10), the overheat ratio depends on the cold wire resistance ($R_{w,cold}$) ,and thus on the temperature at which the latter has measured, which is typically the ambient temperature. Therefore, a change in ambient temperature, with a corresponding change in cold wire resistance, causes the bridge to change the operational wire resistance (R_w) in order to maintain the imposed overheat ratio. This has the unfortunate consequence of varying the hot-wire temperatures throughout the test campaign. However, the Streamline Pro offers the possibility to change the system settings to a predefined setup (chosen a-priori by the operator). By using the setup in which the cold wire resistance has been measured, as default, the following measurements will be referring to same reference temperature and resistance. As a result, the hot-wire operating temperature remains constant.

The overheat ratio has to be chosen accordingly to the flow temperature expected during the measurements. In order to have a good sensitivity to velocity, the ratio T_w/T_{ref} should be equal or higher than 1.5 (with the temperatures expressed in Kelvin) [8]. To prevent the oxidation of the wire, the temperature should not exceed $270 \sim 300°C$ for a wire made with Tungsten.

The facility (S-1/C) operates a nearly ambient temperature conditions (for long testing times the facility heats up to $40 \sim 50°C$), thus the wire does not need a particularly high overheat ratio.

Table 4.1: Overheat ratio setup parameters

τ_w	0.76
$R_{w,cold}$	0.79Ω
T_{ref}	20.46°C
α_w	0.36%
T_w	231.46°C

For the present study the overheat ratio was reduced until the temperature of the wire was around $230°C$, with T_{ref} of $20.46°C$ measured by the system, obtaining $\tau_w = 0.76$. This way in the the worst case scenario, corresponding to $T_{ref} = 323.15K$ $(50°C)$, the ratio T_w/T_{ref} its equal to 1.56. The previous mentioned overheat ratio settings are summarized in table 4.1.

4.1.5 Dynamic response

The dynamic response of the system is defined by the properties of the wire and the CTA frame. To test the frequency response of the probe a square-wave test can be performed. The test consists in a current pulse submitted in the circuit (usually at the diagonal of the Wheatstone bridge) and monitoring the output voltage response in an oscilloscope, as depicted in figure 4.5. The system is then tuned to achieve an optimal response, similar to a second order system. According to Freymuth [43] the optimal response shape is achieved when the response has a 15% undershoot relative to the maximum (figure 4.5). This generates an extra-heat, which is dissipated by the wire, and the system's response is modulated in order to tune the feedback amplifier's performance. As a result, the square-wave test must be carried out at the maximum expected velocity during the measurements.

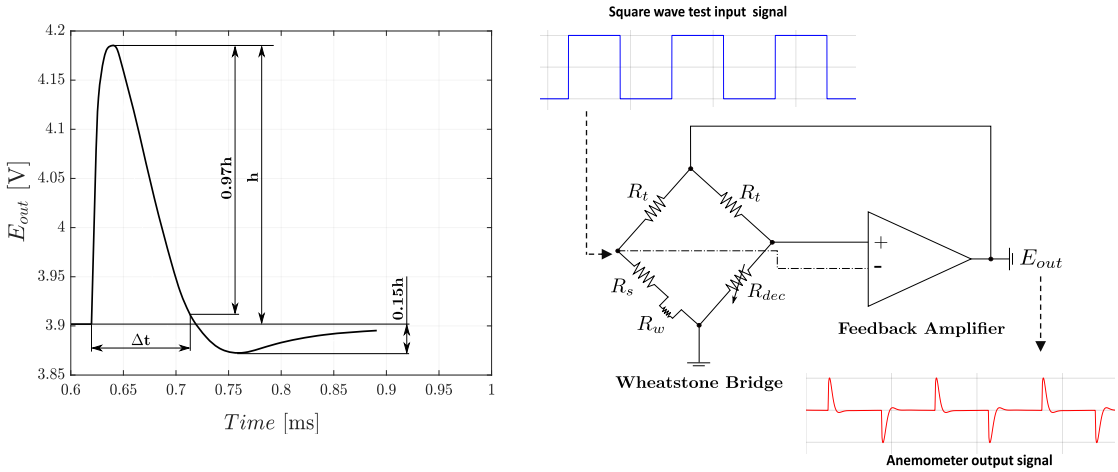

Figure 4.5: Anemometer time response to square wave test: optimal shape (left) and a schematic of square wave test (right)

The square-wave test provides an estimation of the cut-off frequency f_c of the system through the following expression proposed by Freymuth [43]:

$$f_c \approx \frac{1}{1.3\Delta t} \tag{4.11}$$

where Δt is the time when the amplitude is decreased at 3% of the peak value.

The frequency response is primarily determined by the wire diameter. In the current study, the Square-Wave Test was carried out at the maximum velocity achieved during the hot-wire calibration, which was around 155 m/s. The frequency response, which was displayed in real-time on the Streamware Pro dedicated window, was within $7 \sim 10$ kHz for a wire of $9\mu m$. The square wave test value represents the bandwidth in which the wire's response is maximum and flat. As the signal to noise ratio becomes lower than one at frequencies higher than the cut-off, therefore, a low-pass filter of 30kHz was applied to the corrected signal.

A square wave testing unit is implemented in most commercial anemometers and include at least two control parameters that allow the user to adjust the response. In the Dantec system used in the present study, these controls are the gain and filter setting of the feedback amplifier and the cable compensation, which balances the capacitance and inductance on both legs of the Wheatstone bridge. Following that, the signal must be adjusted to match the A/D board's specifications by modifying the Offset and Gain in the system.

4.2 Calibration methodology

The non-dimensional calibration approach proposed by Cukurel et al. [21] was followed in this study. This method employs an effective wire temperature and empirical correlations to eliminate the dependency of the calibration on total temperature and Mach number of the flow respectively, which allows establishing a unique Nu-Re calibration curve [5]. Therefore, this methodology can be divided into two steps: the low-speed calibration and the mass-flux calibration, which will be described in this section.

For constant temperature anemometry, with a specified probe geometry (l_w/d_w=const), with the wire normal to the flow (no angular dependency), in a specific fluid with moderate flow temperature variations (Pr = const), and by neglecting the natural convection ($Re < Gr^{0.3}$) [8], the functional relationship 4.7 reduces at:

$$Nu = f(Re_w, M) \tag{4.12}$$

where Re_w is the Reynolds number based on the wire diameter and is defined as follow:

$$Re_w = \frac{\rho U d_w}{\mu} \tag{4.13}$$

Rearranging equation 4.8 in terms of the anemometer bridge output voltage E_b, the Nusselt number can be calculated according to:

$$Nu = \frac{E_b^2}{\pi l_w k \left(T_w - \eta T_0\right)} \frac{R_w}{\left(R_t + R_s + R_w\right)^2} \tag{4.14}$$

where, in CTA applications, all the resistances are constants. The thermal conductivity k is

computed with the 0.7 power law:

$$k = k_{20}\left(\frac{T_0}{T_{20}}\right)^{0.7} \tag{4.15}$$

where $k_{ref} = 0.0257\, Wm^1K^1$ and $T_{20} = 293.15K$ are the reference conditions for air at $20°C$. The recovery factor η is computed with the empirical correlation proposed by Dewey [39] as a function of Mach and Knudsen number:

$$\eta = \eta_c + \eta^* (\eta_f - \eta_c) \tag{4.16}$$

$$\eta_c = 1 - 0.05\frac{M^{3.5}}{1.175 + M^{3.5}} \tag{4.17}$$

$$\eta_f = \eta_c + 0.2167\frac{M^{2.8}}{0.8521 + M^{2.8}} \tag{4.18}$$

$$\eta^* = \frac{Kn^{1.193}}{0.493 + Kn^{1.193}} \tag{4.19}$$

The bridge output voltage E_b is a function of the wire and flow characteristics. In the most generic case, the two flow angles should be included. Therefore, the bridge output voltage dependency may be expressed by the following functional relationship:

$$E_b = f(d_w, l_w, T_w, T_0, \rho, U, \alpha, \beta) \tag{4.20}$$

which, for a fixed wire geometry and if a CTA is employed (T_w = const.), yields to:

$$E_b = f(T_0, \rho, U, \alpha, \beta) \tag{4.21}$$

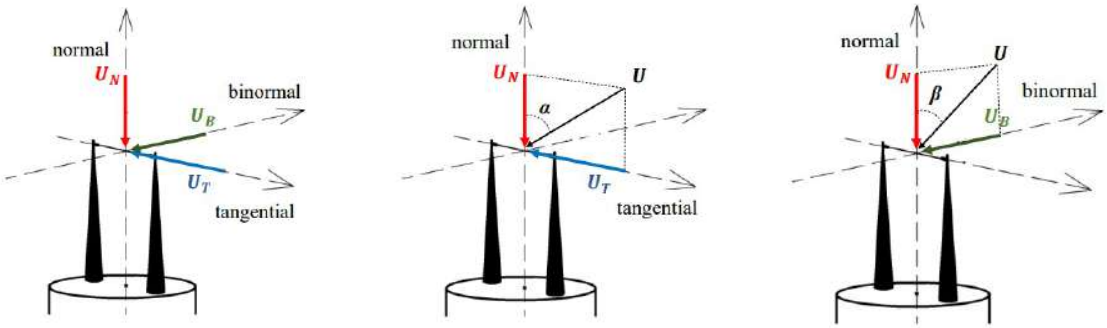

(a) (b) (c)

Figure 4.6: Directional sensitivity of a hot-wire: (a) Definition of the wire coordinate system, (b) Yaw angle defined in the normal-tangential plane, (c) Pitch angle defined in the normal-binormal plane [5]

In the wire coordinate system, the velocity vector U can be decomposed into three velocity components, as shown in 4.6a: the velocity component normal to the wire U_N, the component tangential to the wire U_T, and finally the binormal component U_B. The yaw angle α is defined in the normal-tagential plane, as shown in figure 4.6b, and the pitch angle β in the

normal-binormal plane, as shown in figure 4.6c.The wire effective velocity, defined as the velocity to which the wire is sensitive, is usually expressed as:

$$U_{eff}^2 = U_N^2 + k^2 U_T^2 + h^2 U_B \tag{4.22}$$

k and h are coefficients obtained by a directional calibration or, in some cases, provided by the probe manufacturer.

4.2.1 Low-speed calibration

The low-speed calibration is performed to identify the effective wire temperature $T_{w,eff}$. The idea is that, for a given probe in an incompressible continuum flow regime, therefore, since there is no compressibility effect, the Nusselt number is only dependent on the Reynolds number $Nu = f(Re_w)$.

Based on that, an iterative cycle takes place, where the wire temperature is systematically varied. The Nusselt number is then recomputed for each iteration and correlated with the Reynolds number. The $Nu - Re$ curve is fitted with a fourth order polynomial fitting and the R^2 of the fit is used as the selection criterion. The wire temperature to which corresponds the maximum R^2, thus the best collapse of the entire $Nu - Re$ population, is selected as the temperature that better represents the convective heat transfer process from the wire to the flow: the effective temperature of the wire.

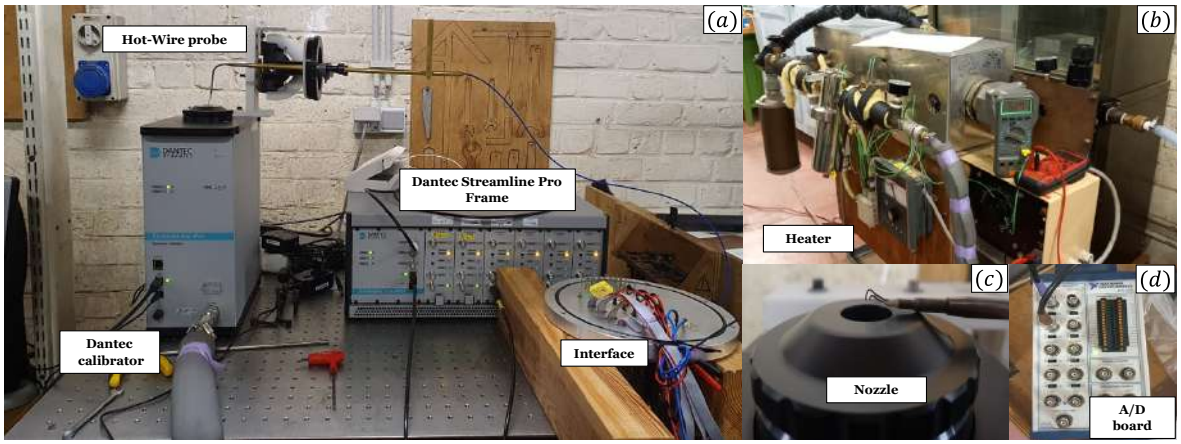

Figure 4.7: Low-speed calibration setup: (a) Overview, (b) Heating system, (c) Automatic calibrator nozzle detail, (d) Analog-to-Digital acquisition board

The procedure was carried out externally using the Dantec Dynamics Automatic Calibrator (figure 4.7a). The automatic calibratior consists in an open jet nozzle, intended for probe calibration in air and other gases from a few cm/sec up to Mach 1. Different nozzles with different throat areas are available depending on the investigated velocity range. The experimental setup is described in detail below and illustrated in figure 4.7.

The calibrator is connected to a 7 bar pressurized air supply and by controlling the pressure ratio across the nozzle allows to generate a free jet of known Mach number, where the probes

are placed during calibration. The pressurized air passes through a heater capable of heating the flow to approximately $60°C$, and then through an external filter that filters away particles and oil before being delivered to the calibrator. A precision regulator inside the calibrator ensures a stable input pressure to the flow control. The hot-wire probe is positioned with the wire in the center of the jet and aligned with the top surface of the nozzle in the same way as it will be used during measurements. The probe is connected to the CTA frame which in turn is connected to an Analog-to-Digital (A/D board) acquisition device. The latter uses digital discretization to digitalize the signal and sends it to the Streamware Pro software, which stores the calibration data in an organized file.

Once setup is complete, the operator can use Dantec Dynamics Streamware Pro software to perform a velocity calibration for different flow velocity established in the system and at different flow temperatures regulated in the heater.

The stagnation pressure, the total temperature and the velocity of the flow are directly measured inside the calibrator and stored inside the calibration output. This way the flow is fully determined and the Reynolds number may be calculated through the isentropic relationships.

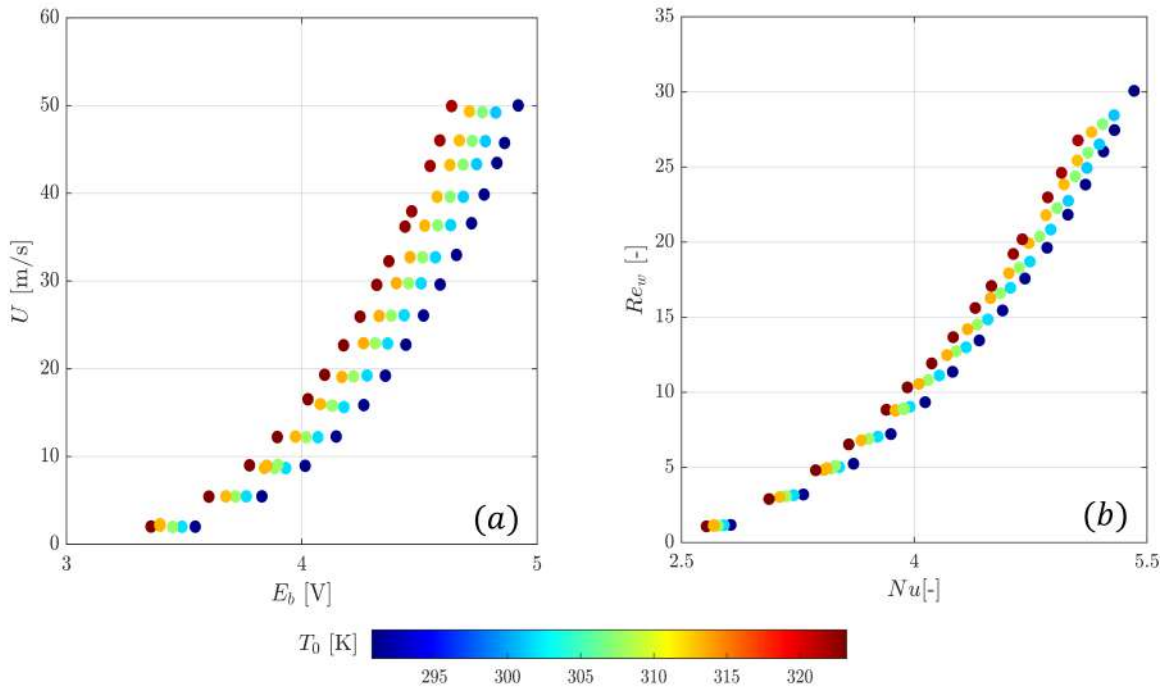

Figure 4.8: (a) Voltage-Velocity calibration for different flow temperatures, (b) Nu-Re calibration for different flow temperatures

The low-speed calibration procedure was performed for a temperature range from $T \sim 20°C$ to $T \sim 50°C$. and the results are represented in figure 4.8.

Figure 4.8a shows the results plotted in terms of voltage and velocity, a different curve is created for each temperature level and the effect of a non-isothermal flow on the heat transfer

process can be seen by a shift on the calibration curve. When the flow is heated, the convective heat exchanged between the wire and the flow decreases because the temperature difference driving the heat transfer process is lower. Figure 4.8b represents the equivalent but translated in non-dimensional parameters Re and Nu. In this case the wire temperature in the Nusselt number computation (Eq. 4.14) is retrieved by the overheat ratio definition (Eq. 4.10), which results in a wire temperature of $504.61K$ for $\tau_w = 0.76$. This wire temperature is not a good option for describing the heat transfer process, as figure 4.8b shows data dispersion based on the total temperature.

Figure 4.9 shows the outcomes of the determination of the effective wire temperature. In figure 4.9a the R^2 of the $4th$ order polynomial fit is presented as a function of the wire temperature and the selected $T_{w,eff}$, corresponding to the maximum R^2 value, resulted to be $445.25K$, witch is lower with respect to the one imposed by the overheat ratio. As depicted in figure 4.9b, when the effective wire temperature is used in equation 4.14, all the acquired data collapse a single Nu−Re curve.

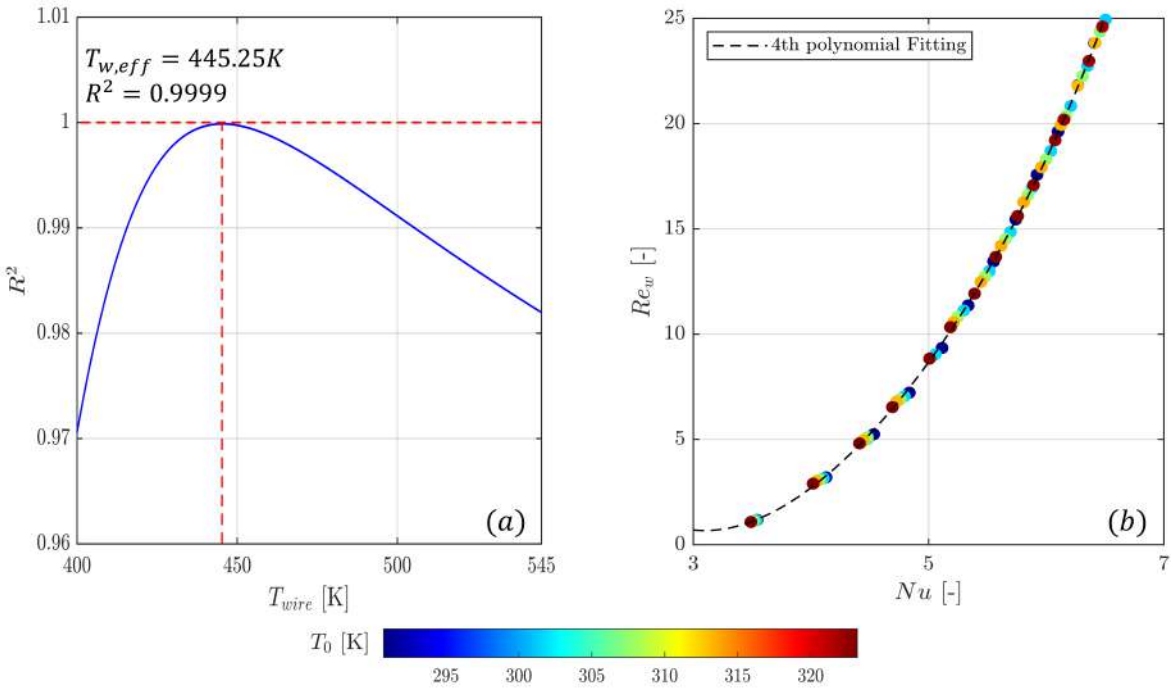

Figure 4.9: Effective wire temperature determination: R^2 as a function of the $T_{w,eff}$ (left) and collapsed Nu-Re calibration curve (right)

4.2.2 Mass-flux calibration

The S-1/C facility operates at high-speed and low-density conditions. An external facility, such as an open-jet (ex-situ) does not allow to replicate the conditions inside the wind tunnel in terms of Mach and Reynolds number. It is therefore necessary that the mass-flux calibration is performed inside the facility (in-situ).

In order to obtain a good calibration curve, a large dataset of different $NuRe$ is required, thus

the mass-flux calibration has to be properly planned. To determine the range of the calibration, the first thing to consider is that boundary layer measurements are involved. Therefore, the lower limit of the calibration must include at least the expected lower speed in the investigated boundary layer profile (closest point to the cavity endwall). Nevertheless, points with higher Reynolds numbers were acquired in order to build a more robust calibration. To accomplish this, the wind tunnel had to be operated in a variety of conditions by varying the rotational speed of the compressor as well as the vacuum level. Finally, the calibration matrix is presented in table 4.2.

Table 4.2: Mass-flux calibration matrix

Point #	Outlet		Inlet		
	Re_{out}, is	M_{out}, is	M_{in}, is	Re_w	Kn_w
1	30000	0.25	0.144	3.054	0.070
2	40000	0.35	0.225	4.473	0.075
3	50000	0.4	0.263	5.787	0.067
4	55000	0.45	0.296	6.405	0.068
5	60000	0.5	0.326	6.998	0.069
6	65000	0.6	0.376	7.495	0.074
7	67000	0.65	0.397	7.658	0.076
8	70000	0.7	0.415	7.923	0.077
9	70000	0.8	0.440	7.728	0.084
10	70000	0.9	0.454	7.513	0.089
11	80000	0.9	0.455	8.602	0.078
12	90000	0.9	0.456	9.691	0.069
13	100000	0.9	0.457	10.78	0.063
14	110000	0.9	0.457	11.87	0.057
15	120000	0.95	0.460	12.75	0.053

The mass-flux calibration is then carried out in the range of flow conditions specified by the test requirements. The data are plotted in the non-dimensional form Nu-Re, using the $T_{w,eff}$ in the computation of the Nusselt number. In this case, the flow is no longer considerable incompressible and equation 4.12 stands. The methodology developed by Cukurel [21] require an empirical correlation proposed by Dewey [39] in order to eliminate the Mach number dependency:

$$Nu_{\text{corr}}\left(Re_w, \inf\right) = \frac{Nu(Re_w, M)}{\phi(Re_w, M)} \tag{4.23}$$

where

$$\begin{aligned}\phi(Re_w, M) = 1 + A(M)\left[1.834 - 1.634\left(\frac{Re_w^{1.10}}{2.765 + Re_w^{1.104}}\right)\right] \\ \times\left[1 + \left(0.3 - \frac{0.0650}{M^{1.670}}\right)\left(\frac{Re_w}{4 + Re_w}\right)\right]\end{aligned} \tag{4.24}$$

and

$$A(M) = \frac{0.6039}{M}1 + 0.5701\left[\left(\frac{M^{1.222}}{1 + M^{1.222}}\right)^{1.659} - 1\right] \tag{4.25}$$

This correlation has been developed based on data from infinitely long wires and consists in the use of a correction term $\phi(Re_w, M)$ that relates the actual Nusselt number to the one if the flow is highly supersonic (Eq. 4.23 , that found to be Mach independent due to the *hypersonic freeze* phenomenon. The correlation is valid for $M > 0.3$ and for all the Reynolds numbers [39].

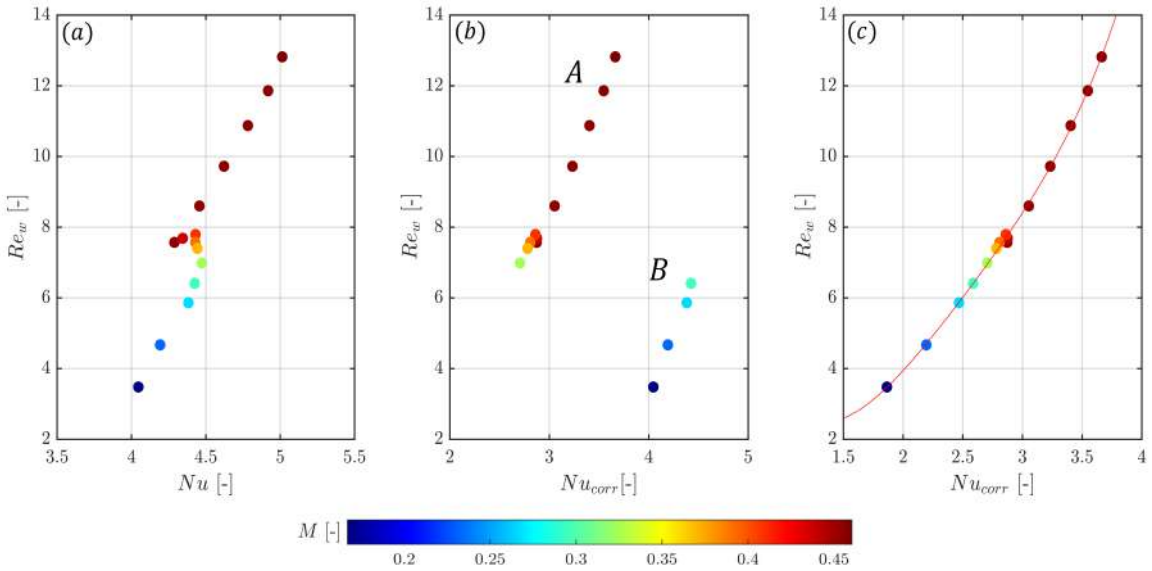

Figure 4.10: Mass-flux calibration results: (a) not corrected calibration data, (b) Application of Dewey's correction, (c) Final $Nu_{corr}Re_w$ single calibration curve.

The results of the calibration curve are presented in figure 4.10a. The compressibility effect is clearly visible in the scattered region of the curve around M = 0.4. When the correction is applied, a single $Nu_{corr} - Re$ calibration curve is retrieved.

In figure 4.10b the correction of Dewey is applied. Since this correlation is only valid for $M > 0.3$, two curves can be distinguished:

- Curve A: For $M > 0.3$, Dewey's correlation is applied.
- Curve B: $M < 0.3$, no correction applied, $Nu = Nu_{corr}$.

This behavior can create difficulties when measuring in Mach numbers around 0.3. For this reason, an extension to Dewey [39] correlation is proposed by Klopfer [44] to cover the range $0 < M < 0.4$, thus a single calibration curve can be obtained. The correlation is based on a weighted logarithmic average between the Oseen solution at $M = 0$ by Cole and Roshko [45] and the corrected Nusselt number at $M = 0.4$ by Dewey .

The corrected Nusselt number Nu_{corr} is given by:

$$Nu_{\text{corr}} = 10^{F\log(Nu(Re,0))+(1-F)\log(Nu_{\text{corr}}(Re,0.4))} \tag{4.26}$$

where

$$F = \left[0.618 + (2.5M)^{0.9}\right]^{-1} - 0.618 \tag{4.27}$$

and

$$Nu(Re, 0) = 0.19 + Re^{0.45} \tag{4.28}$$

This extension was validated using a set of experimental data ranging over $0.1 < Re < 300$. In figure 4.10c, the extended correlation is applied, creating a continuous Mach independent calibration curve for the whole Mach number range:

- For$M \geq 0.4$: Dewey's correlation
- For $M < 0.4$: Klopfer's extension

A previous employment of the aforementioned extension is reported by Boufidi [46] and Biondi [23].

4.3 Sensitivities method

In high subsonic and transonic flows, one method for quantifying the voltage dependency of the hot-wire signal is to assume a functional dependency of $Eb = f(\rho, u, T_0)$ for a given probe and wire temperature, and then empirically curve fit these variables using multiregressive methods. A technique more physical in nature is to determine the sensitivity to various nondimensional parameters [21].

Pioneering work on application of one-dimensional flow normal hot-wire methods for supersonic and transonic flows were conducted by Kovasznay [47] and Morkovin [48] respectively. Morkovin [48], related the fluctuations of the output voltage of the anemometer to the fluctuations of density, velocity and total temperature for Constant Current Anemometry (CCA), by assuming small perturbations. For Constant Temperature Anemometry (CTA) and straight wires mounted parallel to the flow, the following relationship stands:

$$\frac{{E_b}'}{\overline{E_b}} = S_\rho \frac{\rho'}{\bar{\rho}} + S_u \frac{u'}{\bar{u}} + S_{T_0} \frac{T_0'}{\overline{T_0}} \tag{4.29}$$

where S_ρ, S_u and S_{T_0} are the sensitivities to density, velocity and total temperature respectively, defined as follows:

$$S_\rho = \left(\frac{\partial \log E_b}{\partial \log \rho} \right)_{u, T_0 = const} \tag{4.30}$$

$$S_u = \left(\frac{\partial \log E_b}{\partial \log u} \right)_{\rho, T_0 = const} \tag{4.31}$$

$$S_{T_0} = \left(\frac{\partial \log E_b}{\partial \log T_0} \right)_{u, \rho = const} \tag{4.32}$$

The above-mentioned equations can be use to directly obtain the sensitivities through a systematic calibration, where one parameter is varied while keeping the others constant. Nevertheless,this method requires extensive, time-consuming calibrations in a closed-loop facility. In the present study, a non-dimensional calibration will be used to compute the sensitivities from their non-dimensional expressions:

$$S_\rho = \frac{1}{2} \left(\frac{\partial \log Nu}{\partial \log Re} - \frac{1}{\tau_{wr}} \frac{\partial \log \eta}{\partial \log Re} \right) \tag{4.33}$$

$$S_u = S_\rho + \frac{1}{2m} \left(\frac{\partial \log Nu}{\partial \log M} - \frac{1}{\tau_{wr}} \frac{\partial \log \eta}{\partial \log M} \right) \tag{4.34}$$

$$\begin{aligned} S_{T_0} = \frac{1}{2} \Big[n_t + 1 - m_t \frac{\partial \log Nu}{\partial \log Re} - \frac{\theta}{\theta - \eta} \\ + \frac{1}{\tau_w} \left(-\frac{1}{2m} \frac{\partial \log \eta}{\partial \log M} + m_t \frac{\partial \log \eta}{\partial \log Re} \right) - \frac{1}{2m} \frac{\partial \log Nu}{\partial \log M} \Big] \end{aligned} \tag{4.35}$$

where

$$n_t = \frac{\partial \log k}{\partial \log T_0}, m_t = \frac{\partial \log \mu}{\partial \log T_0}, m = \frac{1}{1 + M^2 \frac{\gamma - 1}{2}} \text{ and } \theta = \frac{T_w}{T_0}$$

In incompressible and supersonic flows the Mach number does not affect the heat transfer process ($Nu \neq f(M)$). This results in $S_u = S_\rho = S_{\rho u}$ and equation 4.29 can be simplified to:

$$\frac{E_b'}{\overline{E_b}} = S_{\rho u} \frac{\rho u'}{\overline{\rho u}} + S_{T_0} \frac{T_0'}{\overline{T_0}} \tag{4.36}$$

Since the focus of most prior literature was on obtaining time-averaged turbulent quantities rather than their instantaneous values, equation 4.36 is typically adapted to provide the mean-squared reduced sensitivity equation:

$$\frac{\overline{E_b'^2}}{\overline{E_b}^2} = S_{\rho u}^2 \frac{\overline{(\rho u)'^2}}{\overline{\rho u}^2} + S_{T_0}^2 \frac{\overline{T_0'^2}}{\overline{T_0}^2} + 2 S_{\rho u} S_{T_0} \frac{\overline{(\rho u)' T_0'}}{\overline{\rho u}\,\overline{T_0}} \tag{4.37}$$

This equation can be solved by a graphical method called “the fluctuation diagram technique” developed by Kovasznay [47], which involves varying the overheat ratio, assuming that the statistical properties of the flow do not change during the overheat variation.

In high subsonic and transonic flows, there is a strong Mach (or Knudsen) effect on the heat

transfer process, and $S_\rho \neq S_u$. In this case, equation 4.29 can only be solved instantaneously by using at least three wires with sufficiently different sensitivities (e.g. different overheats, materials or diameters) to solve a system with three equations and three unknowns. Although, in practice, this proved nearly impossible, because even minor errors in obtaining the sensitivities can cause an ill conditioning of the system's matrix [38]. Unsuccessful reported attempts are attributed to Rose et al [49] and Ikawa [50].

In literature, there are discrepancies regarding the behavior of the sensitivities. Horstman and Rose [51] found that for high overheat ratios ($\tau_w > 0.8$) and high Reynolds numbers ($Re_w > 20$), $S_u = S_\rho$. Nevertheless this was not supported by other studies [52], [53], where the sensitivity to density was always higher than the sensitivity to velocity. In summary, in order to obtain turbulence information from the measurements, most investigators had to assume the equality of velocity and density sensitivities.

In the most general case, the angular dependency should be also included. Motallebi [54] introduced the yaw angular sensitivity S_α for inclined wires in a planar flow field, expressed as:

$$S_\alpha = \frac{1}{2}\left(\frac{1}{\tau_{wr}}\frac{\partial \log \eta}{\partial \log \alpha} - \frac{\partial \log Nu}{\partial \log \alpha}\right) \tag{4.38}$$

The pitch angle sensitivity S_β for three or more inclined wires in a three dimensional flow field, should also be included:

$$S_\beta = \frac{1}{2}\left(\frac{1}{\tau_{wr}}\frac{\partial \log \eta}{\partial \log \beta} - \frac{\partial \log Nu}{\partial \log \beta}\right) \tag{4.39}$$

Finally, the sensitivity equation takes the following form:

$$\frac{E_b'}{\overline{E_b}} - S_\alpha \frac{\alpha'}{\bar{\alpha}} - S_\beta \frac{\beta'}{\bar{\beta}} = S_\rho \frac{\rho'}{\bar{\rho}} + S_u \frac{u'}{\bar{u}} + S_{T_0} \frac{T_0'}{\overline{T_0}} \tag{4.40}$$

The yaw and pitch angles are, usually, expressed with respect to the wire coordinates system. In the same way as equation 4.29, equation 4.40 can be solved instantaneously using a probe with at least five wires, in order to transform it in a system of five equations and five unknowns. In general, the added complexity due to the introduced angular dependency has encumbered accurate multidimensional measurements using conventional sensitivity analysis techniques, and results are reported to be inferior to that of a normal wire [54].

In the present study, adopting a single-wire probe, the equations available are not enough to decouple the velocity to density from the mass-flux time-series. Therefore, total temperature and density fluctuations have to be considered negligible.

4.4 Post-processing Methodology

The measurements where done upstream of the cascade at discrete points in the flow conditions described in chapter 3. During the first phase of the experimental campaign, regarding only the turbulence grid, each acquisition lasted 3s with a sampling frequency of 70 kHz. The second phase of the experimental campaign (with turbulence grid and wake generator) the sampling frequency was increased to 120 kHz.

Since a $Nu - Re$ calibration curve was chosen, an iterative cycle has to be built in order to obtain the Reynold's number time-series that corrects the Nusselt number, and allows to retrieved the velocity. The proposed data reduction methodology was built and implemented based on the reduction procedure developed by Boufidi [46] and Acarer [55].

Time-averaged measurements Given the total temperature, pressure measurements at the hot-wire's position, the following methodology concerning time-averaged measurements is used:

1. The mean Mach number is computed by Equation 3.9.
2. The Nusselt number is computed by Equation 4.14.
3. For the first iteration it is assumed that $Nu = Nu_{corr}$.
4. The value of Re_w is obtained by the calibration law.
5. A new value of Nu_{corr} is obtained by applying Dewey's and Klopfer's correlations (Eqs. 4.23 and 4.26)
6. A new value of Re_w is obtained through the calibration law.
7. Go back to point 5 until $Re_{w,new} = Re_w$.
8. The mass-flux can be computed by the Reynolds number definition Eq.4.13
9. With the mean density value computed by the pressure measurements, the velocity measured by the hot-wire can be obtained.

The above methodology is used for the computation of the mean velocity and characterization of the boundary layer. According to Cukurel [21], this methodology can be used for time-resolved measurements as well. The only difference is that the time-series of the Nusselt number is used instead of the mean value.

Time-resolved measurements Cukurel [21] claims that fluctuations in the Mach number are insignificant because a 5%change in the Mach number results in a 1% error in the mass-

flux time-series results. Nonetheless, other researchers, such as Boufidi [56], stated that for compressible flow, the fluctuation in the Mach number need to be taking into account. Therefore, for the computation of the time-resolved measurements, the above procedure is modified as follows:

1. For the first iteration it is assumed that $M_{mean} = M_{inst}$.
2. The Nusselt number is computed by Equation 4.14.
3. For the first iteration it is assumed that $Nu = Nu_{corr}$.
4. The value of Re_w is obtained by the calibration law.
5. A new value of Nu_{corr} is obtained by applying Dewey's and Klopfer's correlations (Eqs. 4.23 and 4.26)
6. A new value of Re_w is obtained through the calibration law.
7. Go back to point 5 until $Re_{w,new} = Re_w$.
8. The mass-flux can be computed by the Reynolds number definition Eq.4.13
9. With the mean density value computed by the pressure measurements, the velocity measured by the hot-wire can be obtained.
10. With the static temperature value given by equation 3.10, the new value of the Mach number $M_{inst,new}$ can be computed through Eq.3.11.
11. Go back to point 2 until $M_{inst,new} = M_{inst}$

As previously mentioned, by adopting a single wire probe, the density fluctuations cannot be taken into account.

This methodology was already used by Biondi[23] and Boufidi[5]. The former carried out its experiments in the same cascade and under the same flow conditions ($M_{out,is} = 0.9$ and $Re_{out,is} = 70000$) as the present study, but for a different hot-wire. The latter conducted an investigation under slightly different flow conditions ($M_{out,is} = 0.69$ and $Re_{out,is} = 85000$) in a different cascade. Moreover,the same turbulence generator grid was used in both cases, including the present one.

Biondi [23] and Boufidi [5] stated that both of the methodologies are in disagreement with Roach's predictions [30]. Boufidi [5] compared her results with the ones of Monaldi [35] and Paolucci [36], who originally conducted hot-wire measurements in the same facility. She noticed that her results were underestimating the values of turbulence intensity obtained by

Monaldi [35] and Paolucci [36] (shown in figure 3.6) even though the latter are in agreement with Roach's predictions. Nevertheless, Monaldi [35] and Paolucci [36] used a King's law calibration made for each density level (thus, Reynolds number).

The King's law is a power law that relates the anemometer output voltage E to the flow velocity U as:

$$E^2 = A + BU^n \tag{4.41}$$

where A, B and n are constants. A is equal to the squared voltage at zero flow E_0^2. Therefore, the turbulence intensity can be calculated as follows:

$$Tu = \sqrt{\overline{E}'^2} \frac{2\overline{E}}{n\left(\overline{E}^2 - \overline{E}_0^2\right)} \tag{4.42}$$

This methodology has the disadvantage of being overly dependent on E_0, which can influence the final value of turbulence intensity [56]. Furthermore, by calibrating the hot-wire for each density level, eventual temperature variations caused by the self-heating of the facility (which leads to density variations), are neglected.

Nevertheless, the King's law is feasible only for restricted and extremely simple scenarios where the flow is isothermal ($T = const.$) and incompressible ($\rho = const.$) and the wire forms a $0°$ angle with the flow direction (no angular dependency). Therefore, the King's law does not represent an accurate tool for hot-wire anemometry in turbomachinery applications where the flow is highly unsteady, generally compressible, and subject to temperature, pressure, and thus density variations.

There is no solid evidence that can determine which method is superior, as both results do not show a good correlation with Roach's predictions. Due to the possibility of being influenced by the probe, the hot-wire used in the previous campaign by Biondi [23] was changed to the one shown in figure 4.3. Therefore, for time-resolved measurements both Cukurel and Boufidi's proposals were compared with the new hot-wire and a third method was implemented.

The third method to be tested is the sensitivities method, where density and total temperature fluctuations are considered negligible. In order to compute the sensitivities, the set of equations 4.33 -4.35 are used. The logarithmic derivatives of the recovery factor to Re and $Mach$ ($\frac{\partial \log \eta}{\partial \log Re}, \frac{\partial \log \eta}{\partial \log M}$) can be analytically computed from the empirical correlation proposed by Dewey [4]. The logarithmic derivatives of Nusselt to Reynolds and Nusselt to Mach can be transformed to:

$$\frac{\partial \log Nu}{\partial \log Re} = \frac{Re}{\phi}\frac{\partial \phi}{\partial Re} + \frac{\partial \log Nu_{\text{corr}}}{\partial \log Re} \tag{4.43}$$

$$\frac{\partial \log Nu}{\partial \log M} = \frac{M}{\phi}\frac{\partial \phi}{\partial M} \tag{4.44}$$

where, the terms $\frac{\partial \phi}{\partial Re}$ and $\frac{\partial \phi}{\partial M}$ are the partial derivatives of the correction term $\phi(Re, M)$. The only term depending on the wire properties is $\frac{\partial \log Nu_{\text{corr}}}{\partial \log Re}$, which can be directly obtained by the calibration curve.

The flow field inside a turbomachine is characterized by its complex unsteadiness. The total unsteadiness can be considered as the contribution of both periodic and random components. The periodically unsteady flow is caused by the relative motion of rotor and stator rows. Therefore, in the second part of the campaign a wake generator was implemented in plane 01 between the cascade and the turbulence grid (figure 3.7) in order to simulate a moving blade row upstream of the cascade.

Since the flow is characterized by deterministic and stochastic unsteadiness, one of the challenges in this study is to extract the stochastic fluctuations from the signal in order to compute the turbulence quantities.

In the case of rotating blade rows, this decomposition is performed by the so-called phase-averaging or phase locked averaging (PLA), resulting in the phase-averaged flow field, which is periodic over one rotor revolution or over one blade passage (when the flow between different passages is considered periodic). This decomposition can be expressed as follows:

$$X = \widetilde{X} + X' \tag{4.45}$$

where X is the instantaneous signal, $\widetilde{X}$ is the periodic fluctuations and X' is the purely stochastic fluctuations.

The periodic fluctuations can then be subtracted by the instantaneous component to retrieve the stochastic fluctuations. This method results in the extraction of all deterministic components related to the Rotor Disk Frequency (RDF) or the Bar Passing Frequency (BPF). A study between the two is show in A.

The steps for the realization of a phased locked averaged (PLA) signal are presented in figure 4.11. Using the number of bars, the raw signal can be divided into rotor revolutions where T corresponds to the period of one rotor revolution. One rotor revolution is defined as the part of the signal containing N complete bar passages (N peaks), where N is the number of bars, in this case 96. Then an average is taken over the number of revolutions that occur during the test. In this way, a ”mean rotor revolution” known as PLA can be obtained.

Once the phase-locked average has been obtained and subtracted from the raw voltage, the aforementioned methods can be used to calculate the turbulence quantities.

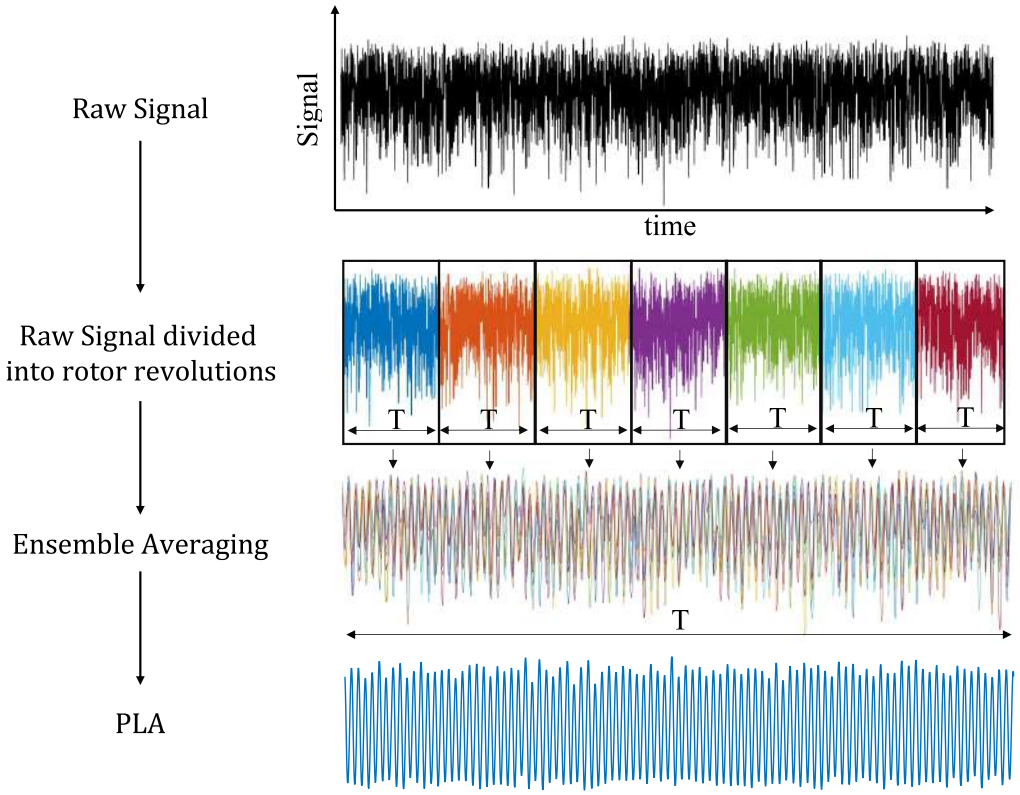

Figure 4.11: Steps from raw signal to PLA

Chapter 5

Results and discussions

In this chapter, time-average and time-resolved results are reported for nominal flow conditions described in section 3.2 for both phases of the experimental campaign. A study of the the inlet boundary layer and the mean velocity field of the flow is presented. As well the hot-wire sensitivities and turbulence quantities.

Hot-Wire Anemometry is a very effective tool in the characterisation of the boundary layer due to the small diameters of the wire. In the present study, the hot-wire was up to 1 mm from the wall in the first phase of the campaign and 0.5 mm in the second phase through a mechanical traversing system, capable of moving the probe both linearly and rotationally in the measuring plane. Despite the fact that the traversal system could go closer to the wall without touching it, a conservative approach is preferred in order to avoid damaging the wire. The traversing system's linear resolution is around 0.1 mm, and the smallest rotation possible is roughly 0.2 degrees.

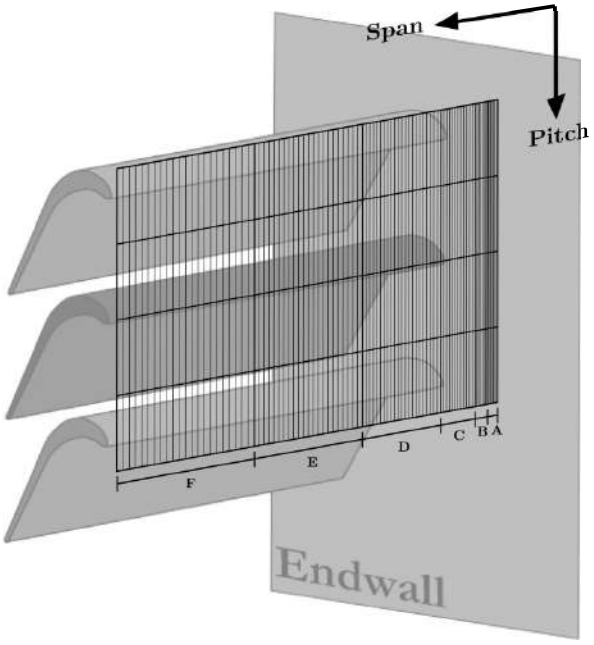

Figure 5.1: Illustration of the boundary layer measurement matrix

5.1 Time-Averaged velocity measurements

The characterisation of the Time-Averaged flow field at the cascade's inlet (plane 02) are presented in this section. The inlet boundary layer covers a role of paramount importance

in turbomachinery applications, therefore the measurements of the inlet boundary layer are given special attention. In addition the velocity 2D map at plane 02 is presented.

Due to the precise movement of the system and the reduced diameter of the hot-wire, the inlet boundary layer profile can be completely investigated. Acquiring a large number of points can be very time consuming. Therefore, in order to correctly analyze the boundary layer and at the same time reduce the testing time, a thinner mesh is used near the wall, where the velocity gradient is steeper, and gradually increases farther from the wall, approaching the free-stream.

The measurement matrix is shown in table 5.1 and represented in figure 5.1. The same spanwise traverse is repeated for five different pitch locations in order to capture the boundary layer's pitchwise evolution. For each pitch location 64 points were acquired, making a total of 320 points for the first phase of the campaign. The signal was acquired for 3 seconds at each measurement point with a sampling frequency of 70 kHz, leading to 350000 samples for each point. For the second phase the number of points close to the wall was increased making a total of 345 points, with a sampling frequency of 120 kHz, resulting in 3600000 samples for each point.

Table 5.1: Boundary layer mesh for each pitch position

Region	1^{st} Phase			2^{th} Phase		
	Span [%]	Step [mm]	n. Points	Span [%]	Step [mm]	n. Points
A	$0.6 \div 1.2$	0.1	10	$0.3 \div 1.2$	0.1	15
B	$1.2 \div 2.4$	0.2	10	$1.2 \div 2.4$	0.1	10
C	$2.4 \div 5$	0.5	10	$2.4 \div 5$	0.5	10
D	$5 \div 12$	1	10	$5 \div 12$	1	10
E	$12 \div 24$	2	10	$12 \div 24$	2	10
F	$24 \div 50$	3	14	$24 \div 50$	3	14
Total			64			69

5.1.1 Inlet Boundary Layer

The total pressure provided by the Pitot tube at the reference plane is no longer employable inside the boundary layer, since it refers to the free-stream. In order to compute the flow quantities inside the boundary layer, another source of total pressure must be considered. It is not possible to traverse a second probe at the same time as the hot-wire. However, due to the facility's high repeatability, the boundary layer could be measured in advance using a 5-Hole Pressure Probe (5HPP), and the resulting profiles were then inserted as an input to the hot-wire post-processing. As the dimensions of the 5HPP prevented it from covering the inner part of the boundary layer, the data in this region had to be extrapolated. To improve the extrapolation within the aforementioned region, a no-slip condition was applied to the wall, and linear interpolation was performed to connect the last acquired point and the no-slip point.

In figure 5.2 and 5.4 the results for the inlet boundary layer measurements are presented for

the cases without and with the wake generator, respectively. It can be seen in figure 5.2a that the data obtained by the hot-wire are close to those obtained by the 5HPP although there is a slight difference when the velocity profile approaches the maximum speed and the hot-wire overestimates the values in relation to the 5HPP. This difference is even more pronounced in the presence of the WG (figure 5.4a). Another significant difference is found in the inner part of the boundary layer. Where the hot-wire can reach a lower speed closer to the wall compared with the 5HPP. Since the hot-wire was actually traversed in the aforementioned region, it can be considered a more reliable source of information.

A boundary layer profile is expected to have zero velocity at the wall (no-slip boundary condition), and as it moves away from the wall, the flow velocity increases to a maximum and then approaches a constant speed. However, as can be seen in both figures 5.2 and 5.4 when approaching the free-stream flow region, the velocity reaches a peak and then gradually decreases rather than remaining constant.

An acceleration caused by the inlet lip is one possible explanation. The latter, also known as passive boundary layer control, is a curve contraction that allows the flow to transition smoothly from facility intake geometry to cascade inlet. Nevertheless, research on the boundary layer at plane 01 rules out this hypothesis [23]. Another explanation could be an instability phenomenon that changes the shape of the velocity profile. Ottavy [57] described different boundary layer shapes in a highly loaded compressor-like flat plane where he obtained similar profiles in the presence of a wake-passing unsteadiness.

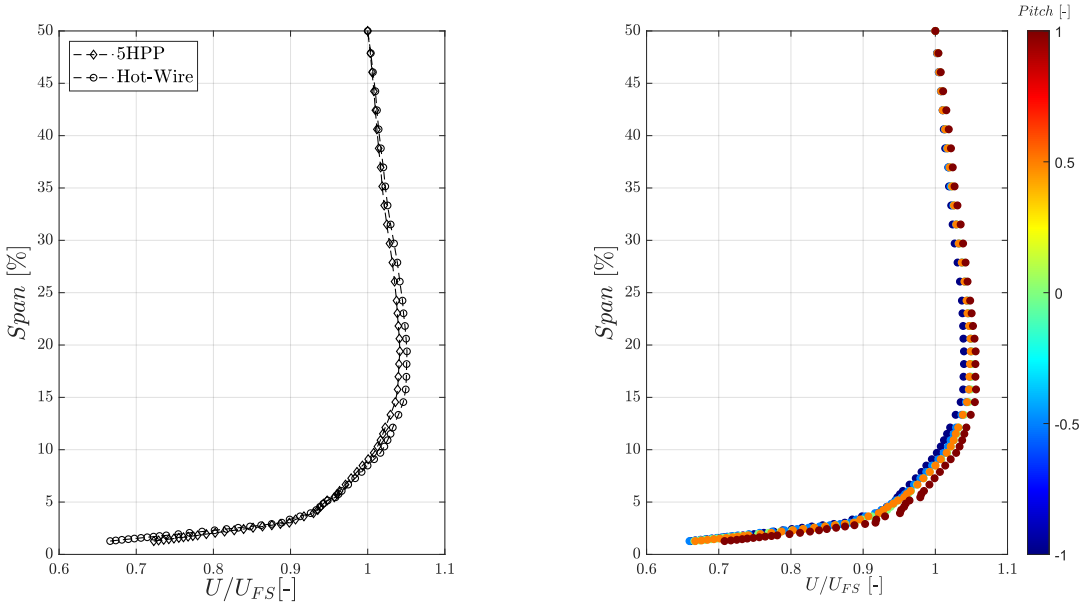

(a) (b)

Figure 5.2: Inlet boundary layer measurements with TG at nominal conditions - $M_{out,is} = 0.9$; $Re_{out,is} = 70000$. (a) Comparison between boundary layer measured by $Hot - Wire$ and $5HPP$. (b) Pitchwise evolution of the inlet boundary layer

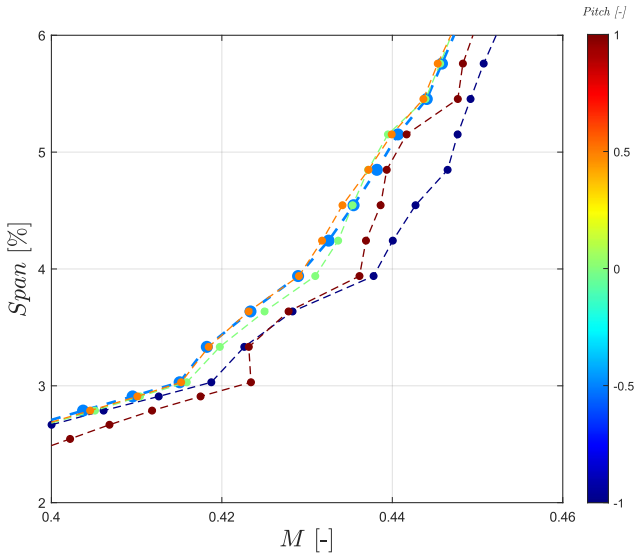

Figure 5.3: Detail of the boundary layer anomaly in terms of Mach number

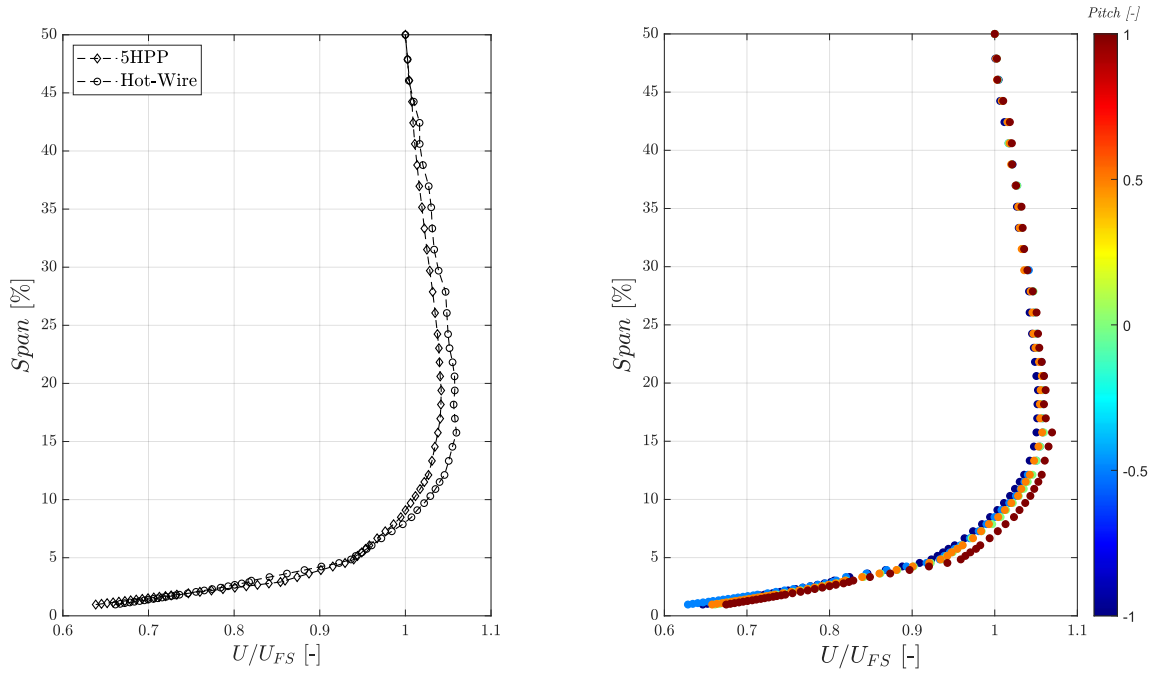

(a) (b)

Figure 5.4: Inlet boundary layer measurements with TG/WG at nominal conditions: $M_{out,is} = 0.9$; $Re_{out,is} = 70000$. (a) Comparison between boundary layer measured by $Hot - Wire$ and $5HPP$. (b) Pitchwise evolution of the inlet boundary layer.

Figure 5.2b and 5.4b shows the boundary layer profile at different pitch positions. As can be seen, in particular in figure 5.2b an anomaly occurs in the hot-wire profile and a more detail view is shown as a function of the Mach number in figure 5.3. The anomaly occurs between $M \sim 0.42 \div 0.45$, so this is not due to the transition between the two correction correlations around $M = 0.4$. This anomaly has already been detected by Biondi [23] so it is not related to the probe configuration.

When measuring close to the wall, the heat transfer going from the wire to the flow takes place as conduction rather than convection (figure 5.5a). This may result in inconsistent high velocities close to the wall, in general for $y > +5$ [8]. Depending on the thermal properties of the wall, different techniques exist in order to correct this effect. Since the facility works in adiabatic conditions, $T_{flow} = T_{wall}$ is assumed. The hot-wire voltage at several position down to the wall $E_{b,0}(y)$ is then retrieved with no flow, at the pressure level corresponding to nominal conditions ($P \simeq 8000Pa$). The wall-proximity voltage is then subtracted as it was an offset to the hot-wire voltage:

$$E^2_{b,\,\text{corr}} = E^2_b - [E_{b,0}(y) - E_{b,0}(y=0)] \tag{5.1}$$

As depicted in figure 5.5b, no deviations occur between corrected and not corrected velocities.This is most likely due to the polyamide's extremely low thermal conductivity ($k_{polyamide} = 0.24\,Wm^{-1}K^{-1}$).

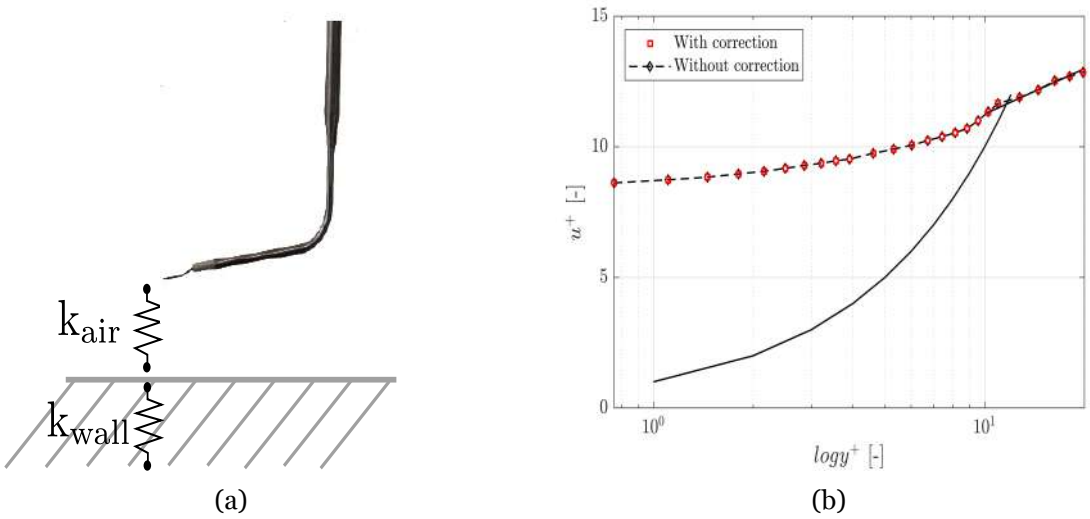

(a) (b)

Figure 5.5: Wall proximity hot-wire correction: (a) Schematic of the establishment of conduction with the wall [23], (b) Application of the correction to present study

In the present study a graphical empirical method, called *slope method* is adopted to compute the skin friction coefficient cf. Therefore the theoretical formulation of the cf (Eq. 2.25) can be rewritten as follow:

$$c_f = 2\left(\frac{B}{2.5U_\infty}\right)^2 \tag{5.2}$$

where B is the slope of the log layer plotted in $ln(y) - U$ coordinates.
The values of u^+ and y^+ are obtained by reformulating the equations 2.28 and 2.29 as a

function of cf:

$$u^+ = \frac{U}{U_\infty}\sqrt{\frac{2}{c_f}} \tag{5.3}$$

$$y^+ = \frac{yU_\infty}{v}\sqrt{\frac{c_f}{2}} \tag{5.4}$$

Figure 5.6 shows the boundary layer expressed in $u^+ - y^+$ coordinates. As it can be observed, in both cases, the 5HPP measurements are in fairly good agreement with the analytical expressions. However, the same does not happen with the measurements with the hot-wire, where the results differ from the analytical trend in the viscous sub-layer. Nonetheless, this could be due to the fact of having used extrapolated flow conditions derived artificially by the 5HPP measurements.

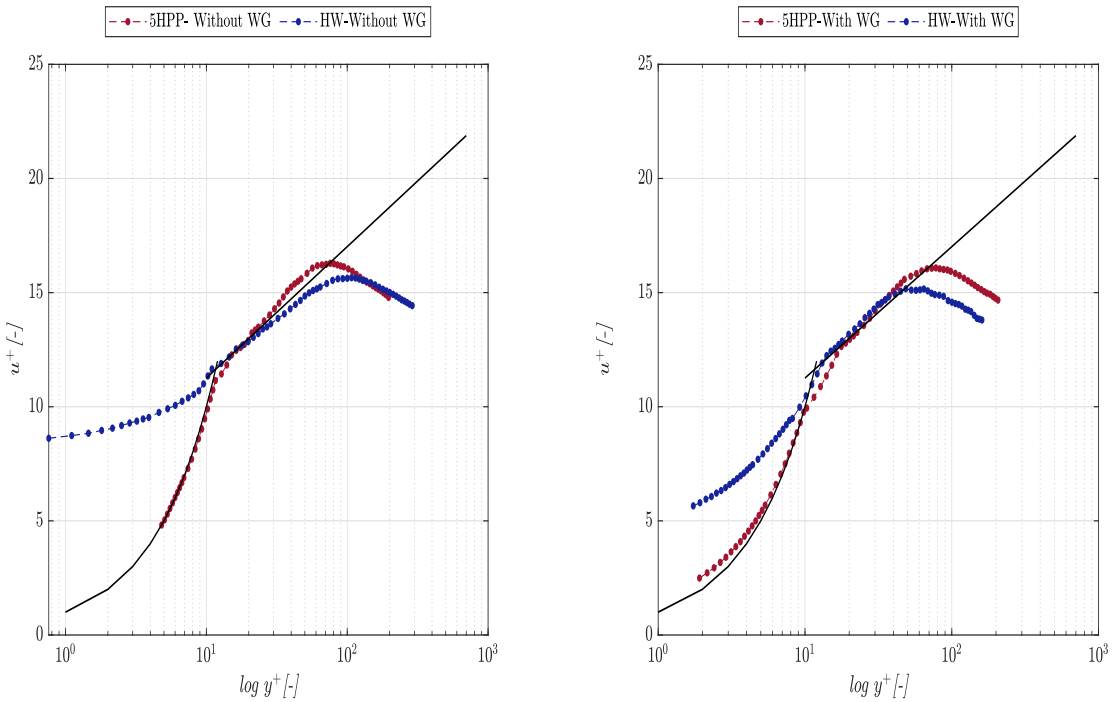

Figure 5.6: Comparison between hot-wire and 5HPP Boundary layer measurements expressed in terms of wall coordinates $y^+ - u^+$: (a) First phase of the experimental campaign, (b) Second phase of the experimental campaign

In Figure 5.7 the values of the boundary layer integral parameters for different pitch locations can be observed. Table 5.2 compiles the data from the figure 5.7 to provide a more rigorous interpretation of the results. As can be seen, there is greater coherence between the hot-wire and 5HPP values for the first phase of the campaign compared to the results of the second phase. Considering the hot-wire results it can be noticed a increased of the shape factor form

~ 1.4 to ~ 1.6 in the presence of the wake generator.According to Brunn [8], since this values are below 1.6 the flow can be considered as turbulent.

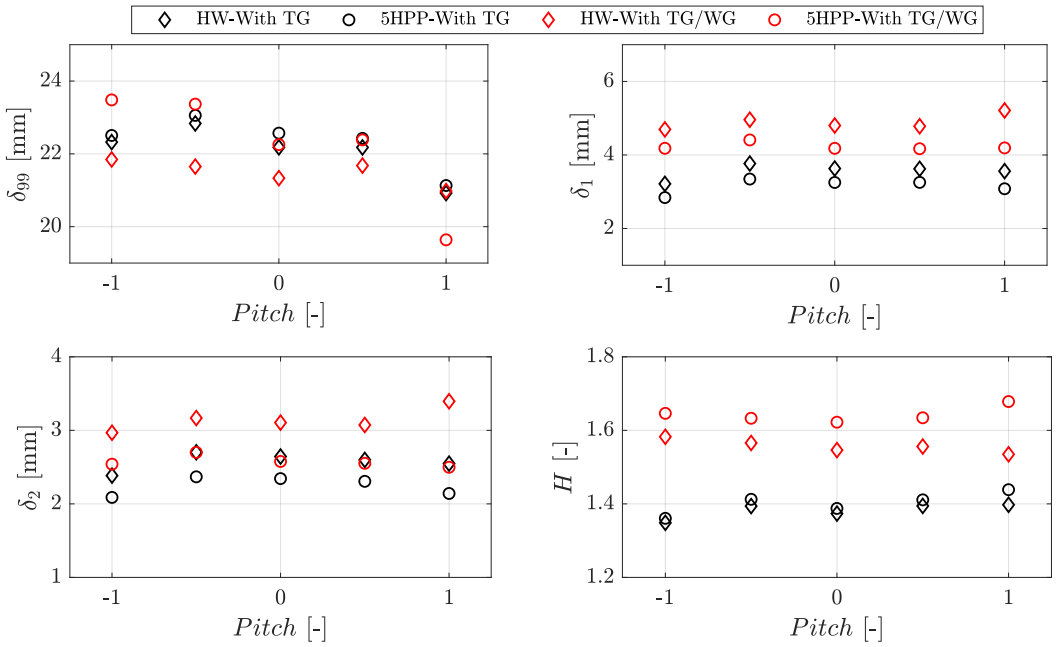

Figure 5.7: Boundary layer integral parameters

Table 5.2: Boundary layer integral parameters computed from the hot-wire (HW) and the five hole pressure probe (5HPP) for different pitch locations.

Pitch [-]		−1	−0.5	0	0.5	1
δ_{99} [mm]	HW - TG	22.324	22.836	22.179	22.177	20.923
	5HPP - TG	22.506	23.056	22.570	22.426	21.130
	HW - TG&WG	21.846	21.651	21.333	21.677	20.978
	5HPP - TG&WG	23.483	23.367	22.255	22.384	19.638
δ_1 [mm]	HW - TG	3.215	3.766	3.631	3.623	3.560
	5HPP - TG	2.841	3.345	3.252	3.254	3.081
	HW - TG&WG	4.696	4.959	4.801	4.781	5.211
	5HPP - TG&WG	4.181	4.409	4.180	4.170	4.192
δ_2 [mm]	HW - TG	2.384	2.702	2.644	2.598	2.547
	5HPP - TG	2.088	2.368	2.344	2.306	2.142
	HW - TG&WG	2.967	3.167	3.105	3.073	3.395
	5HPP - TG&WG	2.540	2.700	2.577	2.552	2.498
H [-]	HW - TG	1.349	1.394	1.374	1.394	1.397
	5HPP - TG	1.361	1.412	1.388	1.411	1.439
	HW - TG&WG	1.582	1.566	1.546	1.556	1.535
	5HPP - TG&WG	1.646	1.633	1.622	1.634	1.678

5.1.2 Inlet Plane 2D velocity mapping

A 2D mapping was carried out in order to provide a comprehensive description of the inlet cascade plane. Figure 5.8 shows the mean normalized velocity of the full inlet section. In the first phase of the campaign (without the wake generator) only five spanwise traverses were acquired without the sufficient amount of points to properly cover both span and pitch directions, resulting in a poor contour of the inlet section, as can be seen in figure 5.8a.

To correct this problem, in the second phase of the campaign, the measurement matrix in table 5.1 was modified to decrease the number of points in the spanwise direction and increase the number of pitch positions. The span was analysed from the wall until 10% span with a step of 1mm and then with a step of 5mm until midspan of the blade. This traverse was repeated for 23 pitchwise locations with a step of 3mm, making a total of 667 points. These amount of points result in a much more refine mesh that can thoroughly describe the inlet section.

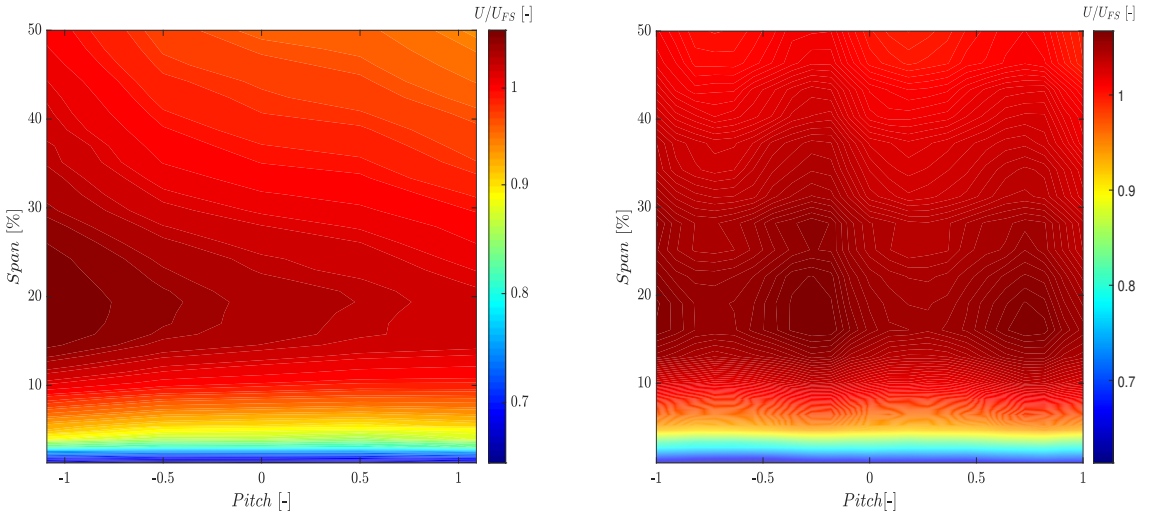

Figure 5.8: Inlet mean velocity 2D mapping: (a) Normalized mean velocity contour witht TG, (b) Normalized mean velocity contour with TG&WG

Figure 5.9 depicts the pitchwise mean velocity distribution for different spanwise locations. In figure 5.9a only two traverses were made at 10% and 50% of the blade span since the ones from the previous matrix do not provide enough points in the pitch direction to provide a proper analysis. Whereas in figure 5.9b thanks to the new matrix more traverses can be observed. As can be seen there is the same trend as the 2D map in figure 5.8b. The velocity tends to be more or less constant in the pitch direction and increases until $\sim$ 20% of the span then decreases until the wall.

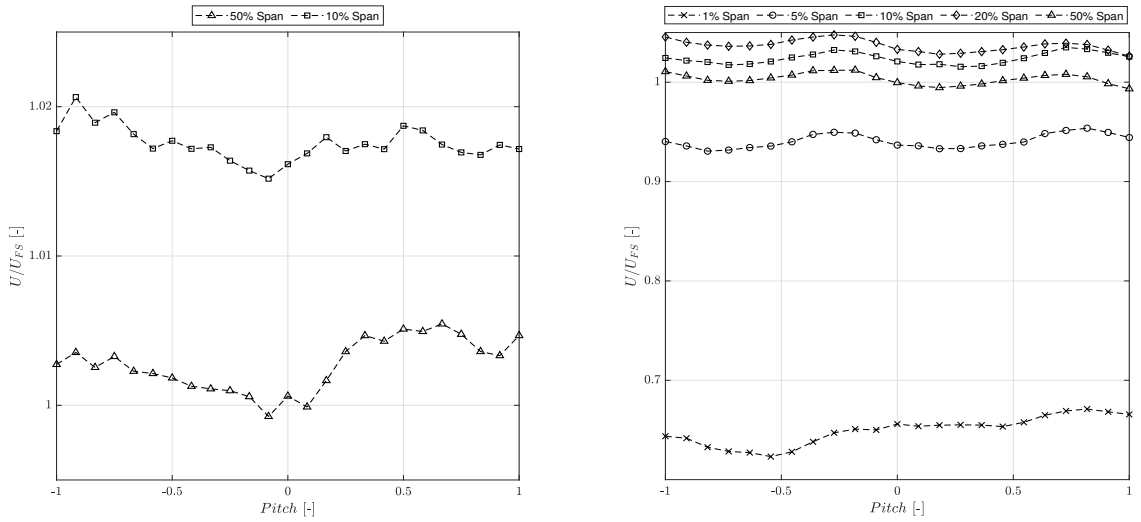

(a) (b)

Figure 5.9: Mean velocity distribution at different span locations: (a) Mean velocity distribution at 10% and 50% span for the first phase of the campaign, (b) Mean velocity distribution at 1%, 5%, 10%, 20% and 50% span for the second phase of the campaign

5.2 Time Resolved Measurements

As previously stated, hot-wire anemometry is the principal technique for measuring turbulence and, as a result, velocity fluctuations. To accomplish this, the hot-wire output voltage is no longer time-averaged, but rather measured over the entire time-series.

5.2.1 Selection of the methodology

For the sake of simplicity, the three methods that have been implemented for time-resolved measurements can be summarized as follows:

- **Method 1 - TA reduction**: it is the data reduction procedure for Time-Averaged quantities but taking the time-series of the Nusselt number instead of the mean value.
- **Method 2 - TR reduction**: it is the data reduction procedure for Time-Resolved measurements proposed by Boufidi [56].
- **Method 3 - Sensitivities**: it is the data reduction procedure using the sensitivities equations 4.33 -4.35 .

The results of the three methods are depicted in the figure 5.10 for a single traverse at midspan of the cascade. It was possible to verify that using *method 2*, the mach number obtained by the hot-wire was significantly overestimated when compared to the one obtained by the 5HPP, whereas the mach values obtained by *method 1* were in reasonable agreement. However, when evaluating turbulence, it was possible to see that *method 1* underestimates the

turbulence values predicted by Roach and *method 2* yields comparable results.

Boufidi [56] found reasonable results in her investigation in S-1/C, with the same inlet Reynolds number ($Re_{in,is} = 45000$) and a slightly lower Mach number ($M_{in,is} = 0.32$), therefore, no major differences were expected in the present investigation. However, from the results of figure 5.10 and the ones of Biondi [56] it is possible to conclude that both method 1 and 2 failed to fulfill the desired conditions. The need for an iterative cycle arises from the application of the compressibility corrections of Dewey and Klopfer to achieve the desired turbulence. As a result, it is reasonable to attribute the malfunctioning of the reduction technique to those functions. Specifically to the Dewey correlection since in the present study, contrary to what happened with Boufidi, the Klopfer correlation cannot be implemented, as it is only valid up to $M = 0.4$. It is evident that a deeply mathematical analysis would be required to further investigate the validity of the data reduction procedure for time-resolved measurements.

To address this issue, the third method is then used. The sensitivities can be calculated using the 4.33 - 4.35 equations and the calibration curve. The fluctuations to density and temperature are considered negligible, therefore the turbulence can be computed as:

$$Tu = \frac{1}{Su}\frac{E_b'}{\overline{E_b}} \tag{5.5}$$

This method shows good results in relation to the Roach correlation, as can be seen in figure 5.10b. Furthermore, the lack of an iterative cycle in the mach number makes this method much less time consuming. For these reasons this method will be used for the treatment of the time-series measurements.

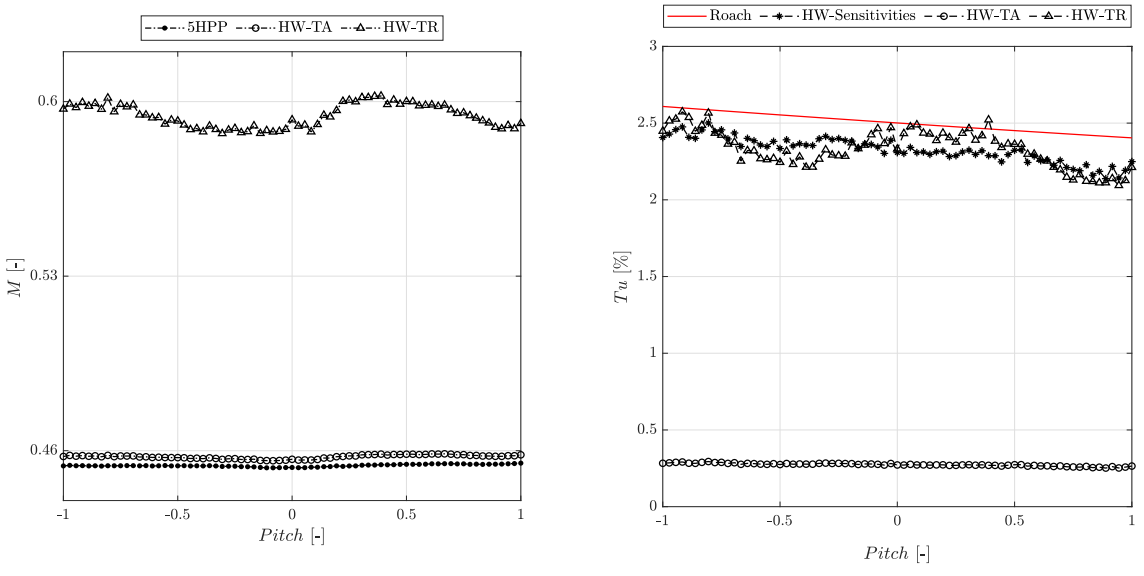

(a) (b)

Figure 5.10: Comparison between the different methodologies for time-resolved measurements: (a) Mach number comparison, (b) Turbulence intensity comparison

5.2.2 Hot-Wire Sensitivities

Boufidi [46] used the sensitivities approach to investigated several flow conditions by means Hot-Wire Anemometry. She found that in high-speed slip-flows ($Kn > 0.01$) the sensitivity to density and total temperature are greater than the sensitivity to velocity. Therefore, even if the level of fluctuations is low, the terms can be significant and neglecting them can lead to errors.

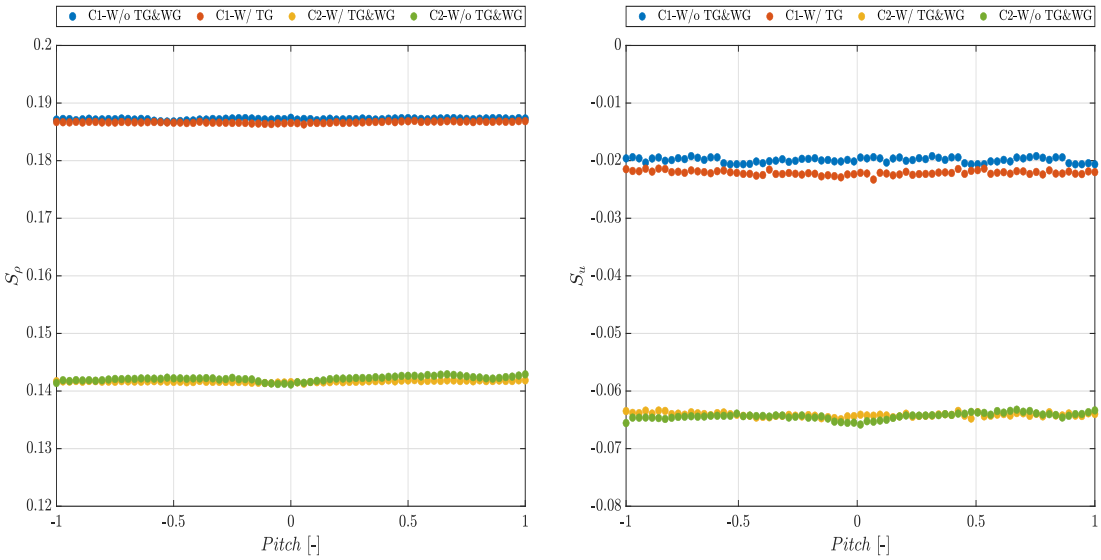

(a) (b)

Figure 5.11: Hot-wire sensitivities to density and velocity at midspan for both phases of the campaign: (a) Hot-wire sensitivity to density, (b) Hot-wire sensitivity to velocity

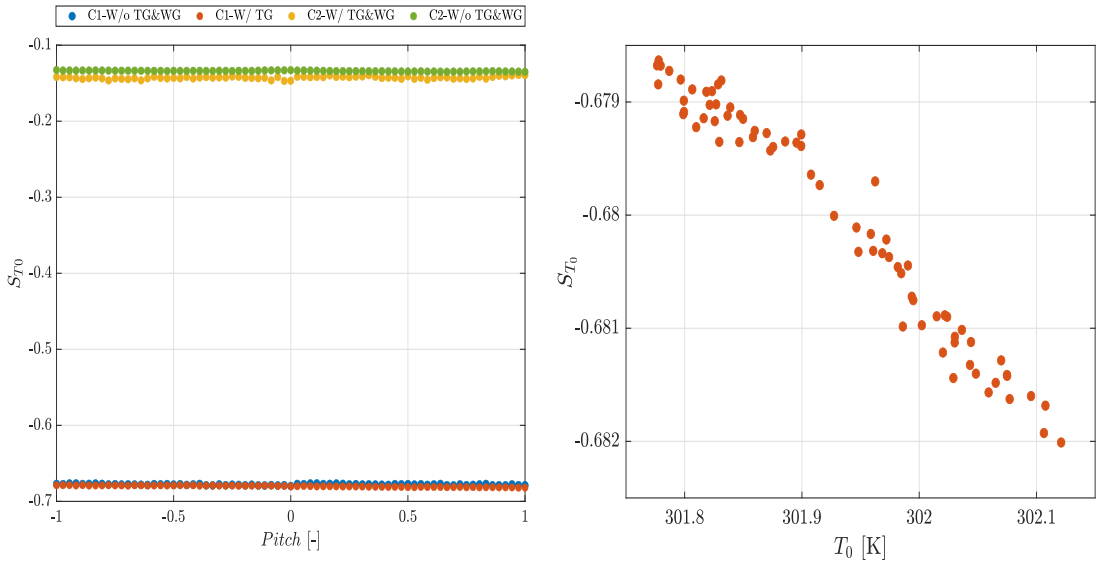

(a) (b)

Figure 5.12: Hot-wire sensitivity to total temperature at midspan for both phases of the campaign: (a) Hot-wire sensitivity to velocity, (b) Sensitivity to total temperature

Table 5.3: Hot-wire sensitivities at midspan for both phases of the campaign

Sensitivity	1^{st} Phase Campaign		2^{nd} Phase Campaign	
	W/o TG	W/ TG	W/o TG&WG	W/ TG&WG
S_ρ	0.1874	0.1865	0.1411	0.1415
S_u	-0.0201	-0.0224	-0.0655	-0.0644
S_{T0}	-0.6798	-0.6803	-0.1329	-0.1468

Figures 5.11a, 5.11b and 5.12a show the sensitivities results to density, velocity and total temperature at midspan of the cascade, respectively. As can be seen, the sensitivities to density and total temperature are way higher than the sensitivities to velocity, supporting Boufidi's statements.

The sensitivity of the hot-wire to total temperature is negative, as an increase of the flow temperature decreases the temperature difference, resulting in a decrease of the heat transfer rate. This is consistent with the relevant literature, which states that the sensitivity to total temperature decreases as overheat increases. Since the wire temperature is constant, a decrease in flow temperature implies an increase in the overheat, according to equation 4.10. This can be observed in figure 5.12b, where the wire sensitivity to total temperature is plotted against the total temperature of the flow for each measurement point. The sensitivity is strongly influenced by the flow total temperature, which decreases with increasing temperature of the flow.

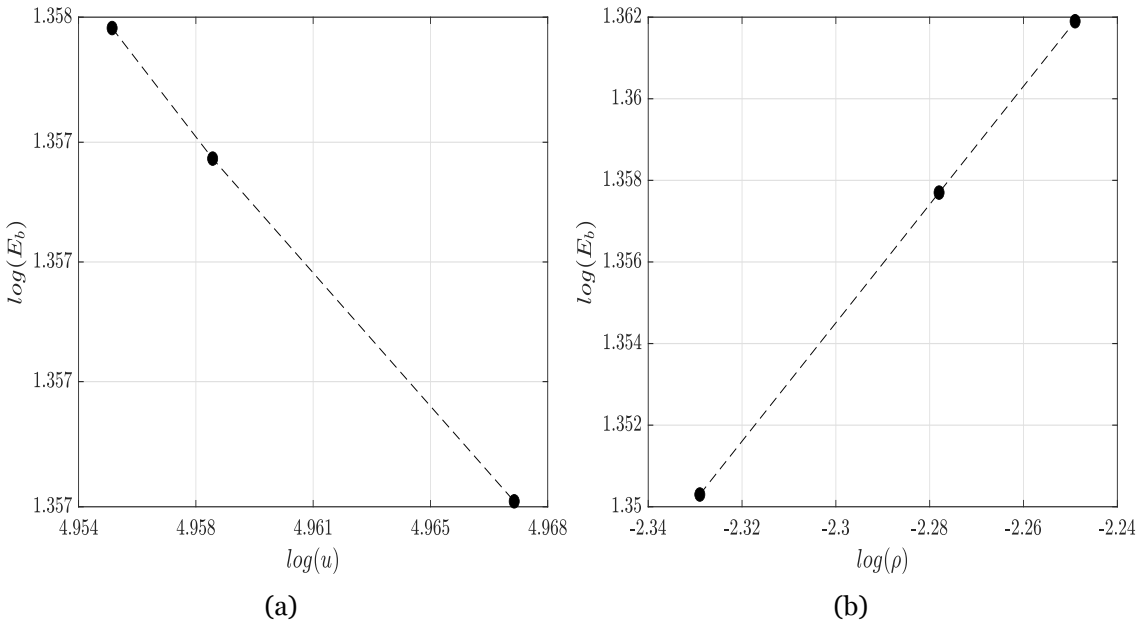

Figure 5.13: Experimental points for computation of hot-wire sensitivities: (a) Measurement points for sensitivity to velocity, (b) Measurement points for sensitivity to density

Besides of the negative sensitivity to total temperature also a negative sensitivity to velocity was measured (figure 4.34). To the author knowledge, this is not in agreement with any previous literature. In order to investigate this result some experimental points were taken

Table 5.4: Flow conditions of the experimental points

Point #	Sensitivity to velocity		Sensitivity to density	
	$M_{out,is}$	$Re_{out,is}$	$M_{out,is}$	$Re_{out,is}$
1	0.88	70000	0.9	68000
2	0.9	70000	0.9	70000
3	0.92	70000	0.9	72000
	S_u=-0.0749		S_ρ=0.1441	

in the second phase of the campaign. Using equations 4.31 - 4.32, the sensitivities can be obtained directly by varying one parameter while keeping the others constant. The results are show in figure 5.13. It can be noticed that with the increasing of the velocity the bridge voltage decreases, therefore the heat transfer decreases and as a result a negative value of for the sensitivity to velocity is obtained. A value of $S_u = -0.0749$ was obtained what is in agreement with the experiments with the wake generator. The same procedure was replicated to compute the sensitivity to density and a value of $S_\rho = 0.1441$ was retrieved.

Although the probe was the same in both phases of the campaign the wire needed to be replaced. This leads to a different characteristics of the wire, specially the effective temperature, witch has a big influence in the computation of the sensitivities. Boufidi [46] stated that by varying the temperature of the wire, very different sensitivities can be achieved. Therefore the sensitives in the first phase of the campaign with and without the turbulence grid are similar but slightly difference from the ones in the second phase with both turbulence generators.

5.2.3 Turbulence Intensity

Figure 5.14 show the turbulence intensity results for a pitchwise traverse at midspan of the cascade for the cases without turbulence grid nor wake generator, with turbulence grid and with both turbulence grid and wake generator. The turbulence intensity naturally achieved by the facility is around 0.8% what is in agreement with previous investigations conducted in S-1/C by Michàlek et al [32]. Also the turbulence intensity with the turbulence grid is in good agreement with Roach correlation. A turbulence of 2.4% was found at midspan and at 400mm far from the turbulence grid, as already mentioned in section 3.2 according to Roach at this position the turbulence should be 2.5% therefore a difference of 0.1% can be obtained. The value of the turbulence intensity with both turbulence generators increases $\sim 1.6\%$ compared to the value with the turbulence grid and increases $\sim 3.1\%$ compared to the value of the free-stream. To the author knowledge no comparison between the values of turbulence with passive and active generators was made in similar flow conditions. Some autors like Wolff et al [58] and Ladwig et al [59], study in slightly different flows conditions the turbulence intensity with and without a active turbulence generator, and a difference between 3% - 4% can be found to the results of the free-stream and with a active turbulence generator.

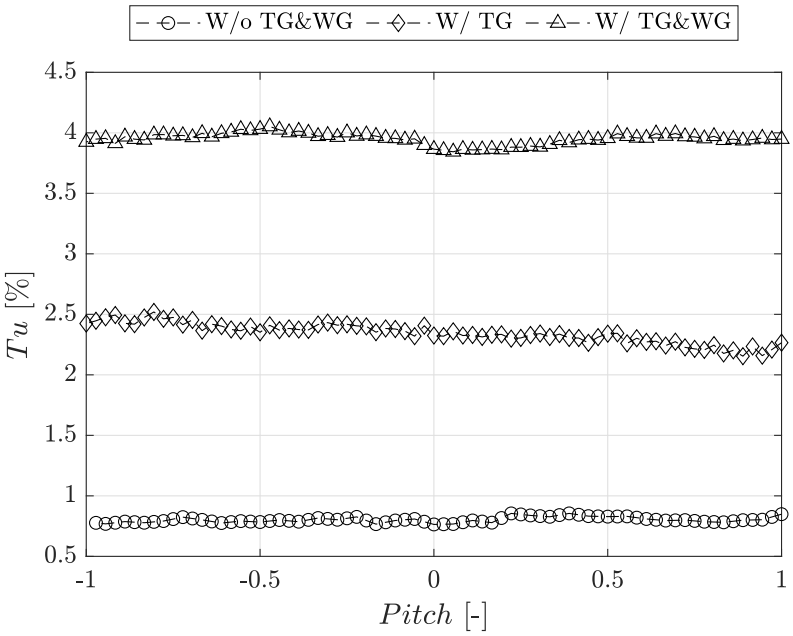

Figure 5.14: Turbulence intensity at midspan

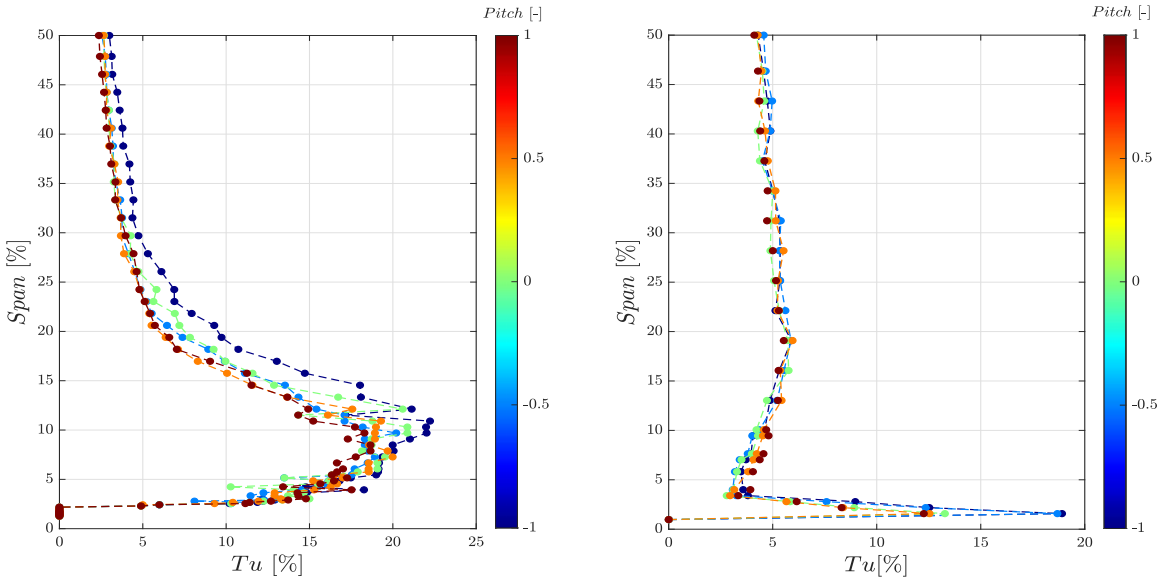

(a) (b)

Figure 5.15: Turbulence boundary layer: (a) Turbulence boundary layer for the first phase of the campaign, (b) Turbulence boundary layer for the second phase of the campaign

In figure 5.15 the results of the turbulence intensity for the boundary layer are show. Comparing both boundary layers it can be observed that the profile with only the tubulence grid (figure 5.15a) starts to increase gradualy from midspan until a maximun of $\sim 18\% - 22\%$ at $\sim 10\%$ span and then start to decrease until zero in the wall. Whereas the the turbulence with the wake generator (figure 5.15b) is more or less constante until $\sim 4\%$ of the span where it increases to a maximum and then drops to zero in the wall. To better visualize these results

the 2D turbulence map is presented in figure 5.16.

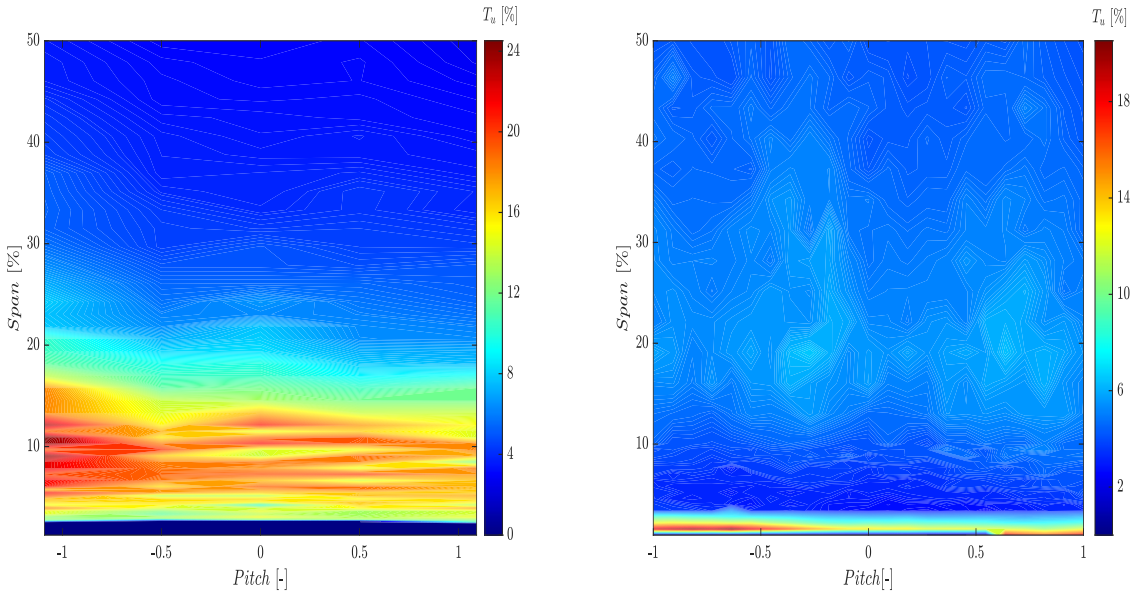

(a) (b)

Figure 5.16: Inlet Turbulence 2D mapping: (a) Turbulence intensity contour for the first phase of the campaign, (b) Turbulence intensity contour for the second phase of the campaign

5.3 Integral Length Scales (ILS)

As previously stated in section 2.1.2, the ILS are representative of the most energized eddies in the turbulence energy spectra. According to the energy cascade theory, these are the structures lying at the limit of the the integral and inertial ranges.

Two methodologies are taken into account and compared in the current investigation. When a large time series is available, as in this case, the autocorrelation function (ACF) is the most commonly used method in the literature to predict the integral length scales. Roach's approach, on the other hand, has been widely validated [60] and represents a reliable method.

The autocorrelation function shape strongly depends on the frequency spectrum of the signal. Since experimentally obtained autocorrelation coefficients may feature wide and frequent oscillations around zero, the integration for the complete signal duration can produce incorrect results. Therefore, different approaches have been proposed for the upper integration limit of equation 2.17. An option would be integrate the autocorrelation function up to the first zero crossing, nevertheless this approach is not efficient when high oscillations occurs [23]. Another option, which was used in this study, is to fit the experimental autocorrelation function with a Gaussian function and integrate the resulting function up to a certain tolerance. The input signal was low pass filtered with an 8 kHz cutoff frequency to remove undesirable oscillation on the ACF, which could lead to errors.

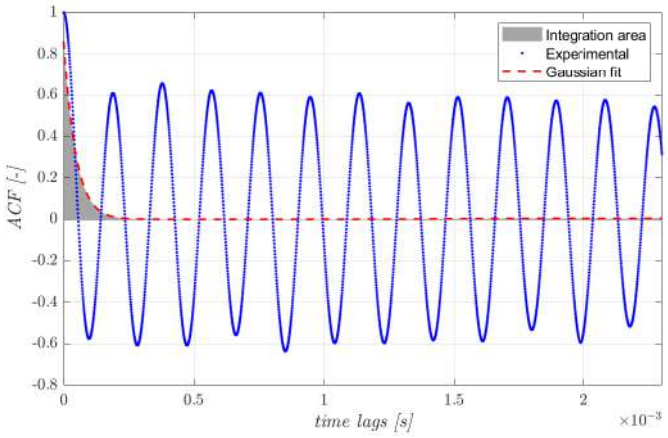

Figure 5.17: Time-autocorrelation dominated by the BPF

In the presence of the wake generator, the signal autocorrelation is dominated by the rotor disk frequency, as demonstrated in figure 5.17. Therefore, in this case, the ACF should be applied to the stochastic fluctuations of the signal. The methodology is the following:

- With the PLA, the signal is divided in rotor revolutions and the mean PLA velocity is computed.
- The mean PLA velocity is subtracted from the instantaneous velocity obtaining the stochastic fluctuations for each revolution, as depicted in Fig. 5.18.
- The integral time scale is then computed by the ACF of the signal of each revolution.
- The mean integral time scale is computed and then the integral length scale is retrieved applying Taylor's Frozen rotor hypothesis (equation 2.1.3).

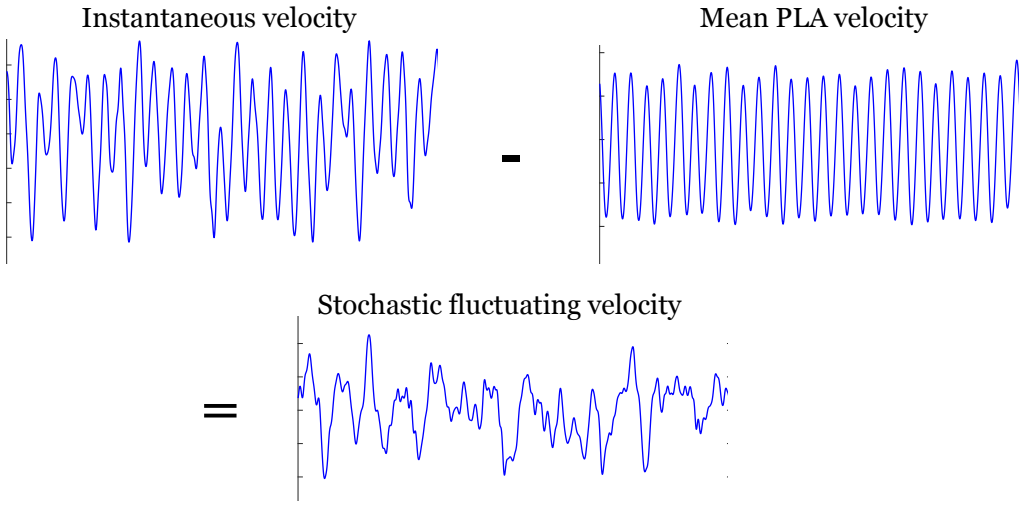

Figure 5.18: Decomposition of stochastic fluctuations

Roach's approach [30] is based on the assumption of truly isotropic turbulence, and his methodology consists in performing a Fourier transformation and compute the integral length

scales directly from the Power Spectral Density function (PSD) (see equation 2.1.3).

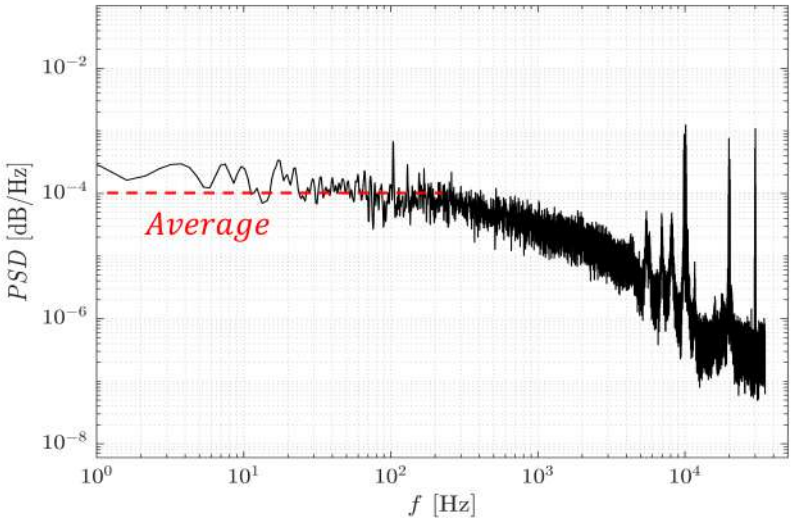

Figure 5.19: Averaging of the asymptotic spectra at $E(f)|_{f\to 0}$

The spectral energy $E(f)$ is extrapolated to zero frequency (figure 5.19), which is the averaged spectra up to when the energy reaches its asymptotic value. Roach also developed a correlation for estimating the Integral Length Scales downstream of Turbulence grid [30]:

$$\frac{\Lambda_x}{d} = I\left(\frac{x}{d}\right)^{1/2} \tag{5.6}$$

where $I = 0.2$, d is the diameter of the bar and x is the downstream distance from the turbulence grid. According to the employed turbulence grid, the predicted integral length scales resulted to be $\Lambda_x = 6.93mm$.

Figure 5.20a shows the integral length scales over a pitchwise traverse conducted at midspan and at nominal conditions, with the turbulence grid. It is clear that the two methods return very different results. While the spectra method give results close to the mesh size of the turbulence grid the ACF gave results close to the bar diameter. Such a big difference between the two method was alreday reporded by Biondi [23], who performed his experiments in the same facility under the same conditions.

The ILS without the turbulence grid are reported in figure 5.20b. As expected, the ILS are lower, as well as the difference between the two methods. Table 5.5 summarize the pitch-averaged values of ILS relative to the different cases.

Michalek et al [32] who previously conducted investigations in the S-1/C facility, computed the Integral length scales by using the ACF for a flow at $Re_{out,is} = 120000$. With the same turbulence grid he found a ILS of $12mm$, whereas without grid the ILS resulted to be $4mm$, which are in fare agreement with the present results from the spectra method. On the other hand, the results show a considerable difference with the ones computed by Biondi [23].

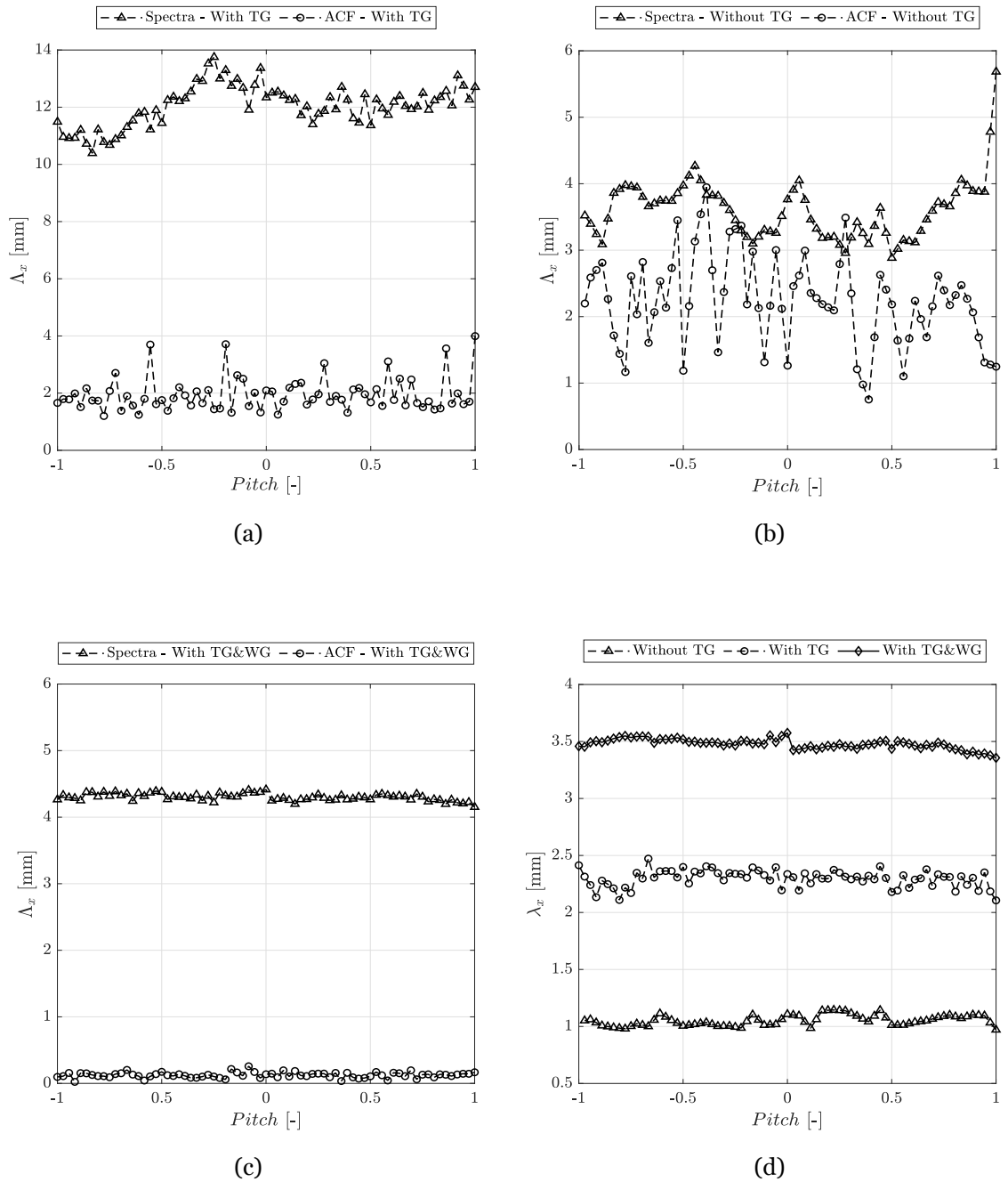

Figure 5.20: Length Scales: (a) ILS with TG, (b) ILS without TG, (c) ILS with TG&WG, (d) Dissipation Length Scales for the three cases

In Figure 5.20c the ILS for the case with both turbulence generators are show. The same trend between the two methods can be observed. Besides that, it is possible to notice that these values are smaller when compared with the case with only the turbulence grid.

Figure 5.20d despites the Kolmogorov scales for the three cases. The values for with and without the turbulence grid are in good agreement with the ones proposed by the spectra

method. On the other hand, with the wake generator the difference between the integral length scales from the spectra method and the Kolmogorov scales is very small. This could be related to the proximity of the wire to the wake generator.

Table 5.5: ILS at midspan of the central blade

Method	Λ_x[mm]		
	With TG	Without TG	With TG\WG
ACF	2.1	1.2	0.1
Energy spectra	12.2	3.9	4.4
Biondi[23]: ACF	3.2	0.7	-
Biondi[23]: Energy Spectra	20.1	2.4	-
Michalek [32]	12	4	-

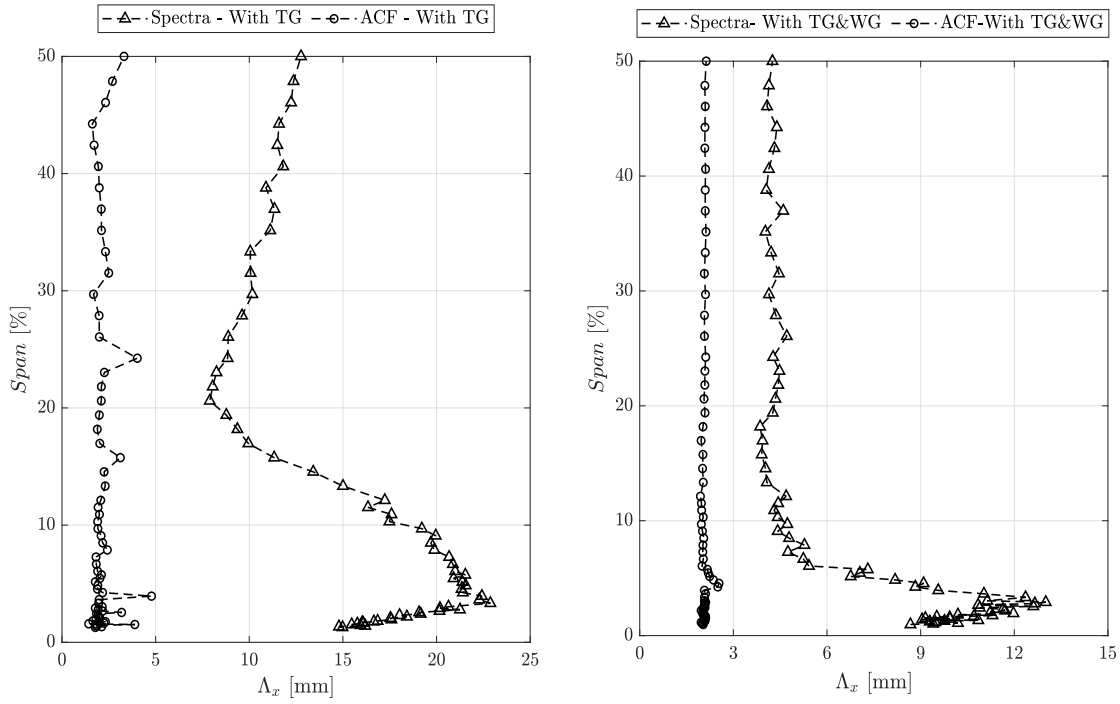

(a) (b)

Figure 5.21: Integral Length Scales for boundary layer at midspan: (a) ILS for the first phase of the campaign, (b) ILS for the second phase of the campaign

Figure 5.21a shows the ILS computed over a boundary layer traverse. It is worth noting that the methodology based on energy spectra is similar to the boundary layer profile, whereas those calculated using the ACF have approximately constant values through the span. In order to visualize the inlet boundary layer the $2D$ mapping of the integral length scales computed with the spectra method is show in figure 5.22.

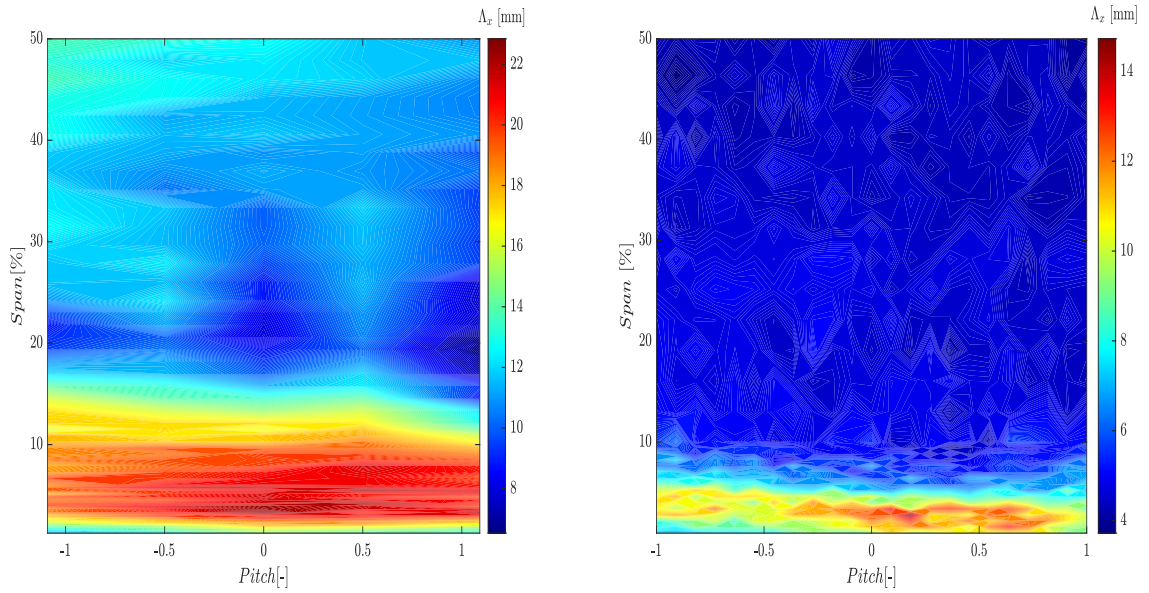

(a) (b)

Figure 5.22: Integral Length Scales 2D mapping computed with the spectra method: (a) ILS contour for the first phase of the campaign, (b) ILS contour for the second phase of the campaign

5.4 Power Spectral Density Analysis

In order to obtain additional information on the flow field, the Power Spectral Density (PSD) of the velocity fluctuations are evaluated. Spectral analyses are used to provide information about how the energy of the signal is distributed with respect to the frequency. The calculation of the spectra is mostly based on the Fourier Transform that produces values of discrete frequencies within sub-records of the signal [5]. In other words, taking the Fourier Transform of a correlation function leads to frequency-domain representation in terms of the spectral density function. For turbulent signals, the PSD represents the turbulent spectra addressed by the energy cascade. The signal is digitally reconstructed through a sampling frequency, that defines the maximum number of frequencies with which the signal may be represented in the Fourier domain. According to *Nyquist's theorem* [61], for a periodic signal with frequency f_p, the sampling frequency must be at least twice that frequency, $f_s = 2f_p$.

Figure 5.23 shows the Power Spectral Density of the velocity signal acquired at midspan with the turbulence grid. The spectra features the presence of several distinctive peaks, the main ones, depicted in detail, corresponds to 5.5 kHz, 7 kHz, 8 kHz, 10 kHz, 20 kHz and 30 kHz. Moreover, the $-5/3$ slope characteristic of the inertial sub-range is visible in a small region within 2 kHz and 4 kHz. Figure 5.24 depicts the spectra for the closest and furthest points to the turbulence grid throughout the pitchwise traverse. As expected, the furthest point features a slightly weaker PSD, relative to the turbulence decay induced by the turbulence grid.

In order to have a first idea of the origin of the aforementioned peaks, the PSD of the velocity

in the boundary layer is presented in figure 5.25 It can be noticed how the turbulence increased inside the boundary layer, which is in agreement with the evidences in figure 5.15a. Moreover, it is clear how turbulence first increases with distance from the wall and then decreases once outside the boundary layer.

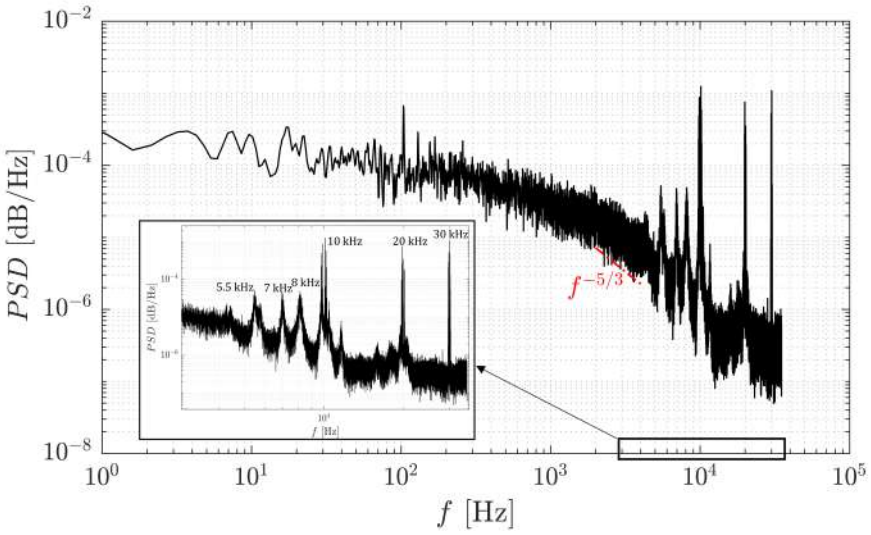

Figure 5.23: Power Spectral Density of the velocity signal at midspan under nominal flow conditions for the first phase of the campaign

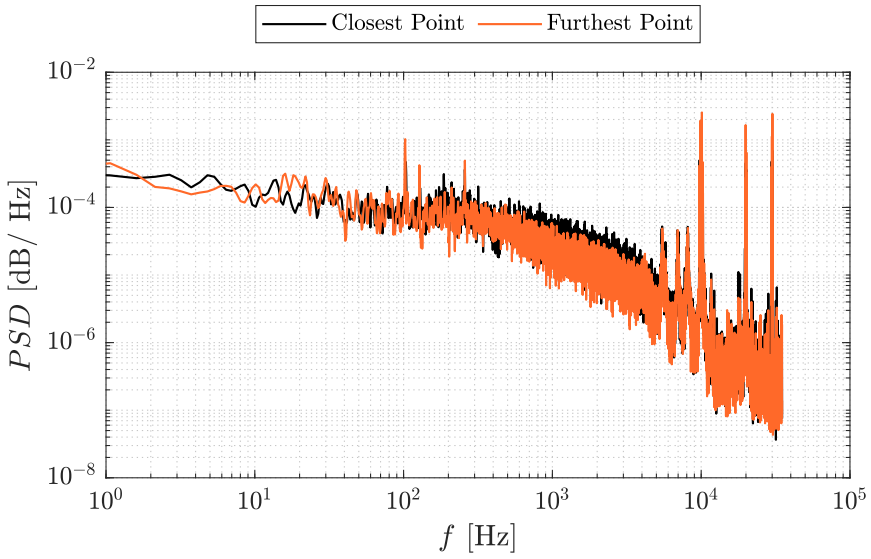

Figure 5.24: Power Spectral Density relative to closest and furthest points to the turbulence generator for the first phase of the campaign

If the peaks are examined in detail, it appears that the the 5.5 kHz peak increases by going close to the endwall and the remaining peaks exhibit the opposite trend. The 10 kHz could be related to the turbulence grid vortex shedding. If a Strouhal number ($St = fL/U$) of $St = 0.21$, characteristic of the vortex shedding frequency, the diameter of the turbulence grid bars and the inlet mean flow velocity are considered, a frequency of 10.8 kHz is ob-

tained. Nonetheless, as will be demonstrated later, the 10 kHz peak persists in the absence of turbulence grid.

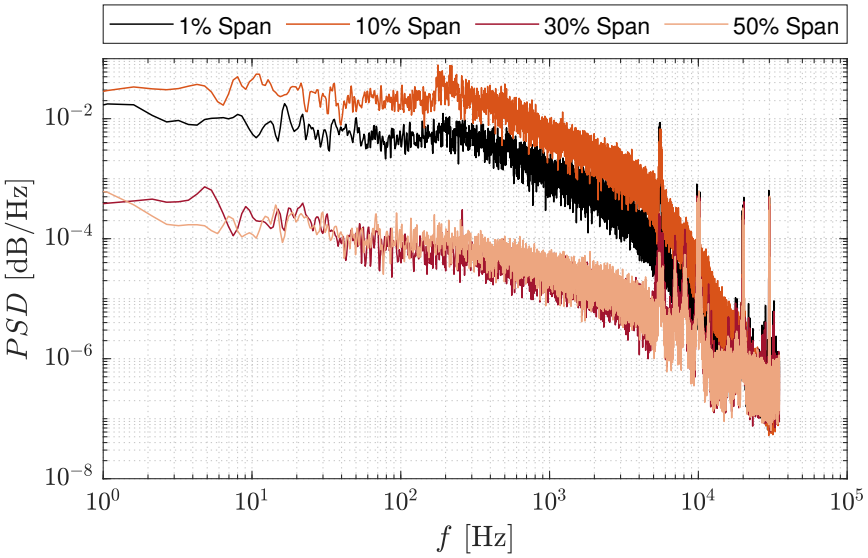

Figure 5.25: Power Spectral Density of the Velocity in the Boundary Layer for the first phase of the campaign

Figure 5.26 depicts the PSD at midspan with and without grid, in order to highlight the influence of the turbulence grid. As expected, the spectra drops in absence of the turbulence grid and a set of low frequency peak is visible. The aforementioned peaks were also reported by Biondi [23] who related them to the large-eddies structures coming from the compressor and the components in facility's central region. It can be also noticed the persistence of the 5.5 kHz, 7 kHz, 8 kHz, 10 kHz, 20 kHz and 30 kHz peaks even without the TG. Moreover, studies at downstream of the cascade demonstrate that the 10 kHz peak and its harmonics are also present, bringing to the conclusion that they might be related to the rig.

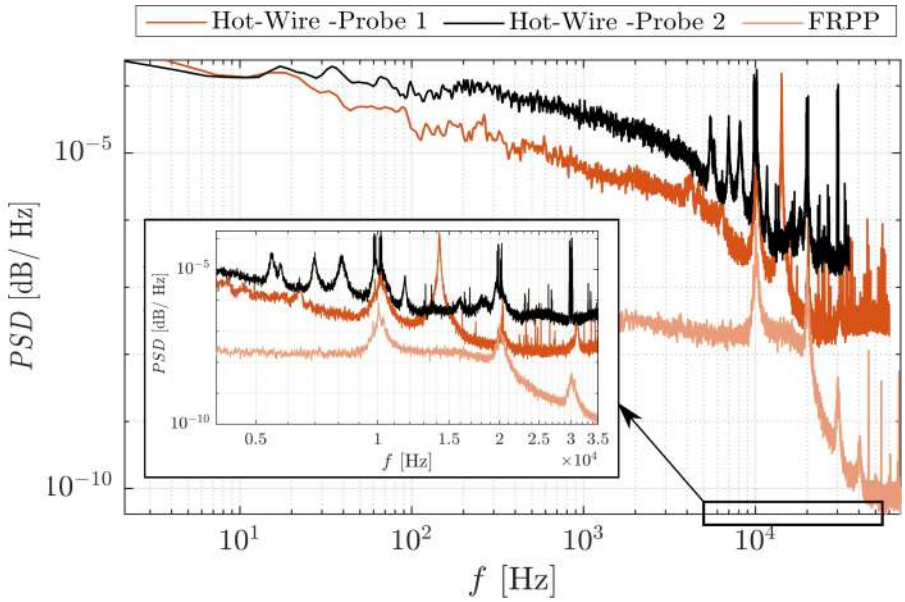

Figure 5.27: Power Spectral Density obtained from different instrumentation.

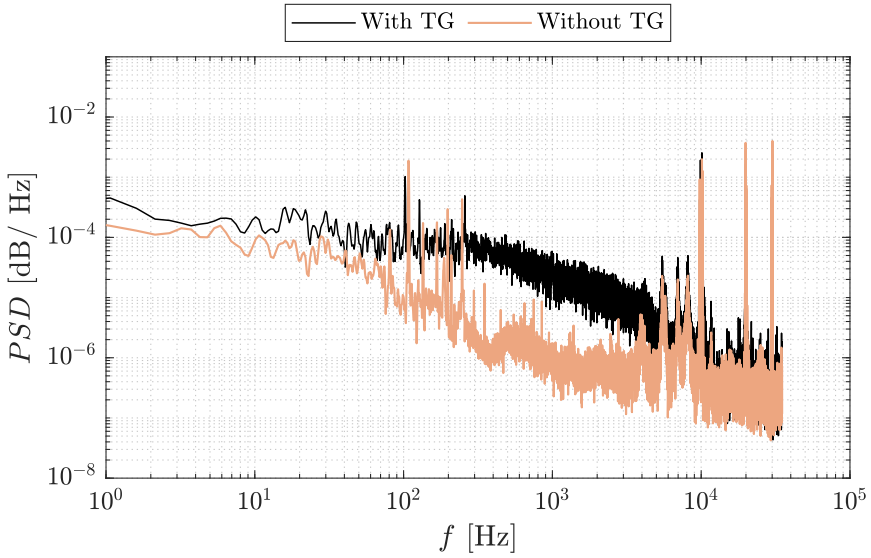

Figure 5.26: Comparison of Power Spectral Density between with and without turbulence generator

Figure 5.27 shows a comparison of PSD at midspan performed with a Fast Response Pressure Probe (FRPP) and the Hot-Wire probe used in the previous campaign (HW1) by Biondi [23] and the one used in the present campaign (HW2). None of the other probes exhibit the presence of the 5.5 kHz, 7 kHz, 8 kHz peaks, therefore it may be related to the probe itself, probably due to either the vibration of the wire or the natural frequency of the prongs.

As already mentioned the wire of the probe was replaced between the two phases of the campaign, what can explain the absence of the 5.5 kHz, 7 kHz, 8 kHz peaks in figure 5.28. In this phase the sampling frequency was increased to 1.2 MHz and the Low-Pass Filter of the CTA system may be observed where beyond the cut-off frequency set as 30 kHz only noise is distinguishable. A new peak at 5.28 kHz appears and it can be related to the bar tip harmonic of the wake generator.

Figure 5.29 depicts a comparison of the PSD for both cases with and without the wake generator. As can be notice the peaks at 10 kHz and 20 kHz still remain although much more lower. Moreover, the three slopes relative to the turbulence cascade processes are clearly visible.

- f^{-1} slope: represents the energy containing the exponential decay of the vortices, where the energy content start to decrease [62].

- $f^{-5/3}$ slope: is the turbulent kinetic energy transport rate in the inertial subrange, where an universal equilibrium between the production and dissipation rates exists.

- f^{-3} slope. This region characteristic of two-dimensional turbulence and it is relative to the enstrophy cascade [63].

Figure 5.30 shows the closest and furthest points at measured at midspan. Since the wake

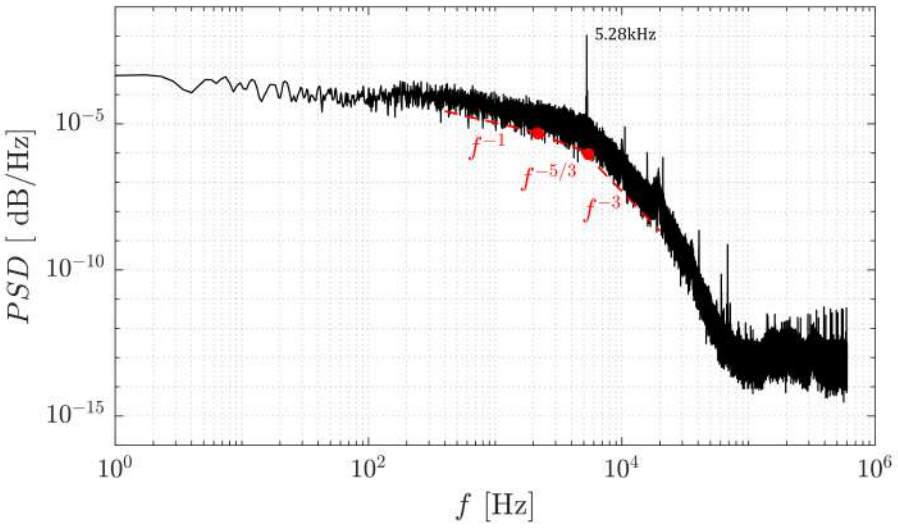

Figure 5.28: Power Spectral Density of the velocity signal at midspan under nominal flow conditions for the second phase of the campaign

generator was placed in a parallel plane to the measurement plane where the hot-wire was placed, no big differences can be seen between the two points. The PSD of the velocity in the boundary layer is presented in figure 5.31. The values are approximately constant until it arrives very close to the wall when achieves a maximum. Therefore, the results are in good agreement with the ones depicted on figure 5.15b.

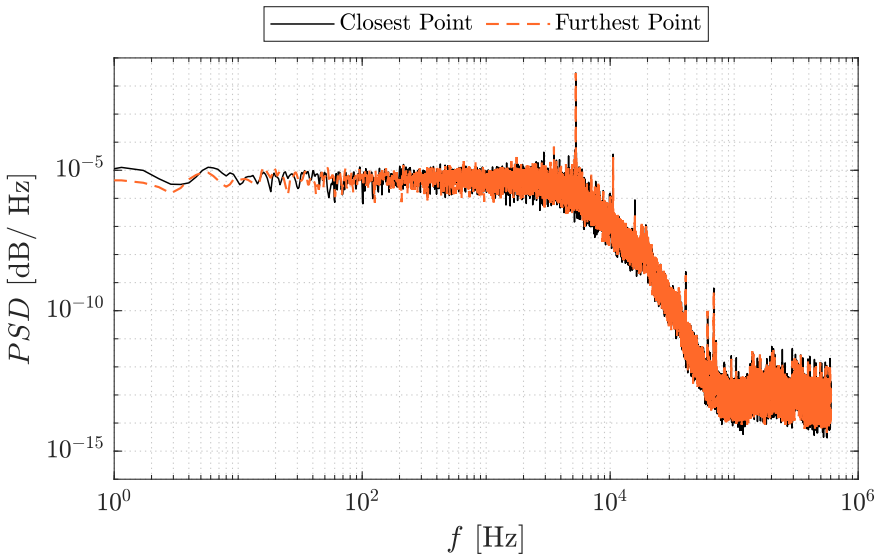

Figure 5.30: Power Spectral Density relative to closest and furthest points to the turbulence generator for the second phase of the campaign

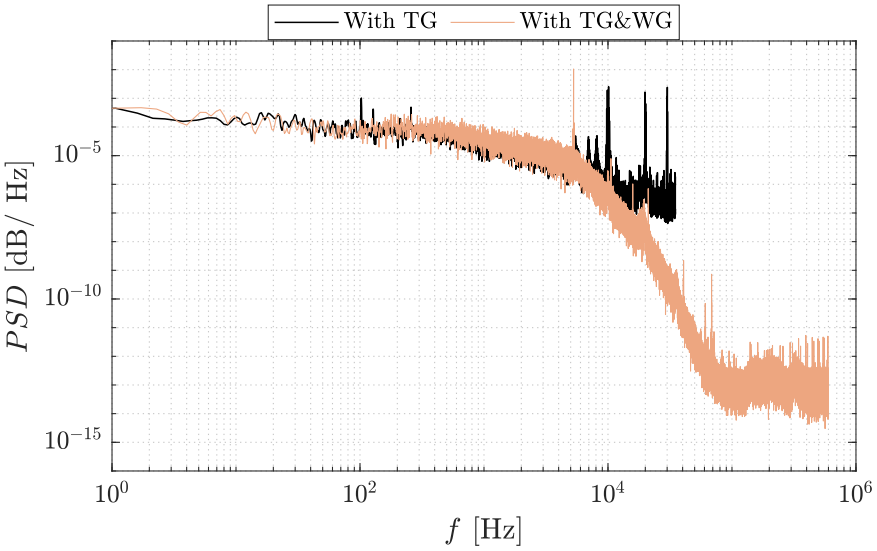

Figure 5.29: Comparison of Power Spectral Density between first and second phase of the campaign

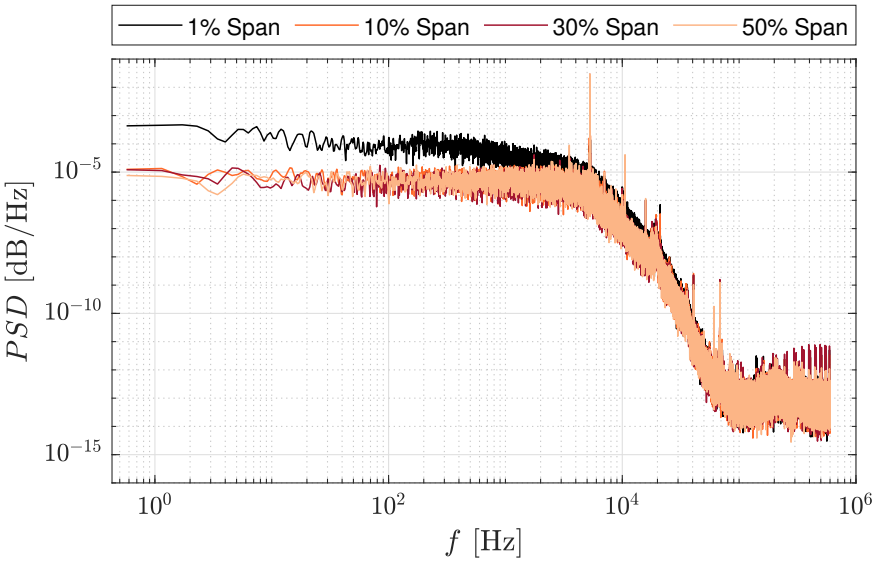

Figure 5.31: Power Spectral Density of the Velocity in the Boundary Layer for the Second phase of the campaign

Chapter 6

Conclusions

The project deals with the application of Constant Temperature Hot-Wire Anemometry operated in low Reynolds and high Mach number conditions in a linear cascade, representative of a low pressure turbine operation. The investigations were conducted in S-1/C high-speed, low-density test rig, located at the von Karman Institute for Fluid Dynamics. The ultimate goal of the project is to provide solid engine representative boundary conditions, such as turbulence intensity and integral length scales, for the development and validation of high-fidelity numerical models.

Hot-Wire Anemometry is is the most frequent technique in experimental fluid dynamics for measuring velocity fluctuations (i.e. turbulence), thanks to the small dimensions of the sensing wire that guarantee high frequency response and high spatial resolution. However, critical aspects need to be taken into account when HWA is applied to high-speed transonic flows. As the operating principle is based on the heat transfer from the heated wire to the flow, the hot-wire is sensitive to velocity, but also to temperature and density , adding an increased degree of complexity to the measurements. Simple voltage-velocity calibration laws can be obtained in isothermal and incompressible flows, but more elaborate methods are required in all other cases. Several attempts have been made with the goal of developing a methodology for calibration of the instrumentation, but without success unless unrealistic assumptions are made.

A non-dimensional calibration methodology for high-subsonic hot-wire measurements, previously developed in VKI by Cukurel et al. [21] and subsequently employed by Boufidi [46] and Biondi [23], was employed in the present study. Cukurel's approach is based on a dimensionless reformulation of the hot-wire output voltage functional relationship . This method consists in expressing the heat transfer law in dimensionless parameters and using correlations to eliminate the compressibility effect. Using a widely-validated correlation, proposed by Dewey [39], the Mach dependency is eliminated. Since Dewey's correlation is validated only beyond M>0.3, an extension to this methodology has been added, by employing the correlation of Klopfer [44] in order to cover also the low Mach number region. Applying both correlations a single $Nu_{corr} - Re$ curve is obtained, resulting in a $Nu = f(Re)$ relationship .

The non-dimensional calibration was employed in previous investigations conducted at VKI by Boufidi [5], who validate Cukurel's methodology for velocity measurements in slip-flow conditions less severes than the ones in the present study. Biondi[23], who perform previous measurements with the same flow conditions of the present study, validate the data reduc-

tion methodology, for time-average measurements. However, the methodology for time-resolved measurements, initially proposed by Cukurel [21] and subsequently modified by Boufidi [5], failed in the prediction on the turbulence intensity. It appears that an instability on the compressibility correlations occurs throughout the iterative cycle when estimating the Mach number fluctuations. This seems to be triggered by a strong variation of the Knudsen number when the density level is really low ($Kn > 0.09$).

The methodology for time-average measurements proposed by Boufidi [5] was employed in the present case. The inlet endwall boundary layer was characterized in terms of mean velocity, integral parameters and wall units.

For the time-resolved measurements three methodologies were compared in the first case of the campaign:

- **TA reduction**: it is the data reduction procedure for Time-Averaged quantities but taking the time-series of the Nusselt number instead of the mean value.

- **TR reduction**:it is the data reduction procedure for Time-Resolved measurements proposed by Boufidi[5].

- **Sensitivities**: it is the data reduction procedure using the sensitivities equations 4.33 -4.35 .

The TA reduction show a good agreement in predict the mach flow number since its was close to the one measure by the pressure measurements. On the other hand this method underestimate the turbulence intensity predicted by Roach. The opposite seems to happen with the TR reduction. Although the turbulence intensity is close to the one predicted by Roach, the mach number is in fair disagreement whit the 5HPP measurements. Therefore this two methodologies were set aside and a the third method was employed. Using equations 4.33 -4.35 the sensitivities can be calculated and the turbulence can retrieved with good agreement with Roach's prediction, while the mach number was obtain directly from the calibration curve. The third method was chosen to perform the time-series measurements for the first and second phase of the cascade.

In the second phase of the campaign a wake generator was mounted in plane01 parallel to plane02 were the measurements with the hot-wire were preform. In these case the total unsteadiness can be considered as the contribution of both periodic and stochastic fluctuations. Since only the the stochastic fluctuations are related to turbulence, a PLA (Phase Locked Averaging) was applied to the data to remove periodic components. Once the periodic fluctuations are subtract from the raw data the sensitivities method can be used to predict the turbulence intensity in the same way as mentioned above.

The hot-wire sensitivities to density, velocity and total temperature have been studied. For

all the cases tested, it is clear that the sensitivity to density and total temperature is greater than the one to velocity. Therefore, the assumption that these fluctuations are negligible must be treated with caution for each application. Interesting evidences were found on the sensitivities values to velocity, witch in the present case are negative since a increase in the velocity decreases the heat transfer. By varying the temperature of the wire, very different sensitivities can be achieved. This was already studied by Boufidi and can be the cause of the difference between the sensitivities in the first and second phase of the campaign.

The turbulence intensity naturally achieved by the facility was found to be 0.8%, this value is in agreement with previous investigations conducted in S-1/C by Michàlek et al [32]. In the first phase of the campaign a turbulence intensity of 2.4% was found at midspan, which according to Roach [30] should be 2.5%. In the second phase of the campaign the wake generator increased the turbulence to 4%.There are no previous cases of studies that can be used as a direct comparison between the turbulence obtained with the turbulence grid and with the presence of the wake generator. But some authors like Wolff et al [58] and Ladwig et al [59] who used an active turbulence generator, estimate that the increase in turbulence should be in the order of 3 to 4% of the free-stream turbulence, which would be in agreement with the values obtained.

The integral length scales were computed with the autocorrelation function and the spectra method proposed by Roach. Both methods were in disagreement with Roach's predictions and also dissimilar values were found between the two approaches. Although the values computed by the spectra method were in agreement with the values computed by Michàlek et al [32], little confidence is given to this results and more studies should be performed.

Finally, the Power Spectra Density of the velocity fluctuations are evaluated in order to provide information about how the energy of the signal is distributed with respect to the frequency.

6.1 Recommendations for future work

Based on the conclusions of the current investigation, the following proposals for future work Hot-Wire Anemometry in high-speed and low-density can be made:

- More specific investigations should be conducted with the goal of testing the stability of the data reduction technique for Time-Resolved measurements by improving the non-dimensional approach proposed by Cukurel [21]. A single hot-wire does not allow the decoupling of the velocity and the density fluctuations from the resultant mass-flux. This, in a low-density flow, due to the high sensitivity of the wire to the density, can lead to strong errors. Therefore, the use of at least a double hot-wire should be considered.

- In order to solve completely the sensitivities equations a triple hot-wire should be implemented. This way the fluctuations to density and total temperature can be consid-

ered and the flow can be thoroughly analyzed. Only this way we can assure the turbulence levels. By using a triple hot-wire, since different wires need to be use, it may be possible to understand why the sensitivity to velocity is negative and which parameters influence this value.

Bibliography

[1] H. Hodson and R. Howell, "The role of transition in high-lift low-pressure turbines for aeroengines," *Progress in Aerospace Sciences*, vol. 41, no. 6, 2005. 1

[2] R. Mayle, "The role of laminar-turbulent transition in gas turbine engines," *Journal of Turbomachinery*, vol. 113, no. 4, pp. 509–536. 1

[3] R. E. Mayle, K. Dullenkopf, and A. Schultz, "The turbulence that matters," *Journal of Turbomachinery*, vol. 1, p. V001T03A046. 1

[4] J. D. Denton, "Some limitations of turbomachinery cfd," *In ASME Turbo Expo 2010: Power for Land, Sea and Air*, vol. 44021, no. GT2010-22540, p. 735–745, 2010. 1, 50

[5] E. Boufidi, "Development of methods for the characterization and uncertainty assessment of turbulent quantities in high speed compressible flows by hot wires and fast response pressure probes," *von Karman Institute For Fluid Dynamics, PhD Report*, 2021. 2, 3, 4, 38, 39, 49, 72, 79, 80

[6] L. V. King, "On the convection of heat from small cylinders in a stream of fluid: Determination of the convection constants of small platinum wires with applications to hot-wire anemometry," *Philosophical transactions of the royal society of London. series A, containing papers of a mathematical or physical character*, vol. 214, no. 509-522, p. 373–432, 1914. 2

[7] J. Boussinesq, "An equation for the phenomena of heat convection and an estimate of the cooling power of fluids," *Journal de Mathematiques*, vol. 1, p. 285–332, 1905. 2

[8] H. H. Bruun, "Hot-wire anemometry: Principles and signal analysis," *Oxford University Press*, 1995. 2, 31, 32, 33, 34, 36, 38, 57, 59

[9] T. Camp and H.-W. Shin, "Turbulence intensity and length scale measurements in multistage compressors," *in ASME 1994 International Gas Turbine and Aeroengine Congress and Exposition*, vol. 117, pp. 38–46, 1994. 2

[10] J. M. Oro, K. M. Díaz, C. Morros, , and E. Marigorta, "On the structure of turbulence in a low-speed axial fan with inlet guide vanes," *Experimental Thermal and Fluid Science*, vol. 32, no. 1, p. 316–331, 2007. 2

[11] J. Maunus, S. Grace, D. Sondak, , and V. Yakhot, "Characteristics of turbulence in a turbofan stage," *Journal of Turbomachinery*, vol. 135, no. 2, p. 021024, 2013. 2

[12] N. Odier, F. Duchaine, L. Gicquel, G. Staffelbach, A. Thacker, N. Rosa, G. Dufour, and J. D. Muller, "Evaluation of integral turbulence scale through the fan stage of a turbofan using hot wire anemometry and large eddy simulation," *American Society of Mechanical Engineers*, vol. 2C, p. V02CT42A021. 2

[13] L. Porreca, M. Hollenstein, A. I. Kalfas, and R. S. Abhari, "Turbulence measurements and analysis in a multistage axial turbine," *Journal of Propulsion and Power*, vol. 23, no. 1, pp. 227–234, 2007. 3

[14] A. C. Chasoglou, M. Mansour, A. I. Kalfas, and R. S. Abhari, "A novel 4-sensor fast-response aerodynamic probe for non-isotropic turbulence measurement in turbomachinery flows," *Journal of the Global Power and Propulsion Society*, vol. 2, pp. 362–375, 2018. 3

[15] D. Lengani, B. Paradiso, and A. Marn, "A method for the determination of turbulence intensity by means of a fast response pressure probe and its application in a lp turbine," *Journal of Thermal Science*, vol. 21, no. 1, p. 21–31, 2012. 3

[16] S. Bauinger, S. Behre, D. Lengani, Y. Guendogdu, F. Heitmeir, and E. Goettlich, "On turbulence measurements and analyses in a two-stage two-spool turbine rig," *Journal of Turbomachinery*, vol. 139, no. 7, p. 071008, 2017. 3

[17] C. B. F. Schwarzbach, C. Muller-Schindewolffs and F. Herbst, "The effect of turbulent scales on low-pressure turbine aerodynamics: Part b—scale resolving simulations," *In ASME Turbo Expo 2018: Turbomachinery Technical Conference and Exposition, American Society of Mechanical Engineers Digital Collection*, vol. 51005, p. V02BT41A004, 2018. 3

[18] S. Chemnitz and R. Niehuis, "A comparison of turbulence levels from piv and cta downstream of a low-pressure turbine cascade at high-speed flow conditions," *In ASME Turbo Expo 2019: Turbomachinery Technical Conference and Exposition, American Society of Mechanical Engineers Digital Collection*, vol. 58561, p. V02BT40A010, 2019. 3

[19] L. Axelsson and W. K. George, "Spectral analysis of the flow in an intermediate turbine duct," *Turbomachinery, Parts A, B, and C. ASMEDC*, vol. 43161, pp. 1419–1426, 2008. 3

[20] L. Axelsson, W. K. George, and T. Johansson, "Fourier decomposed turbulence measurements downstream of a high-pressure turbine stage," *ASMEDC*, vol. 48418, pp. 177–182, 2008. 3

[21] B. Cukurel, S. Acarer, and T. Arts, "A novel perspective to high-speed cross-hot-wire

calibration methodology," *Experiments in fluids*, vol. 53, no. 4, p. 1073–1085, 2012. 3, 4, 38, 43, 45, 48, 79, 80, 81

[22] R. Boyle, B. L. Lucci, and R. G. Senyitko, "Aerodynamic performance and turbulence measurements in a turbine vane cascade," *In ASME Turbo Expo 2002: Power for Land, Sea and Air*, vol. 3610, no. GT2002-30434, pp. 705–714, 2002. 3

[23] F. Biondi, "On the application of hot-wire anemometry in a transonic turbine cascade," *von Karman Institute For Fluid Dynamics, Master Report*, 2021. 4, 7, 10, 12, 14, 35, 45, 49, 50, 55, 56, 57, 67, 69, 71, 74, 75, 79

[24] P. Bradshaw, "An introduction to turbulence and its measurement," *Pergamon Press*, 1971. 7

[25] L. F. Richardson, *Weather prediction by numerical process*. Cambridge university press, 1992, vol. 1. 8

[26] S. B. Pope and S. B. Pope, *Turbulent flows*. Cambridge university press, 2000. 8, 16, 17

[27] A. N. Kolmogorov, "The local structure of turbulence in incompressible viscous fluid for very large reynolds numbers," *Cr Acad. Sci. URSS*, vol. 30, pp. 301–305, 1941. 9

[28] G. I. Taylor, "The spectrum of turbulence," *Proceedings of the Royal Society of London. Series A-Mathematical and Physical Sciences*, vol. 164, no. 919, pp. 476–490, 1938. 13

[29] R. Theunissen, A. Di Sante, M. Riethmuller, and R. Van den Braembussche, "Confidence estimation using dependent circular block bootstrapping: application to the statistical analysis of piv measurements," *Experiments in Fluids*, vol. 44, no. 4, pp. 591–596, 2008. 13

[30] P. E. Roach, "The generation of nearly isotropic turbulence by means of grids," *International Journal of Heat and Fluid Flow*, vol. 8, no. 2, pp. 82–92, 1987. 14, 24, 49, 68, 69, 81

[31] K. Gersten and H. Schlichting, "Hermann schlichting and the boundary-layer theory," in *Hermann Schlichting–100 Years*. Springer, 2009, pp. 3–17. 15, 17

[32] J. Michàlek, M. Monaldi, and T. Arts, "Aerodynamic performance of a very high lift low pressure turbine airfoil (t106c) at low reynolds and high mach number with effect of free stream turbulence intensity," *Journal of Turbomachinery*, vol. 134, no. 6, p. 061009, 2012. 23, 65, 69, 71, 81

[33] G. Batchelor, "Pressure fluctuations in isotropic turbulence," in *Mathematical Proceedings of the Cambridge Philosophical Society*, vol. 47, no. 2. Cambridge University Press, 1951, pp. 359–374. 24

[34] F. Frenkiel, "The decay of isotropic turbulence," pp. 311–321, 1948. 24

[35] M. Monaldi, "Aerodynamics of low pressure turbine blades." von Karman Institute for Fluid Dynamics, 2008. 24, 49, 50

[36] D. Paolucci, "Experimental study of separation and transition on very-high lift low pressure turbine blades at low re and high subsonic conditions." von Karman Institute for Fluid Dynamics, 2007. 24, 49, 50

[37] G. Pastorino, "Calibration and data reduction methods of multi-hole pressure probes for surveys of turbine unsteady flows," *von Karman Institute For Fluid Dynamics, Master Report*, 2021. 28

[38] P. Stainback and K. Nagabushana, "Review of hot-wire anemometry techniques and the range of their applicability for various flows," *a a*, vol. 1, p. 4, 1993. 31, 32, 47

[39] C. F. Dewey Jr, "A correlation of convective heat transfer and recovery temperature data for cylinders in compressible flow," *International Journal of Heat and Mass Transfer*, vol. 8, no. 2, pp. 245–252, 1965. 32, 39, 43, 44, 79

[40] D. Olivari and M. Carbonaro, "Hot wire measurements," *Lecture series-von Karman Institute for fluid dynamics*, vol. 1, pp. 183–218, 1994. 33

[41] G. R. Sarma, "Analysis of a constant voltage anemometer circuit," in *1993 IEEE Instrumentation and Measurement Technology Conference*. IEEE, 1993, pp. 731–736. 34

[42] M. Kegerise and E. Spina, "A comparative study of constant-voltage and constant-temperature hot-wire anemometers part i: The static response," *Experiments in fluids*, vol. 29, no. 2, pp. 154–164, 2000. 34

[43] P. Freymuth, "Frequency response and electronic testing for constant-temperature hot-wire anemometers," *Journal of Physics E: Scientific Instruments*, vol. 10, no. 7, p. 705, 1977. 37

[44] G. Klopfer, "Constant temperature hot wire anemometry data reduction procedure," Tech. Rep., 1974. 44, 79

[45] J. Cole, *Heat transfer from wires at Reynolds numbers in the Oseen range*. Heat Transfer & Fluid Mechanics Inst, University of California, 1954. 44

[46] E. Boufidi and F. Fontaneto, "Towards a more reliable application of hot-wire anemometry in complex compressible flows," 2016. 45, 48, 63, 65, 79

[47] L. S. Kovasznay, "Turbulence in supersonic flow," *Journal of the Aeronautical Sciences*, vol. 20, no. 10, pp. 657–674, 1953. 45, 46

[48] M. V. Morkovin, *Fluctuations and hot-wire anemometry in compressible flows*. North Atlantic Treaty Organization advisory Group for aeronautical research, 1956. 45

[49] W. C. Rose and E. P. McDaid, "Turbulence measurement in transonic flow," *AIAA Journal*, vol. 15, no. 9, pp. 1368–1370, 1977. 47

[50] H. Ikawa, "Turbulent mixing layer experiment in supersonic flow," Ph.D. dissertation, California Institute of Technology, 1973. 47

[51] C. Horstman and W. Rose, "Hot-wire anemometry in transonic flow," *AIAA Journal*, vol. 15, pp. 395–401, 1977. 47

[52] P. Stainback, C. Johnson, and C. Basnett, "Preliminary measurements of velocity, density and total temperature fluctuations in compressible subsonic flow," in *21st Aerospace Sciences Meeting*, 1983, p. 384. 47

[53] K. Nagabushana and P. C. Stainback, "Heat transfer from cylinders in subsonic slip flows," NASA, Tech. Rep., 1992. 47

[54] F. Motallebi, "A review of the hot-wire technique in 2-d compressible flows," *Progress in aerospace sciences*, vol. 30, no. 3, pp. 267–294, 1994. 47

[55] S. Acarer, T. Arts, and B. Cukurel, "Two-dimentional hot-wire anemometry in high-speed flow," *von Karman Institute For Fluid Dynamics, Research Master Report*, 2011. 48

[56] E. Boufidi, T. Arts, J. Clinckemaillie, and F. Fontaneto, "Time-resolved velocity measurements in the wake of a low-pressure turbine blade, at low reynolds and high mach number," *von Karman Institute For Fluid Dynamics, Research Master Report*, 2015. 49, 50, 61, 62

[57] X. Ottavy, S. Vilmin, H. Hodson, and S. Gallimore, "The effects of wake-passing unsteadiness over a highly loaded compressor-like flat plate," *J. Turbomach.*, vol. 126, no. 1, pp. 13–23, 2004. 55

[58] S. Wolff, S. Brunner, and L. Fottner, "The use of hot-wire anemometry to investigate unsteady wake-induced boundary-layer development on a high-lift lp turbine cascade,"

J. Turbomach., vol. 122, no. 4, pp. 644–650, 2000. 65, 81

[59] M. Ladwig and L. Fottner, "Experimental investigations of the influence of incoming wakes on the losses of a linear turbine cascade," in *Turbo Expo: Power for Land, Sea, and Air*, vol. 78927. American Society of Mechanical Engineers, 1993, p. V03CT17A055. 65, 81

[60] L. A. El-Gabry, D. R. Thurman, and P. E. Poinsatte, *Procedure for determining turbulence length scales using hotwire anemometry*. National Aeronautics and Space Administration, Glenn Research Center, 2014. 67

[61] J. C. Lindon, G. E. Tranter, and D. Koppenaal, *Encyclopedia of spectroscopy and spectrometry*, 2016. 72

[62] V. Nikora, "Origin of the "- 1" spectral law in wall-bounded turbulence," *Physical Review Letters*, vol. 83, no. 4, p. 734, 1999. 75

[63] R. H. Kraichnan, "Inertial ranges in two-dimensional turbulence," *The Physics of Fluids*, vol. 10, no. 7, pp. 1417–1423, 1967. 75

Appendix A

Comparison between the PLA at the rotor disk frequency (RDF) and the PLA at the bar passing frequency (BPF)

For the phase locked averaging the raw signal can be divided into a full revolution of the disk considering all 96 bars (RDF) or in a revolution of one of the bars of the disk (BPF).

Figure A.1 shows the PLA for the bar passing frequency where only one bar is observed and figure A.2 shows the PLA for the rotor disk frequency where 96 peaks are visible corresponding to each one of the bars.

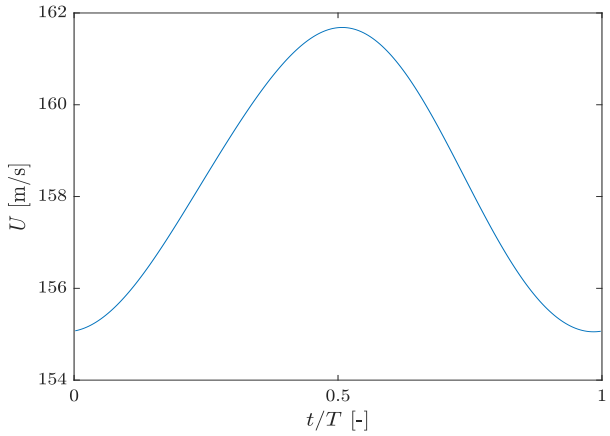

Figure A.1: PLA at the bar passing frequency

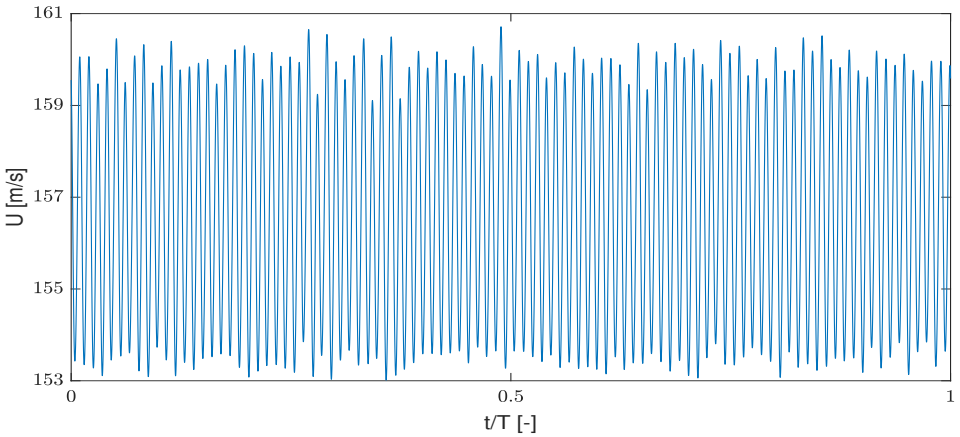

Figure A.2: PLA at the rotor disk frequency

Before subtracting the PLA from the raw signal, the PLA based on the BPF needs to be multiplied by the number of bars (96). Figure A.3 shows a comparison between both PLAs with a maximum deviation of 1.51 m/s.

In figure A.4 and A.5 is possible to see the raw signal and the computed PLA for the BPF and RDF respectively. By subtracting the PLA from the raw signal it is possible to obtain the random fluctuations. The results of the random fluctuations are show in figure A.6. The difference between the two methods results in a error of $\sim 1\%$.

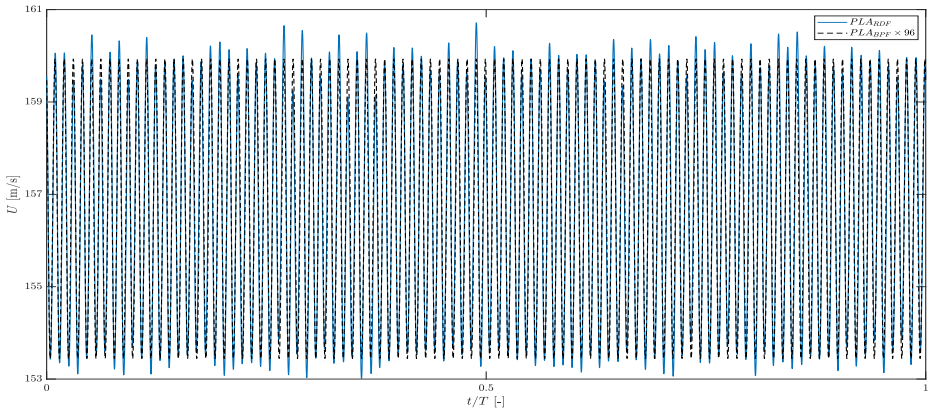

Figure A.3: Comparison between the PLA on the RDF and the PLA on the bar BPF

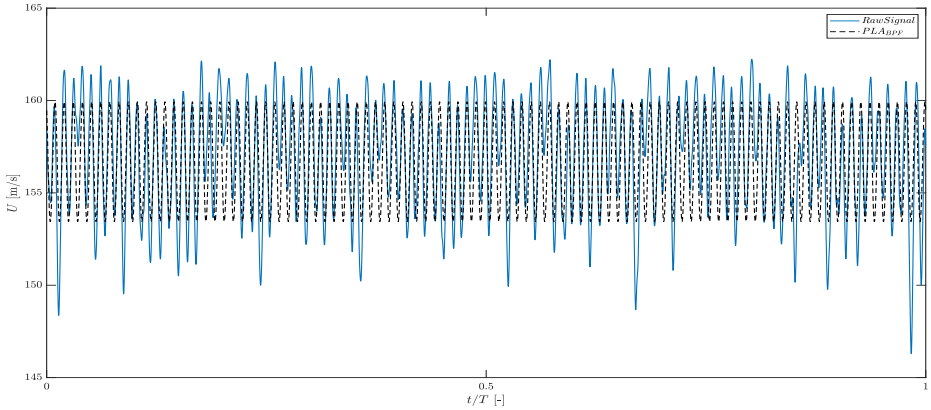

Figure A.4: Raw signal and PLA based on the BPF

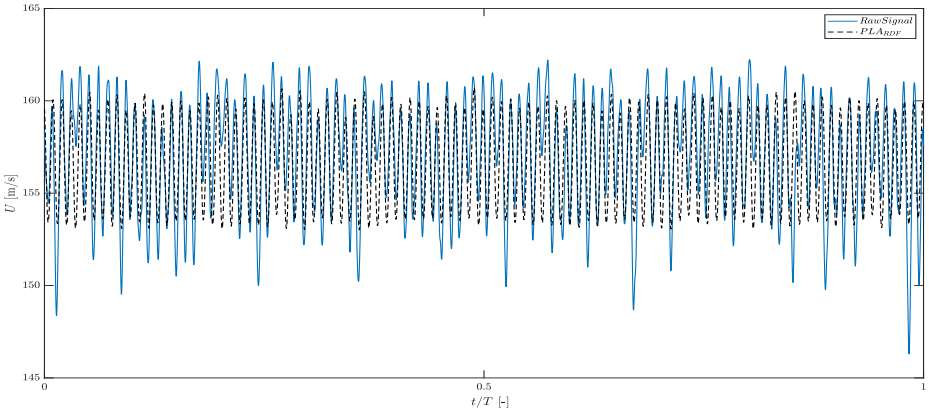

Figure A.5: Raw signal and PLA based on the RDF

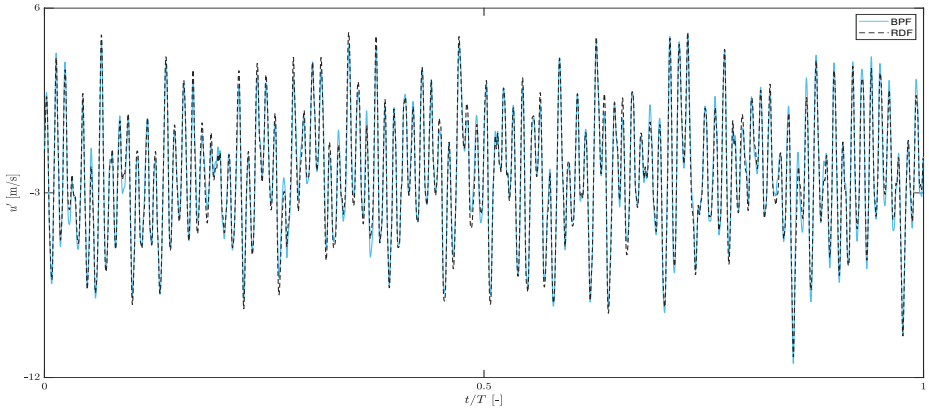

Figure A.6: Comparison between the velocity fluctuations based on the BPF and RDF

Appendix B

Analytical study of the sensitivities

Taking into account the hot-wire characteristics in the first phase of the campaign and the non-dimensional calibration implemented it was possible to make a study of the hot-wire sensitivities for other Mach and Reynolds numbers. Therefore, it is possible to have an idea of the sensitivities for other flow conditions. Figures B.1, B.2 and B.3 show the hot-wire sensitivities to velocity, density and total temperature respectively.

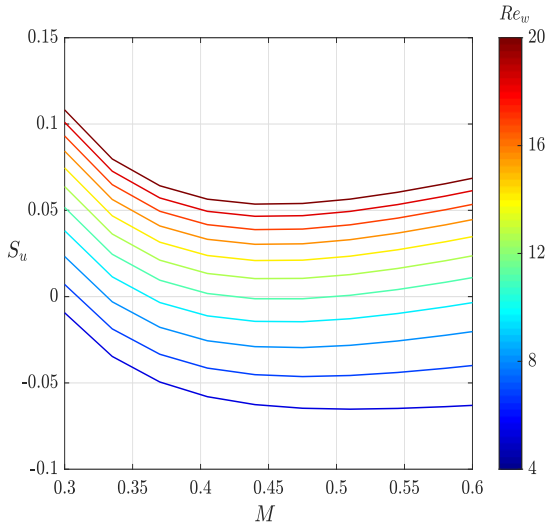

Figure B.1: Sensitivity to velocity for different Mach and Reynolds numbers

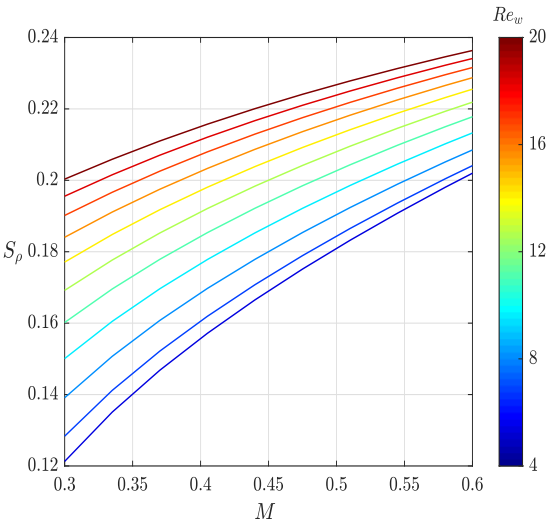

Figure B.2: Sensitivity to density for different Mach and Reynolds numbers

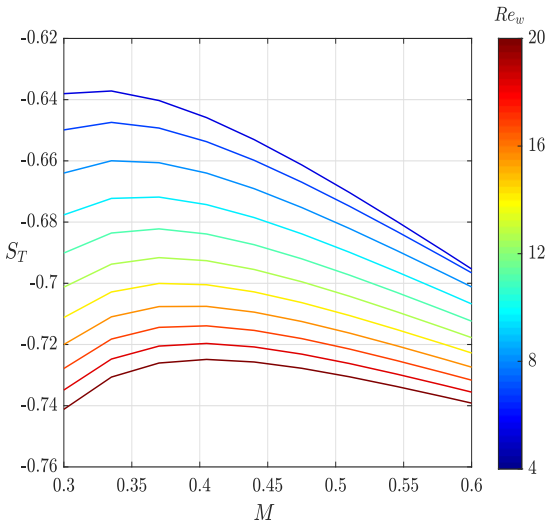

Figure B.3: Sensitivity to total temperature for different Mach and Reynolds numbers